

RESTRICTED

Copy  
RM L9J07



3 1176 00082 0051

CLASSIFIED

NACA

# RESEARCH MEMORANDUM

LOW-SPEED PRESSURE-DISTRIBUTION AND FLOW INVESTIGATION FOR A  
LARGE PITCH AND YAW RANGE OF THREE LOW-ASPECT-RATIO  
POINTED WINGS HAVING LEADING EDGE SWEPT BACK  $60^{\circ}$   
AND BICONVEX SECTIONS

By Ralph W. May, Jr., and John G. Hawes

Langley Aeronautical Laboratory  
Langley Air Force Base, Va.

CLASSIFICATION CANCELLED

J. W. Crawley: Date 12/14/53

CLASSIFIED DOCUMENT

EO 1.0801

Q # 1/1154

RF 1928

This document contains classified information  
relating to the National Defense of the United  
States within the meaning of the Espionage Act,  
50C USC 1 and 2. Its transmission or the  
revelation of its contents in any manner to an  
unauthorized person is prohibited by law.  
Information so classified may be imparted  
only to persons in the military and naval  
services of the United States, appropriate  
civilian officers and employees of the Federal  
Government who have a legitimate interest  
therein, and to United States citizens of known  
loyalty and discretion who of necessity must be  
informed thereof.

NATIONAL ADVISORY COMMITTEE  
FOR AERONAUTICS

WASHINGTON

November 18, 1949

RESTRICTED

UNCLASSIFIED

ERRATA NO. 1

NACA RM L9J07

LOW-SPEED PRESSURE-DISTRIBUTION AND FLOW INVESTIGATION FOR A  
LARGE PITCH AND YAW RANGE OF THREE LOW-ASPECT-RATIO  
POINTED WINGS HAVING LEADING EDGE SWEPT BACK  $60^\circ$   
AND BICONVEX SECTIONS

By Ralph W. May, Jr., and John G. Hawes

November 18, 1949

Page 18, lines 6 and 8 below table: Reference 3 should be reference 2.

Page 19, line 10: Reference 3 should be reference 2.

Page 105: Reference 1 (both in key and legend below figure 54) should be reference 2.

Page 106: In key, reference 3 should be reference 2 and in legend below figure, reference 1 should be reference 2.

NATIONAL ADVISORY COMMITTEE FOR AERONAUTICS

RESEARCH MEMORANDUM

LOW-SPEED PRESSURE-DISTRIBUTION AND FLOW INVESTIGATION FOR A  
LARGE PITCH AND YAW RANGE OF THREE LOW-ASPECT-RATIO  
POINTED WINGS HAVING LEADING EDGE SWEPT BACK  $60^\circ$   
AND BICONVEX SECTIONS

By Ralph W. May, Jr., and John G. Hawes

S U M M A R Y

Pressure distributions and flow characteristics were investigated at low speed through a yaw range from  $0^\circ$  to  $35^\circ$  and an angle-of-attack range through the stall for three small-scale low-aspect-ratio pointed wings having 10-percent-thick biconvex sections,  $60^\circ$  sweptback leading edge, and  $0^\circ$ ,  $30^\circ$ , and  $-30^\circ$  trailing-edge sweep.

An effort was made to correlate the pressure distributions with the strong conical vortex flow observed. At zero yaw, separation vortices, emanating in the region of the wing apexes, increased in size and were swept back farther from the leading edge along the span as the angle of attack was increased. Flow observations showed that the center of vortex rotation coincided with the maximum depth of a region of turbulent separated flow and with a negative pressure peak. Behind the center of vortex rotation a negative-pressure dip occurred as the depth of the turbulent region diminished rather rapidly. With increasing angle of yaw the separation vortices along the leading and trailing semispans became more clearly defined as bound and trailing vortices, respectively.

Section lift coefficients and local centers of pressure at zero yaw and spanwise load distributions throughout the yaw range are presented and discussed with reference to the flow analysis. Force and moment characteristics of the three wings are compared throughout the large yaw range.

I N T R O D U C T I O N

In the Langley full-scale-tunnel investigations of the German delta-wing DM-1 glider (reference 1), a remarkable effect of a sharp

leading edge was observed. Whereas the flow over the original glider with a round leading edge was essentially as expected (characterized by turbulent separation from the trailing edge with the separated region increasing with angle of attack), the flow over the modified glider with a sharp leading edge was characterized by a large vortex on the upper surface just behind the leading edge. The vortex remained attached up to high angles of attack and provided a considerably higher maximum lift coefficient than that of the original configuration. Although such upper-surface attached vortices had been reported previously for low-aspect-ratio airfoils, only relatively meager information was available as to their causes and effects. In view of the likelihood that such flows would be encountered frequently on highly swept wings with sharp or small-radius leading edges, further efforts to define the flow and its effects on the wing characteristics were considered desirable.

The project herein reported represents one of the first steps in this direction. Three related small-scale low-aspect-ratio pointed wings, liberally equipped with pressure orifices, were constructed and studied at low speeds in the entrance cone of the Langley full-scale tunnel. The wings had 10-percent-thick biconvex sections parallel to the air stream,  $60^\circ$  sweptback leading edge, and  $0^\circ$ ,  $30^\circ$ , and  $-30^\circ$  sweep of the trailing edge. Pressure distributions were obtained for a range of angles of attack through the stall and for yaw angles up to  $35^\circ$ . Extensive tuft and smoke studies were made to help clarify the flow and to correlate its characteristics with the measured pressure distributions.

A number of independent but related studies, all for unyawed wings, exist: References 2 and 3 describe force and limited flow studies of delta wings with sharp leading edges; and references 4 to 6 give pressure-distribution and flow studies of delta wings with sharp and round leading edges of different relative radii of curvature. Reference 7 describes a pressure-distribution and flow study through a yaw range of a wing with  $47.5^\circ$  of leading-edge sweep and with a sharp leading edge. Pressure distributions on a two-dimensional 6-percent-thick biconvex airfoil are given in reference 8.

#### S Y M B O L S

Conventional NACA coefficients, reduced from pressure-distribution data neglecting chord force, are referred to the standard stability axes. The Z-axis is in the plane of symmetry and perpendicular to the relative wind, the X-axis is in the plane of symmetry and perpendicular to the Z-axis, and the Y-axis is perpendicular to the plane of symmetry at the quarter chord of the mean aerodynamic chord.

$c_n$	section normal-force coefficient $\left( \int_0^{1.0} p \, d\left(\frac{x}{c}\right) \right)$
$c_l$	section lift coefficient $(c_n \cos \alpha)$
$c_m$	section pitching-moment coefficient about Y-axis $(c_n \bar{x}_c/4)$
$c_{l_\alpha}$	section lift-curve slope at $c_l = 0$ , per degree
$p$	pressure coefficient $\left( \frac{p - p_0}{q} \right)$
$C_N$	wing normal-force coefficient $\left( \frac{1}{2} \int_{-1.0}^{1.0} \frac{c_n c}{c_{av}} \, d\left(\frac{y}{b/2}\right) \right)$
$C_L$	wing lift coefficient $(C_N \cos \alpha)$
$C_{L_{max}}$	maximum wing lift coefficient
$C_{L_\alpha}$	wing lift-curve slope, per degree
$\alpha_{C_{L_{max}}}$	angle of attack for $C_{L_{max}}$ , degrees
$C_m$	wing pitching-moment coefficient $\left( \frac{c_{av}}{2c} \int_{-1.0}^{1.0} c_m \left(\frac{c}{c_{av}}\right)^2 \, d\left(\frac{y}{b/2}\right) \right)$
$C_l$	wing rolling-moment coefficient $\left( \frac{1}{4} \int_{-1.0}^{1.0} \frac{c_n c}{c_{av}} \frac{y}{b/2} \, d\left(\frac{y}{b/2}\right) \right)$
$p$	local static pressure, pounds per square foot
$p_0$	free-stream static pressure, pounds per square foot

$q$  reference dynamic pressure at pitot-tube location (fig. 1.),

pounds per square foot  $\left(\frac{\rho V^2}{2}\right)$

$q_l$  local dynamic pressure, pounds per square foot  $\left(\frac{\rho V_l^2}{2}\right)$

$V$  velocity at pitot-tube location (fig. 1), feet per second

$V_l$  local velocity, feet per second

$\rho$  mass density of air, slugs per cubic foot

$\nu$  kinematic viscosity, square feet per second

$S$  wing area, square feet

$b$  wing span, feet

$c$  local wing chord, feet

$c_{av}$  average wing chord, feet  $(S/b)$

$\bar{c}$  mean aerodynamic chord, M.A.C., feet  $\left(\frac{2}{S} \int_0^{b/2} c^2 dy\right)$

$A$  aspect ratio,  $\left(b^2/S\right)$

$\alpha$  angle of attack, degrees

$\psi$  angle of yaw, degrees

$R$  Reynolds number  $\left(\frac{V_l \bar{c}}{\nu}\right)$

$x$  distance along chord from leading edge, feet

$\bar{x}_{c/4}$ 

distance from local center of pressure to  $\bar{c}/4$  in percent of local chord, positive when  $\bar{c}/4$  is behind

$$\left( \frac{\int_0^{1.0} P \left( 0.25 - \frac{x}{c} \right) d \left( \frac{x}{c} \right)}{c_n} + \frac{\bar{x}_{c/4}}{c} \right)$$

 $x_{c/4}$ 

distance along chord from  $c/4$  to  $\bar{c}/4$ , feet

 $y$ 

distance along span from root chord, positive direction to the right, feet

### M O D E L S

The geometric characteristics and principal dimensions of the three low-aspect-ratio pointed wings with  $60^\circ$  sweptback leading edge and varying trailing-edge sweep are given in figure 2. The wings, designated hereinafter respectively as wings 1, 2, and 3, had  $30^\circ$ ,  $0^\circ$ , and  $-30^\circ$  trailing-edge sweep. All of the wings had 10-percent-thick biconvex sections parallel to the plane of symmetry. The aspect ratios were 3.46, 2.31, and 1.73, and the angles of sweep of the quarter-chord line were  $55.2^\circ$ ,  $52.4^\circ$ , and  $49.1^\circ$  for wings 1, 2, and 3, respectively. A close-up photograph of wing 1 is shown as figure 3(a) and a photograph showing wing 3 mounted in the entrance cone is given as figure 3(b).

Wings 2 and 3 were made of  $\frac{3}{32}$ -inch sheet brass attached with flush

rivets to a rigid steel inner structure. Wing 1 was cast of a tin-bismuth alloy with a steel insert for added strength. Approximately 200 orifices were located on the left semispan of each wing at 7 stations, hereinafter designated as stations 1, 2, 3, 4, 5, 6, and 7, which were located at 0, 16.7, 33.3, 50.0, 66.7, 83.3, and 91.6 percent of the semispan from the plane of symmetry, respectively. The chordwise location of the orifices on each wing is given in table I. The wing support sting, which served as a conduit for the pressure tubes, was set off center on the right semispan and was faired smoothly into the bottom surface near the trailing edge, leaving the upper surface clear of any protuberance.

## T E S T S

The over-all arrangement of the testing apparatus as located just inside the entrance cone of the Langley full-scale tunnel is sketched in figure 1 and is shown in part by the photograph of figure 3(b). The wings assumed a wide range of positions in the air stream with varying pitch and yaw because the pitch and yaw axes were located 5.3 feet behind the wing apexes at  $\psi = 0^\circ$  and  $\alpha = 0^\circ$ .

The air-stream angularity and the distribution of  $q$  in the entrance cone were surveyed with a six-prong yaw-pitch head in a vertical plane located 7 inches behind the apexes of the wings at  $\alpha = 0^\circ$  and  $\psi = 0^\circ$ . The survey was made in 1-foot vertical increments from 5 feet to 10 feet above the tunnel floor, and in  $\frac{1}{2}$ -foot horizontal increments through a distance of 4 feet on each side of the wing center lines.

Orifice pressures over the left semispan were recorded through an extensive angle-of-attack range from  $-10^\circ$  to well through the stall angle for yaw angles of  $0^\circ$ ,  $\pm 2^\circ$ ,  $\pm 4^\circ$ ,  $\pm 6^\circ$ ,  $\pm 8^\circ$ ,  $\pm 10^\circ$ ,  $\pm 15^\circ$ ,  $\pm 20^\circ$ ,  $\pm 25^\circ$ ,  $\pm 30^\circ$ , and  $\pm 35^\circ$ . All wings were tested at an approximate airspeed of 55 miles per hour or a Mach number of 0.07 and a Reynolds number of  $0.57 \times 10^6$  for wing 1,  $0.85 \times 10^6$  for wing 2, and  $1.14 \times 10^6$  for wing 3. Wing 2 was also tested for the zero-yaw condition at an airspeed of approximately 95 miles per hour corresponding to a Reynolds number of  $1.42 \times 10^6$  in order to obtain an indication of the scale effect. Surface-tuft studies were made on the three wings at several angles of attack for yaw angles of  $0^\circ$ ,  $10^\circ$ ,  $20^\circ$ , and  $35^\circ$  and tuft-probing studies were made on wing 2 at zero yaw. Extensive smoke studies were made on each wing at yaw angles of  $0^\circ$  and  $20^\circ$  to observe the vortex flow.

## R E D U C T I O N O F D A T A

## AIR-STREAM FLOW ANALYSIS

Results of the entrance-cone survey show that the  $q_z/q$  ratio (ratio of dynamic pressure in the surveyed plane to the reference dynamic pressure at the pitot tube used throughout the tests (fig. 1)) over the region occupied by the left semispan of the wings varied throughout the yaw and angle-of-attack range from about 0.87 to 0.90 (fig. 4). These ratios were low primarily because the reference pitot tube was in a relatively high velocity field; however, the over-all variation in dynamic pressure was of about the same magnitude as reported in reference 9 for



the test section of the Langley full-scale tunnel. The pitch angularity of the air stream in the region of the left semispan did not vary materially throughout the angle-of-attack range (fig. 5(a)) although it did vary from about  $1^\circ$  at  $\psi = 35^\circ$  to  $3^\circ$  at  $\psi = -35^\circ$ . The air-stream yaw angularity varied about  $1.5^\circ$  in the area occupied by the left semispan (fig. 5(b)). The air-stream pitch angle and the local dynamic pressure fluctuated noticeably in the lower region of the survey plane.

The extent to which the indicated asymmetric air flow influenced the wing-pressure data cannot be ascertained reliably. The survey must be considered only as an indication of general effect for the survey was taken in just one plane located 7 inches behind the apexes of the wings when  $\psi = 0^\circ$  and  $\alpha = 0^\circ$ , or approximately  $0.2\bar{c}$  ahead of the mean aerodynamic chord of wing 2. A comparison of the pressure distributions along the centrally located station 1 at equal positive and negative yaw angles might be expected to give an indication of the magnitude of the flow irregularity, especially since station 1 was located on a ridge (section A-A of fig. 2(b)) where the local pressures were sensitive to cross-flow velocity components. Because, however, these pressures also were very sensitive to minor construction irregularities along the ridge, especially to slight asymmetries in the location of the orifices along the ridge, such a procedure was not considered trustworthy.

#### CORRECTIONS TO DATA

A constant stream-angle correction, determined by the zero-lift condition at zero yaw, was used throughout the yaw range. Corrections for support-sting interference and for tunnel-boundary effects were assumed to be negligible for the tests. At  $\pm 20^\circ$  and  $\pm 35^\circ$  yaw, however, the pressure data of the 80-percent and 90-percent chord orifices of station 1 on the bottom surface were not used because of noticeable support-sting interference.

The contribution of chord force to the lift and pitching-moment coefficients was considered to be small enough to neglect. A representative calculation made for wing 2 at zero yaw and at  $24.1^\circ$  angle of attack showed that the greatest increment in the section lift coefficient due to chord force was 2.4 percent at station 2, while the over-all wing-lift-coefficient increment was only 1.1 percent.

The pressure data for all yaw angles were plotted and analyzed, but only the results of representative yaw angles are presented in this paper.

## RESULTS AND DISCUSSION

## CHORDWISE PRESSURE DISTRIBUTIONS AND FLOW CHARACTERISTICS

## Pressure Distributions and Flow Characteristics at Zero Yaw

Presentation of data.- The zero-yaw chordwise pressure distributions of the three wings investigated are plotted in rectangular Cartesian coordinates in figures 6 to 11 and in oblique Cartesian coordinates on isometric views of the wing plan forms in part (a) of figures 12 to 26. The zero-yaw flow characteristics as observed by surface tufts are shown in part (a) of figures 27 to 29.

Concept of correlation between pressure distributions and flow.- Each wing semispan displayed a region of relatively high negative pressure over the upper surface that was confined to a narrow strip at the leading edge for the lowest angles of attack. With increasing angles of attack the region outboard along the semispan progressively swept back from the leading edge and inward toward the plane of symmetry; that is, the region progressively fanned out over a greater chordwise length. Immediately downstream from the high negative pressures was a lower negative-pressure region, which was well defined over the inboard stations but which spread increasingly over the outboard sections. As substantiated by smoke-flow and tuft-probing studies, these high and low negative-pressure regions were associated with conical separation vortices. The three-dimensional vortices, rotating with the bottom tangential component of velocity toward the leading edge, are illustrated schematically in figures 30(a) and 30(b) as observed over wing 2. The sections outboard along the semispan effectively operated at progressively higher resultant angles of attack and the resulting higher leading-edge negative pressures at the wing tips caused a strong spanwise flow of the low-energy boundary-layer air. Observations from a direction parallel to the wing leading edge of a narrow jet of smoke issued close to the leading edge gave a representative visual interpretation of the chordwise flow such as is sketched in figure 30(c) for wing 2 at  $\alpha = 24.1^\circ$ . The short-dash line represents a stream line at the boundary of the region of rotating turbulent flow. The boundary was distinct over the forward part of the turbulent region but became less defined farther back. The tuft probing and smoke studies indicated that the center of vortex rotation and the maximum depth of the turbulent region occurred at the chordwise position corresponding to the negative-pressure peak. Behind the point of maximum thickness, the depth of the turbulent flow diminished rather rapidly; and, as the boundary of the turbulent region bent toward the wing surface, the value of the negative pressure coefficient decreased sharply and approached more nearly the free-stream static pressure at the approximate chordwise point of contact of the boundary with the wing surface. The position of the pressure dip could be defined reliably by tufts when the vortex was strong

by establishing a narrow chordwise band where tufts at the wing surface were in a state of transition between the undisturbed rearward flow and the strong spanwise flow in the separated region of lower pressure.

Generally the same type of pressure distributions were reported in reference 8 for a two-dimensional investigation of a 6-percent-thick biconvex section; however, the pressure change following the peak negative pressure was not as great as observed in the present three-dimensional investigation. Unpublished data for the two-dimensional airfoil (investigated in reference 8) indicate a standing region of turbulent separated flow having its greatest depth at approximately the position of maximum negative pressure and decreasing in depth farther back chordwise where the reduction in negative pressure occurred. Measured velocity profiles indicated that the boundary of the separated region had the same general contour as the boundary streamline sketched in figure 30(c) for wing 2 of the present investigation. For the two-dimensional airfoil the pressure dip seemed to be just behind the chordwise location where surface tufts indicated intermittent forward and rearward flow.

Pressure distributions and flow characteristics of wing 2 at zero yaw. - In light of the general concepts given in the foregoing remarks, the pressure distributions and flow characteristics of wing 2, which are typical for all three wings, are discussed in detail. At an angle of attack of  $4.1^\circ$  a region of relatively high negative pressure close to the leading edge was followed by a region of lower pressure, which indicated the presence of a separation vortex along most of the semispan. The tip sections at this low angle of attack were more highly loaded than the inboard stations. One apparent reason for the higher outboard loading was the increasing induced angle of attack along the semispan such as would be expected from considerations of potential flow over a triangular wing. The areas of relatively high and low negative pressures at the short outboard chords were poorly defined (fig. 8). Two possible explanations for the characteristic decreasing chordwise pressure change outboard from station 4, caused primarily by the weakening of the negative-pressure dip behind the vortex, could be (a) an equalization of pressure throughout the thickened tip boundary layer and (b) a more gradual return of the flow above the turbulent vortex region to the wing surface. This gradual return could be caused by the vortex trying to sweep back from the leading edge as it does for higher angles of attack.

With the angle of attack increased to  $8.1^\circ$ , the vortex swept back on the wing and became stronger and thus gave sharper distinction between the negative-pressure peaks and dips on the wing. The pressure distributions of figure 8 indicate that the vortex was approximately at 4, 10, 15, 30, and 65 percent of the chord of stations 2, 3, 4, 5, and 6, respectively. The vortex was increasingly hard to locate by the pressure distributions outboard from station 4 because as the vortex grew larger

and as the boundary layer thickened, a less defined peak-negative-pressure region resulted. The pressure distributions indicate station 7 to be stalled, apparently from leading-edge separation since the vortex was behind station 7 at  $\alpha = 8.1^\circ$ . Surface tufts, however, showed only the usual strong spanwise flow with no visible indication of stall (fig. 28(a)). This same characteristic tuft behavior was noted at all angles of attack for the wing area ahead of the vortex.

Increasing the angle of attack to  $14.1^\circ$  and to  $24.1^\circ$  continued the trends of increasing the vortex size and strength and of sweeping it back farther from the wing leading edge and inward toward the plane of symmetry. The separation vortex at  $\alpha = 24.1^\circ$  caused a negative-pressure peak at the center station 1. The difference in the pressure coefficient from -3.0 to -0.4 between the 10-percent and 30-percent chordwise orifices of station 2 ( $0.167\ b/2$ ) indicates that the vortex was very strong. A pressure coefficient of -2.1 was measured at the 20-percent chord of station 3 in the peak-negative-pressure region, but at station 4 the vortex was relatively parallel to the air stream and too large to influence the attainment of an outstanding peak-negative-pressure coefficient. At  $\alpha = 24.1^\circ$  the vortex at the tip swept inward enough toward the plane of symmetry so as not to be behind stations 6 and 7. As expected, figure 8(b) shows that these two stations remained stalled; however, the negative pressures on the upper surface were considerably increased over those at  $\alpha = 14.1^\circ$ ; with the net result that the stations developed more lift at  $\alpha = 24.1^\circ$ . At  $\alpha = 24.1^\circ$ , but not at  $14.1^\circ$ , surface tufts at stations 6 and 7 indicated decisive stall (fig. 28(a)) such as noted for the wing tips of the original DM-1 glider configuration with rounded nose in reference 1 and the round-nose delta wings of reference 7, all of which had trailing-edge separation.

The pressure distributions, smoke-flow observations, and tuft studies showed that further increases in the angle of attack merely continued the trends of increasing the size and sweepback of the vortex and of increasing the area of outboard stall until at  $\alpha = 44.1^\circ$  practically the complete wing was stalled. The progression of the regions of relatively high and low negative pressure over wing 2 is shown very effectively by the pressure distributions plotted over an isometric view of the wing in part (a) of figures 17 to 21.

The pressure distributions, as previously described for a Reynolds number of about  $0.85 \times 10^6$ , were essentially unaffected by increasing the Reynolds number to  $1.42 \times 10^6$ . The change in vortex location was negligible as indicated by the pressures; however, the peak pressure coefficients were generally higher and small changes in the area of the pressure-distribution curves occurred with the increased Reynolds number.

Comparison of pressure distributions and flow characteristics of wings 1, 2, and 3 at zero yaw.- The zero-yaw pressure distributions of wings 1 and 3 were quite similar in nature to those of wing 2, although three primary differences were evident. First, at comparable stations and angles of attack the widths of the negative-pressure peaks and dips, measured in percent of chord, increased with aspect ratio with the greater successive difference being between wings 1 and 2. For example, at  $\alpha = 14.1^\circ$  the peak-negative pressure in the region of the separation vortex was at about 12, 8, and 6 percent of the chord of station 2 for wings 1, 2, and 3, respectively. Thus at equal angles of attack the vortex at any specified station was generally about the same absolute distance from the leading edge of each wing. Second, the maximum negative pressure coefficient increased with decreased wing aspect ratio. As shown in figures 6, 9, and 11, the highest measured pressure coefficient at station 2 ( $0.167 b/2$ ) was  $-2.25$  at  $\alpha = 24.1^\circ$  for wing 1,  $-3.13$  at  $\alpha = 34.1^\circ$  for wing 2, and  $-3.50$  at  $\alpha = 34.1^\circ$  for wing 3. Third, the extent of tip stall was progressively greater for the wings of higher aspect ratio although the boundary-layer-flow tuft diagrams of figures 27(a), 28(a), and 29(a) indicate that the flow direction was similar for each wing. The pressure distributions of figures 6 to 26 show the same trend.

Comparison of theoretical and experimental pressure distributions at zero yaw.- Theoretical two-dimensional pressure distributions (calculated at equal  $c_l$  by use of reference 10) are compared with the measured distributions for each station at  $\alpha = 4.1^\circ$  in figures 6, 8, and 10 for wings 1, 2, and 3, respectively. Station 1 for all wings had a favorable pressure gradient extending well behind midchord, as is predicted by the theory of reference 11. With the exception of the vortex region at the leading edge, station 2 exhibited the same tendency to a lesser degree. Because the leading edge was swept back, the measured stagnation pressures were much less than  $1.0q$ . For an infinitely long  $60^\circ$ -sweptback airfoil, the stagnation pressure corresponding to the velocity normal to the leading edge should be  $0.25q$ , which may be compared with the values of  $0.15q$  to  $0.42q$  measured for the present wings at  $\alpha = 4.1^\circ$ .

#### Pressure Distributions and Flow Characteristics in Yaw

Presentation of data.- The effects of yaw angles of  $10^\circ$ ,  $20^\circ$ , and  $35^\circ$  on the pressure distributions of the three related wings are presented in figures 12 to 26, and the effects on the boundary-layer flow as indicated by surface tufts are shown in figures 27 to 29. The pressure coefficients for positive wing yaw shown over the isometric view of the right semispan in figures 12 to 26 were actually measured over the left semispan with the wings at equal negative yaw angles.

Concept of correlation between pressure distributions and flow.-

As observed by smoke-flow studies, the vortex increased in size on the trailing semispan but became obscure on the leading semispan as the wings were yawed at moderate and high angles of attack. As for zero yaw, the pressure distributions on the trailing semispan had negative-pressure peaks and dips up to yaw angles of about  $20^\circ$ , which indicated that the vortex had the characteristics of the separation vortex as discussed for  $\psi = 0^\circ$ . Nevertheless, increasing the sweep of the leading edge in yaw gradually transformed the trailing semispan vortex into more of a trailing vortex of approximately constant cross-sectional area. Thus at  $\psi = 35^\circ$  there was little evidence of negative-pressure peaks or dips on the upper surface of the trailing semispan, which indicated that the nature of the vortex was different from that at zero yaw.

Apparently as the leading edge of the leading semispan was losing sweep with increased yaw, the vortex became more clearly defined as merely part of the bound (or lifting) vortex system. However, earlier tip stall of the leading semispan also occurred in yaw with the result that visible indications of the vortex, as evidenced by the smoke-flow studies and the pressure distributions, became unnoticeable over the outboard sections.

Pressure distributions and flow characteristics of wing 2 in yaw.-

As evidenced by the negative-pressure peaks and dips, the pressure distributions for the low angle of attack of  $4.1^\circ$  (fig. 17) indicate that the vortex generally moved increasingly forward on the leading semispan and rearward on the trailing semispan as the yaw angle increased. The pressure distributions over the leading semispan at the highest yaw angles approached those indicated by two-dimensional theory for low angles of attack. (See fig. 8 for  $\alpha = 4.1^\circ$  at  $\psi = 0^\circ$ .) The extreme outboard stations of the left semispan were even more highly loaded than at zero yaw. The loading on the leading semispan increased and that on the trailing semispan decreased in yaw. The airfoil sections parallel to the air stream changed with increasing yaw so that at  $35^\circ$  of yaw the left semispan leading edge with only  $25^\circ$  of sweep was the leading edge of the entire wing, and the region of greatest lift over the forward part of these altered airfoil sections was mostly on the leading semispan. With increasing sweep of the right semispan in yaw, the peak-negative-pressure region at the leading edge became smaller and did not exist in the extreme case of  $\psi = 35^\circ$  when the leading edge had  $95^\circ$  of sweep.

In a reverse manner than that at  $\alpha = 4.1^\circ$ , the vortex moved rearward on the leading semispan and slightly forward on the trailing semispan as the angle of attack was increased to  $14.1^\circ$  (fig. 18). (Data not presented indicated that at  $\alpha = 8.1^\circ$  the yaw range investigated had practically no effect on the vortex location.) An increase in the angle of yaw to  $10^\circ$  or more caused tip stall of the leading semispan as shown by the boundary-layer-flow diagrams of figure 28.

The same trends in vortex flow shown for  $\alpha = 14.1^\circ$  were prevalent at  $\alpha = 24.1^\circ$ . The negative-pressure peaks and dips over the leading semispan became less pronounced in yaw so that at  $\psi = 20^\circ$  they were not evident. As discussed in the previous section, two apparent reasons are the transformation of the separation vortex to a bound vortex and the large extent of outboard stall. A schematic sketch of the vortex flow as observed by smoke studies at  $\psi = 20^\circ$  and  $\alpha = 20^\circ$  is given as figures 30(d) and 30(e). The smoke studies revealed considerable flow of air around the leading edge from the under surface of the trailing semispan into the top of the large vortex and, therefore, indicated that the trailing semispan vortex was transforming into a trailing vortex. This leading-edge flow apparently accounts for the negative values of  $P$  on the lower surface of the trailing semispan in the leading-edge region (fig. 19). When the angle of attack was increased to  $34.1^\circ$  for yaw angles of  $10^\circ$  or greater, there was no indication of a vortex on the stalled leading semispan as evidenced by the pressure distributions and the smoke-flow studies. The large trailing-semispan vortex had the characteristics of a trailing vortex with essentially a constant cross-sectional area along the wing leading edge. There was a very strong flow of air around the leading edge into the vortex as mentioned in the previous paragraph for  $\alpha = 24.1^\circ$ . At  $\alpha = 44.1^\circ$ , visible indications of the separation vortex had dissipated and the flow over the wing was completely stalled or unsteady for all yaw angles investigated.

Comparison of pressure distributions and flow characteristics of wings 1, 2, and 3 in yaw.- The effects of yaw on wings 1 and 3 were quite similar to the effects on wing 2. The three principal differences among the pressure distributions and flow characteristics of the related wings noted at zero yaw generally prevailed throughout the yaw range tested. First, for identical stations and equal angles of attack and yaw, the vortex was farther back in percent of the shorter chords of the wings of higher aspect ratio. Second, the highest negative values of the pressure coefficient increased with decreased wing aspect ratio and also were higher at moderate yaw angles than at  $\psi = 0^\circ$ . Thus for station 2 of the trailing semispan at  $\psi = 10^\circ$  and  $\alpha = 34.1^\circ$ , pressure coefficients of -3.45, -4.10, and -4.22 were measured for wings 1, 2, and 3, respectively. Third, the characteristic more pronounced tip stall with increasing wing aspect ratio observed at zero yaw was also evident for the leading-semispan tip in yaw (figs. 27, 28, and 29). Peculiarities were noted at  $\alpha = 14.1^\circ$  where wing 3 had more tip stall than wing 2 for  $\psi = 20^\circ$  and as much or more tip stall than both wings 1 and 2 for  $\psi = 35^\circ$ . Contrary to the usual case, station 6 of the leading semispan of wing 1 actually unstalled in going from  $\psi = 20^\circ$  to  $\psi = 35^\circ$  at  $\alpha = 14.1^\circ$ .

Effects of vortex flow on airplane stability and control.- A thorough understanding of the flow about a highly swept wing has special significance. In particular, if controls were located in the field of

influence of a vortex, the growth and development of the vortex flow, as on the triangular wings reported herein, would be expected to have first-order effects on the stability and control of an airplane and also on the effectiveness of the controls. As found recently in a low-speed investigation of a small-scale wing having NACA 65-006.5 sections (reference 12), serious discontinuities in the lift, pitching-moment, and damping coefficient curves occurred for particular installations of outboard vertical fins. The significance of these particular results as applied to the full-scale wing is not clear at this time due to inadequacy of large-scale information, but evidently the presence of a vortex on a large-scale wing, as has been observed for wings having sharp-edge sections, would be expected to influence largely the low-speed characteristics of wings having outboard fins, nacelles, or other similar protuberances. The

recent investigation of reference 7 for a wing with  $47\frac{1}{2}^\circ$  leading-edge

sweep and with 10-percent-thick biconvex sections has shown the same characteristic pressure distributions as described in this paper. Although the flow was not investigated in detail on the large-scale wing, the presence of a strong vortex was immediately evident in explorations of smaller models of the same plan form.

#### SECTION LIFT CHARACTERISTICS AT ZERO YAW

As the angle of attack was increased, the spanwise position of maximum  $c_l$  and the extent of reduced tip effectiveness moved inboard on each wing at a rate increasing with increased aspect ratio (figs. 31 to 33). The relatively high tip loading is shown for  $\alpha = 4.1^\circ$ , as previously discussed, but at  $\alpha = 8.1^\circ$  the tips of each wing incurred loss of lift, with the loss being much more severe for the high aspect ratio wing 1.

As shown again effectively in the curves of  $c_l$  against  $\alpha$  of figures 34 to 36, this loss of lift accompanying the collapse or movement off the wing of the negative-pressure peak occurred more rapidly with increased distance from the plane of symmetry of each wing and, as already noted, more rapidly for the wings of higher aspect ratio where the vortex swept behind the wing tips sooner. As noted in the section entitled "Pressure Distributions and Flow Characteristics at Zero Yaw," this primary tip stall occurred apparently from leading-edge separation but did not alter the strong spanwise boundary-layer flow as could be determined visibly by surface tufts. However, with increased wing angle of attack the  $c_l$  values for the outboard stations increased again even though the sections became visibly stalled as evidenced by surface tufts.



The effect of the flow on the over-all lift characteristics of the wings is illustrated by the increased section lift-curve slopes and the nonlinearity of the slopes along the span of each wing as given in the following table for  $\alpha = 0^\circ$ :

Station	$\frac{y}{b/2}$ (percent)	Wing 1		Wing 2.		Wing 3	
		$R \times 10^6$	$c_{l\alpha}$	$R \times 10^6$	$c_{l\alpha}$	$R \times 10^6$	$c_{l\alpha}$
1	0	0.86	0.028	1.28	0.023	1.71	0.014
2	16.7	.71	.030	1.06	.026	1.43	.015
3	33.3	.57	.034	.85	.027	1.14	.016
4	50.0	.43	.044	.64	.028	.86	.017
5	66.7	.39	.056	.43	.049	.57	.038
6	83.3	.14	.094	.21	.081	.29	.071
7	91.6	.07	.120	.11	.103	.14	.090

The scatter of the data and the insufficiency of low angle-of-attack data, except for wing 2, make the fairing of the curves of  $c_l$  against  $\alpha$  in figures 34 to 36 and the determination of  $c_{l\alpha}$  values somewhat questionable near zero lift. Nevertheless, the data of the preceding table are sufficiently reliable to show the trends of increased  $c_{l\alpha}$  with increased aspect ratio of the related wings. Nonlinear lift curves would be expected from considerations of the varying three-dimensional vortex and boundary-layer flow.

#### SPANWISE-LOAD DISTRIBUTIONS

At low angles of attack where the separated-flow region near the leading edge was small and sharp along the entire span, the lift over the wings was close to the theoretical lift and the spanwise-load distributions were approximately elliptical for the three wings. However, with increased angle of attack the distributions deviated from elliptical curves as an outboard dip and a hump farther inboard developed. The humps occurred at the spanwise locations where the region of separated flow covered a large extent of the chord and effectively gave the airfoil

larger camber, thereby producing a higher loading. Farther outboard where the separated region covered the entire chord and the boundary layer thickened, the sections effectively became stalled, thereby causing the aforementioned dip in the span-loading curves. Since the humps and dips were a function of the vortex flow, they shifted progressively inboard with increased angle of attack. Yawing the wings moved more of the spanwise loading to the leading semispan, especially at low angles of attack (figs. 37 to 48).

The spanwise-loading humps and dips for wing 2 at  $\psi = 0^\circ$  are shown in figure 41. The spanwise loading at  $\alpha = 4.1^\circ$  agreed fairly well with the Weissinger theoretical loading obtained by use of reference 13, although the experimental curve had a hump above the theoretical curve outboard from station 4. Study of the basic pressure distributions reveals that the hump resulted from the weakening or loss of the negative-chordwise-pressure dip behind the vortex. The humps located at approximately 65, 60, 30, 15, 10, and 0 percent of the semispan as the vortex swept back at angles of attack of  $8.1^\circ$ ,  $14.1^\circ$ ,  $24.1^\circ$ ,  $32.1^\circ$ ,  $36.1^\circ$ , and  $44.1^\circ$  may be attributed mainly to additional camber effects. Yawing wing 2 reduced or removed the humps in the loading curves on the trailing semispan (figs. 42 to 44) and increased the magnitude of the humps on the leading semispan. The loading difference between the two semispans was most pronounced for low angles of attack and decreased as the angle of attack was increased.

The variation of the spanwise loading with angle of attack and yaw followed the same trends for all three wings except that the humps and dips tended to be more pronounced for wing 1 than for the other two wings. The comparison of the experimental and theoretical loadings for  $\alpha = 4.1^\circ$  of wing 3 was much poorer than for the other wings with the experimental loading being considerably higher for the center station 1.

The discrepancy noted between the loading of station 1 in positive and negative yaw generally increased with angle of yaw. The increase in the pitch angularity of the air stream in the negative-yaw direction, as found by the survey, undoubtedly had an appreciable effect in causing the loading of station 1 to be generally higher at negative yaw than at positive yaw. However, the large discrepancy in the variation among wings, especially between wing 3 and the other two wings, seems to indicate that the effect of the orifices of station 1 not being located on the exact center of the rounded ridge had a greater effect in yaw than the flow irregularity as discussed in the section entitled "Air-Stream Flow Analysis."

## CENTERS OF PRESSURE AT ZERO YAW

The local center-of-pressure variation with angle of attack (figs. 49 to 51) depended primarily upon the change in size, strength, and location of the vortex. At  $\alpha = 4.1^\circ$  the center of pressure was generally in the vicinity of the quarter chord from station 3 outboard except for a slight rearward displacement from the quarter-chord line at the outboard spanwise location where the chordwise negative pressure dip behind the vortex weakened. Each center-of-pressure curve for higher angles of attack had a rearward displacement with reference to the quarter-chord line, with the most rearward point generally moving inboard as the angle of attack was increased. This maximum rearward displacement of local center of pressure generally occurred at the spanwise location where the vortex was on the rear of the section chords. Farther inboard for each angle of attack of each wing above  $4.1^\circ$ , the local center of pressure was closer to or even ahead of the quarter-chord line where the negative-chordwise-pressure dips behind the vortex were located on the rear of the section chords and the negative pressure peaks in the vortex region were on the forward part of the chords. The distance from the plane of symmetry of the described regions of rearward and forward center-of-pressure displacement from the quarter-chord line varied approximately inversely with the wing aspect ratio. Although its variation with angle of attack was erratic, the center of pressure at station 1 was always at a greater percent of the local chord behind the leading edge, generally between 0.35c and 0.40c, than the center of pressure of station 2.

At an angle of attack of approximately  $4^\circ$ , as shown in figure 52, the lateral center of pressure of the three wings was about 42 percent of the semispan, which is only about 1 percent higher than that predicted by the Weissinger theory in reference 13. With increased angle of attack there was a gradual inboard movement of the lateral center of pressure for each wing as the outboard sections progressively became less effective. The distance of the spanwise center of pressure from the plane of symmetry varied among the wings basically as an inverse function of aspect ratio, although a greater successive change in position at a given angle of attack was noted between wings 1 and 2 than between wings 2 and 3 because of the more rapid loss of outboard effectiveness for wing 1 as noted in the section entitled "Section Lift Characteristics at Zero Yaw."

## WING FORCE AND MOMENT CHARACTERISTICS

## Lift and Pitching-Moment Characteristics at Zero Yaw

The lift-curve slopes of the three wings were practically linear but increased slightly with aspect ratio below the angle-of-attack range of  $12^\circ$  to  $14^\circ$  (fig. 53). At higher angles of attack, however, the slopes in contrast decreased with aspect ratio. The values of  $C_{L_{max}}$ ,  $\alpha_{C_{L_{max}}}$ , and  $C_{L_\alpha}$  (measured at  $C_L = 0.2$ ) for the three wings and the theoretical values of  $C_{L_\alpha}$  (obtained from reference 13 at  $C_L = 0$  using the Weissinger theory) are presented in the following table:

Wing	A	$C_{L_{max}}$	$\alpha_{C_{L_{max}}}$ (deg)	Measured $C_{L_\alpha}$ at $C_L = 0.2$ (per deg)	Theoretical $C_{L_\alpha}$ at $C_L = 0$ (per deg)
1	3.46	0.98	34.1	0.043	0.046
2	2.31	1.16	36.1	.041	.042
3	1.73	1.17	38.5	.037	.037

The experimental values of  $C_{L_\alpha}$  were measured at  $C_L = 0.2$  due to insufficient data at zero lift for all three wings. The experimental values agree well with the theoretical values and tend to increase with increased wing aspect ratio. A comparison is made in figure 54 of the lift of wing 2 at Reynolds numbers of  $0.85 \times 10^6$  and  $1.42 \times 10^6$  with that of the large-scale wing of reference 3 (identical in plan form and section to wing 2) at a Reynolds number of  $2.91 \times 10^6$ . The wing of reference 3, which had negligible scale effect from Reynolds numbers of  $2.91 \times 10^6$  to  $9.61 \times 10^6$ , generally had a slightly higher lift-curve slope than wing 2 and a more gradual stall at a lower  $C_{L_{max}}$  (1.08) and  $\alpha_{C_{L_{max}}}$  ( $33^\circ$ ). Consistent with these trends, increasing the Reynolds

number of wing 2 increased the lift-curve slope except at low angles of attack and produced a more gradual stall. The inclusion of the 1.1-percent increment in  $C_L$  due to chord force mentioned in the section entitled "Corrections to Data" for wing 2 at  $\alpha = 24.1^\circ$  and  $R = 0.85 \times 10^6$  would give better agreement than noted in figure 54.

The longitudinal stability of the three wings increased slightly with aspect ratio between lift coefficients of about 0.15 and 0.4; however, above that lift coefficient the longitudinal stability decreased with increased wing aspect ratio (fig. 55). Wings 2 and 3 had good stability throughout the  $C_L$  range including a stable break at stall. Although wing 1 had a stable break at the stall, it had a strong destabilizing shift in the pitching-moment curve at about  $C_L = 0.6$ , where the rapid loss of outboard lift was noted. The excellent agreement between the longitudinal stability of wing 2 and that for the comparable large-scale wing of reference 3 again illustrates the validity of the low Reynolds number data for configurations having sharp-edged sections.

Lift and moment characteristics in yaw. - The effect of yaw on  $C_L$ ,  $C_m$ , and  $C_l$  of the three wings is given in figures 56 to 58. As is the case for conventional wings, the decrease in  $C_L$  with yaw was more pronounced as the angle of attack increased. Also the decrease in  $C_L$  with yaw was generally greater for all angles of attack as the wing aspect ratio increased. The general effect of yaw on the curves of  $C_L$  against  $\alpha$  (figs. 27 to 29) was to decrease the lift-curve slope and make it less linear and to broaden and lower the curve in the region of  $C_{L_{max}}$ . The trends of decreasing  $C_{L_{max}}$  and increasing  $C_{L_{\alpha}}$  with increased wing aspect ratio noted at zero yaw also generally prevailed in yaw. The effect of angle of yaw on  $C_m$  was insignificant for all wings. The variation of  $C_l$  with yaw was erratic, but generally at  $\psi = 0^\circ$  it indicated dihedral effect which varied from positive or approximately zero values at low angles of attack to strong negative values as the angle of attack increased to  $\alpha_{C_{L_{max}}}$ . For angles of yaw greater than about  $10^\circ$ , the dihedral effect generally increased negatively with yaw for all wings in the angle-of-attack range investigated below stall.

## SUMMARY OF RESULTS

The significant results of the low-speed pressure-distribution and flow investigation of three small-scale low-aspect-ratio pointed wings having 10-percent-thick biconvex sections,  $60^\circ$  sweptback leading edge, and  $0^\circ$ ,  $30^\circ$ , and  $-30^\circ$  trailing-edge sweep may be summarized as follows:

1. At zero yaw each wing had conical separation vortices that emanated in the region of the apex and increased in size and were swept back farther from the leading edge along the span as the angle of attack was increased. Flow observations showed that the center of vortex rotation coincided with the maximum depth of a region of turbulent

separated flow and with a negative pressure peak. Behind the center of vortex rotation a negative-pressure dip occurred as the depth of the turbulent region diminished rather rapidly.

2. In yaw at moderate and high angles of attack, the vortex increased in size and assumed the characteristics of a trailing vortex on the trailing semispan, but apparently transformed into a bound vortex on the leading semispan.

3. The pressure distributions and flow characteristics of the three wings were similar in nature except that (a) the regions of increased and decreased negative pressure extended farther, in percent of chord, at comparable spanwise stations of the wings with higher aspect ratio because the vortex location was generally about the same absolute distance from the leading edge of each wing at equal angles of attack and yaw, (b) the highest negative pressure coefficient decreased with increasing wing aspect ratio, and (c) the area of decreased tip effectiveness increased with wing aspect ratio.

4. At low angles of attack and zero yaw, the spanwise-load distributions agreed fairly well with those predicted by the Weissinger lifting-line theory. With increasing angle of attack, however, the center of semispan loading shifted inboard because of the increasing extent of the stalled area at the tip and because of the development of a pronounced hump in the spanwise-loading curve just inboard of the stalled area. The inboard movement of the semispan center of pressure was generally greater for the wings of higher aspect ratio.

5. Yawing the wings shifted more of the spanwise loading to the leading semispan, especially at low angles of attack.

6. The local chordwise center of pressure at zero yaw was generally at about 35 to 40 percent of the chord at the plane of symmetry. Outward along the span from the plane of symmetry at each angle of attack the center of pressure was first closer to or even ahead of the quarter-chord line where the vortex was on the forward part of the chord and then finally farther behind the quarter-chord line near the midspan as the vortex moved to the rear of the wing.

7. The wing lift-curve slopes increased and the values of maximum lift coefficient decreased with increased wing aspect ratio.

8. All wings had a stable pitching-moment break at stall, but for lift coefficients above 0.4 the longitudinal stability decreased with aspect ratio, especially for the highest aspect-ratio wing.

9. The lift and pitching moments of the wing with zero-trailing-edge sweep agreed remarkably well with those published in NACA RM L8G05 for a comparable large-scale wing.

Langley Aeronautical Laboratory  
National Advisory Committee for Aeronautics  
Langley Air Force Base, Va.

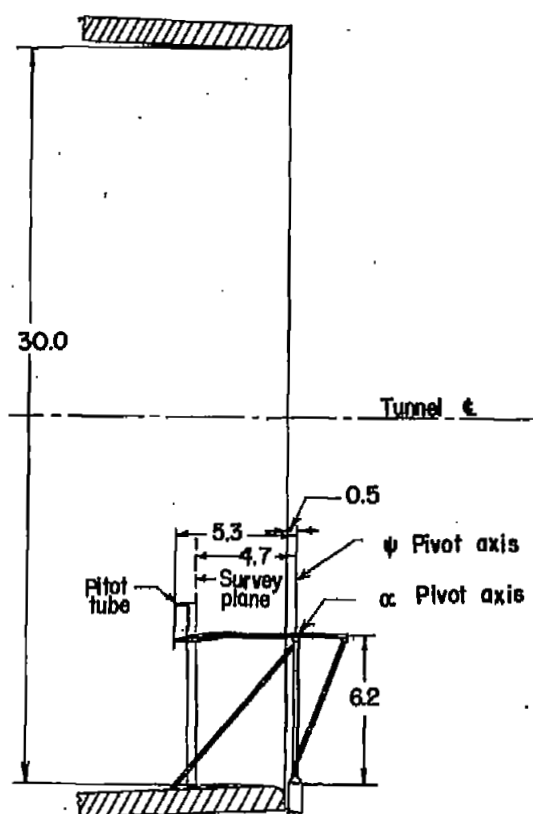
## R E F E R E N C E S

1. Wilson, Herbert A., Jr., and Lovell, J. Calvin: Full-Scale Investigation of the Maximum Lift and Flow Characteristics of an Airplane Having Approximately Triangular Plan Form. NACA RM L6K20, 1947.
2. Whittle, Edward F., Jr., and Lovell, J. Calvin: Full-Scale Investigation of an Equilateral Triangular Wing Having 10-Percent-Thick Biconvex Airfoil Sections. NACA RM L8G05, 1948.
3. Anderson, Adrien E.: An Investigation at Low Speed of a Large-Scale Triangular Wing of Aspect Ratio Two.- I. Characteristics of a Wing Having a Double-Wedge Airfoil Section with Maximum Thickness at 20-Percent Chord. NACA RM A7F06, 1947.
4. Wick, Bradford H.: Chordwise and Spanwise Loadings Measured at Low Speed on a Triangular Wing Having an Aspect Ratio of Two and an NACA 0012 Airfoil Section. NACA TN 1650, 1948.
5. Anderson, Adrien E.: Chordwise and Spanwise Loadings Measured at Low Speed on Large Triangular Wings. NACA RM A9B17, 1949.
6. Orlik-Rückemann, K.: Experimental Determination of Pressure Distributions and Transition Lines of Plane Delta Wings at Low Speeds and Zero Yaw. KTH-Aero TN 3, Roy. Inst. of Technology, Div. of Aero., Stockholm, Sweden, 1948.
7. Lange, Roy H., Whittle, Edward F., Jr., and Fink, Marvin P.: Investigation at Large Scale of the Pressure Distribution and Flow Phenomena over a Wing with the Leading Edge Swept Back  $47.5^\circ$  Having Circular-Arc Airfoil Sections and Equipped with Drooped-Nose and Plain Flaps. NACA RM L9G15, 1949.
8. Underwood, William J., and Nuber, Robert J.: Aerodynamic Load Measurements over Leading-Edge and Trailing-Edge Plain Flaps on a 6-Percent-Thick Symmetrical Circular-Arc Airfoil Section. NACA RM L7H04, 1947.
9. Theodorsen, Theodore, and Silverstein, Abe: Experimental Verification of the Theory of Wind-Tunnel Boundary Interference. NACA Rep. 478, 1934.
10. Theodorsen, T., and Garrick, I. E.: General Potential Theory of Arbitrary Wing Sections. NACA Rep. 452, 1933.

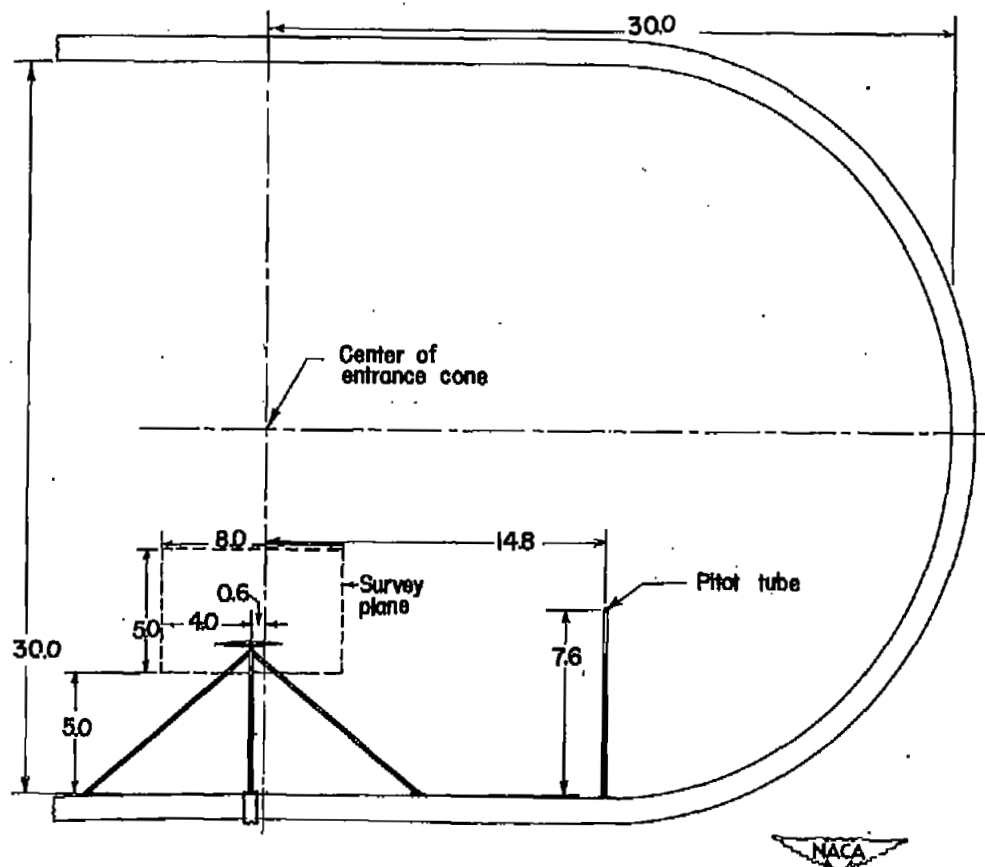


11. Jones, Robert T.: Subsonic Flow over Thin Oblique Airfoils at Zero Lift. NACA Rep. 902, 1948.
12. Jaquet, Byron M., and Brewer, Jack D.: Effects of Various Outboard and Central Fins on Low-Speed Static-Stability and Rolling Characteristics of a Triangular-Wing Model. NACA RM L9E18, 1949.
13. DeYoung, John: Theoretical Additional Span Loading Characteristics of Wings with Arbitrary Sweep, Aspect Ratio, and Taper Ratio. NACA TN 1491, 1947.



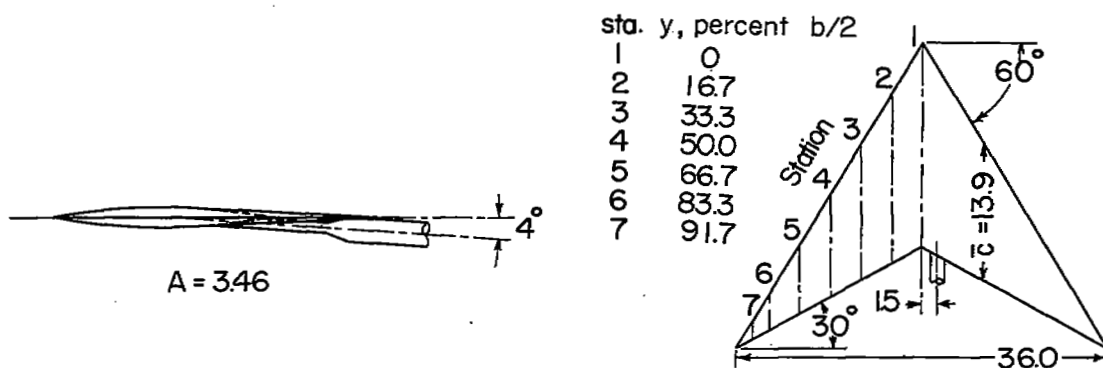


(a) Side view.

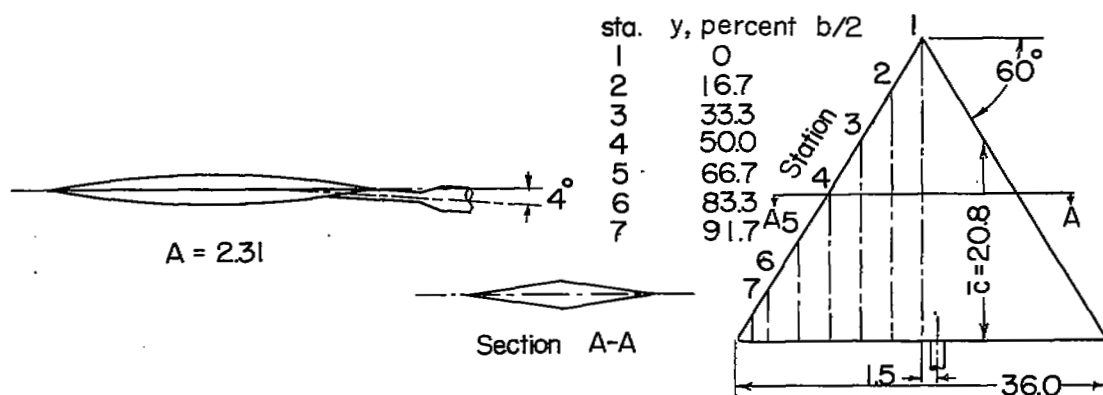


(b) View looking into entrance cone from rear of model.

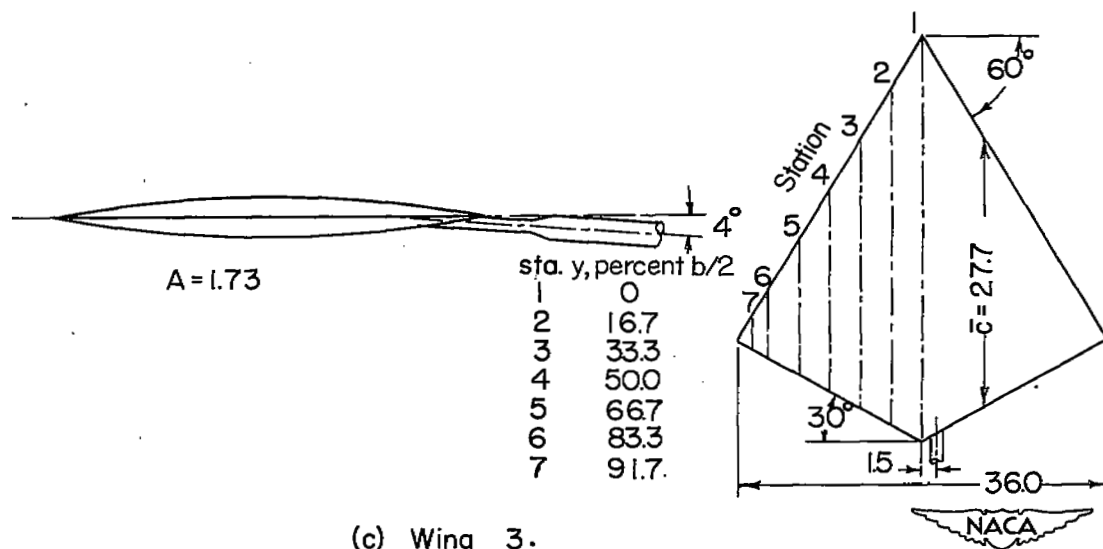
Figure 1.- Sketch of test setup in entrance cone of Langley full-scale tunnel. All dimensions are in feet.



(a) Wing 1.

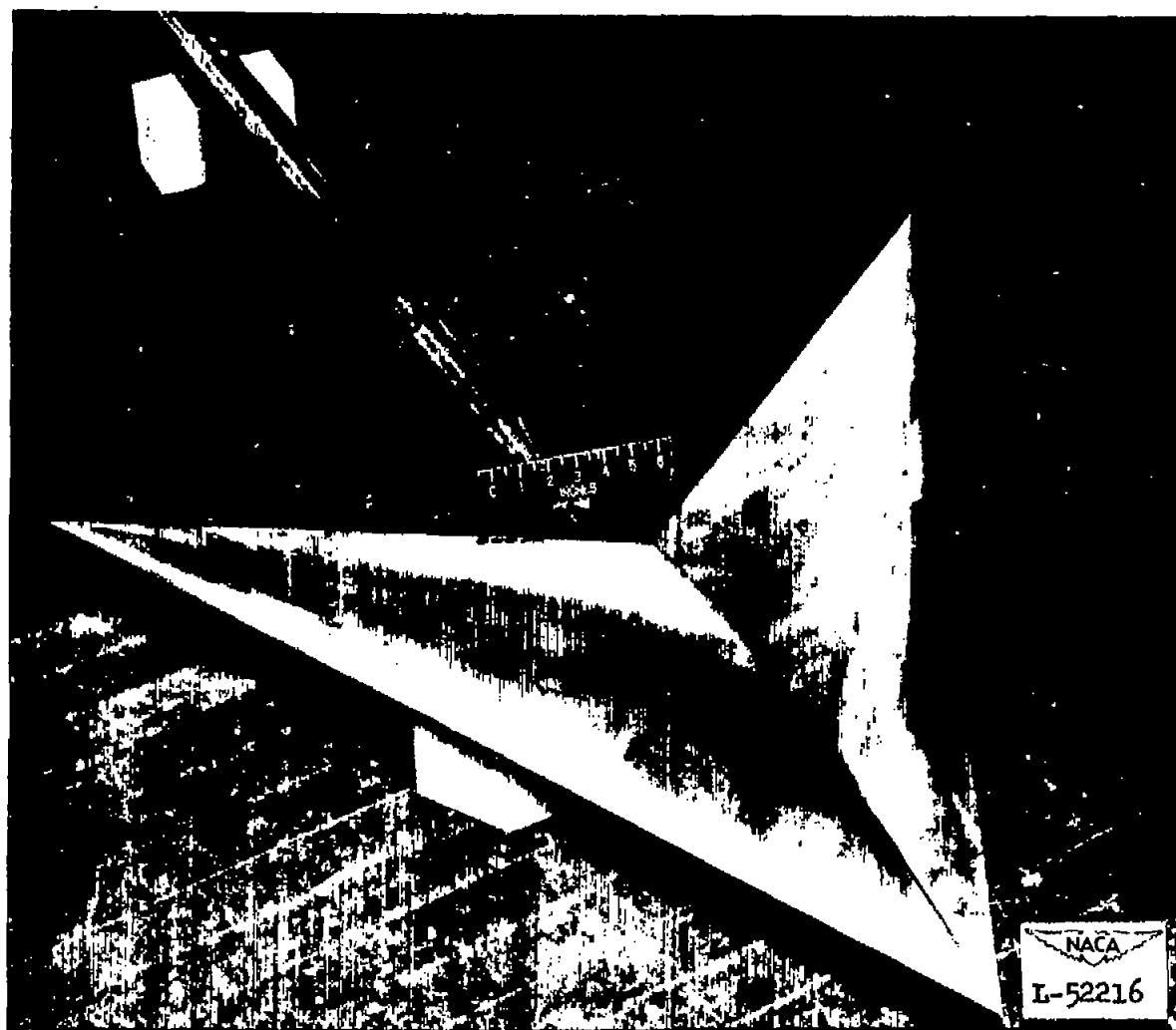


(b) Wing 2.



(c) Wing 3.

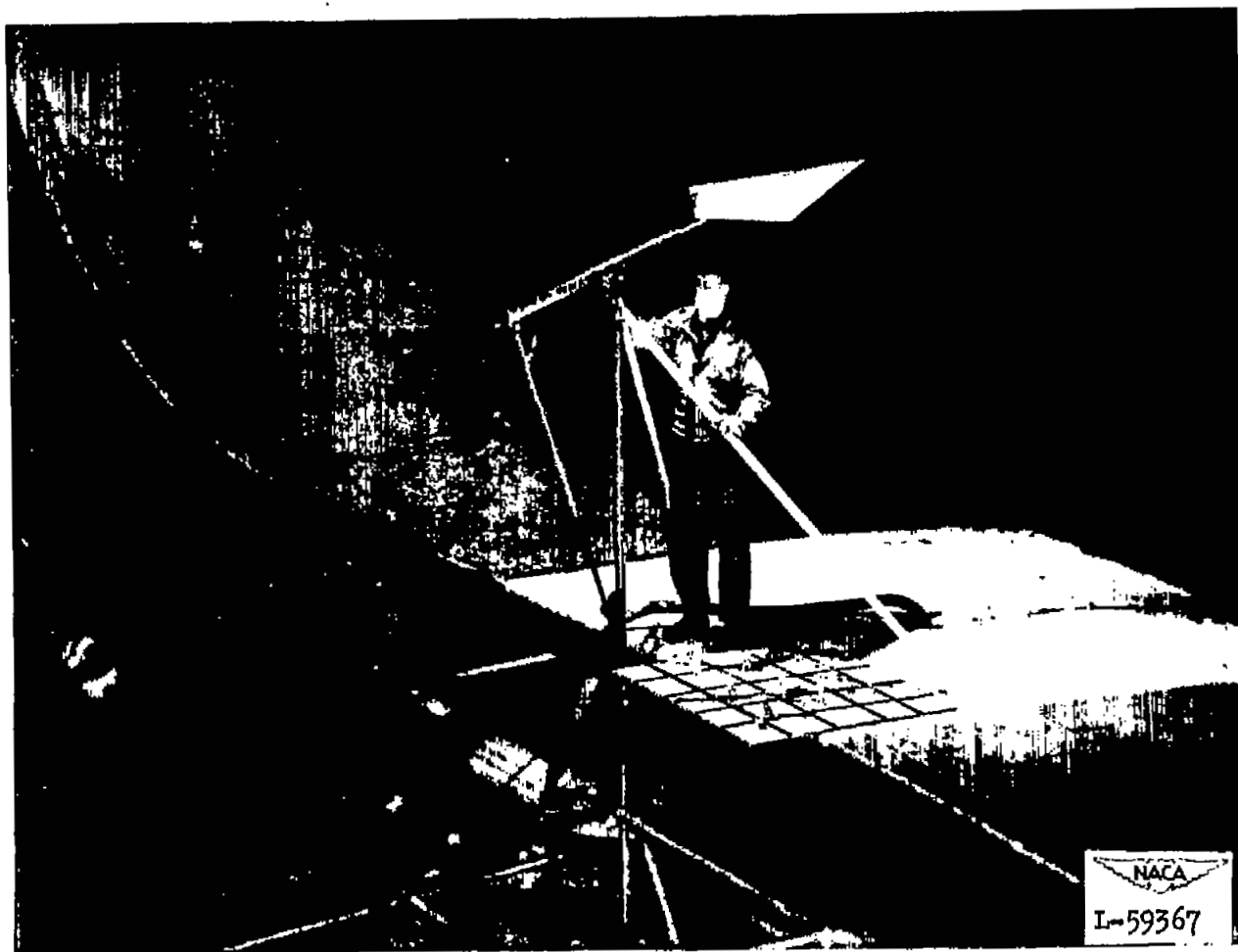
Figure 2.- Geometric characteristics of wings tested. All dimensions are in inches.



(a) Close-up view of wing 1.

Figure 3.- Wings and test apparatus.





(b) Three-quarter rear view of wing 3 mounted in tunnel;  $\psi = 0^\circ$ ,  $\alpha = 10^\circ$ .

Figure 3.- Concluded.





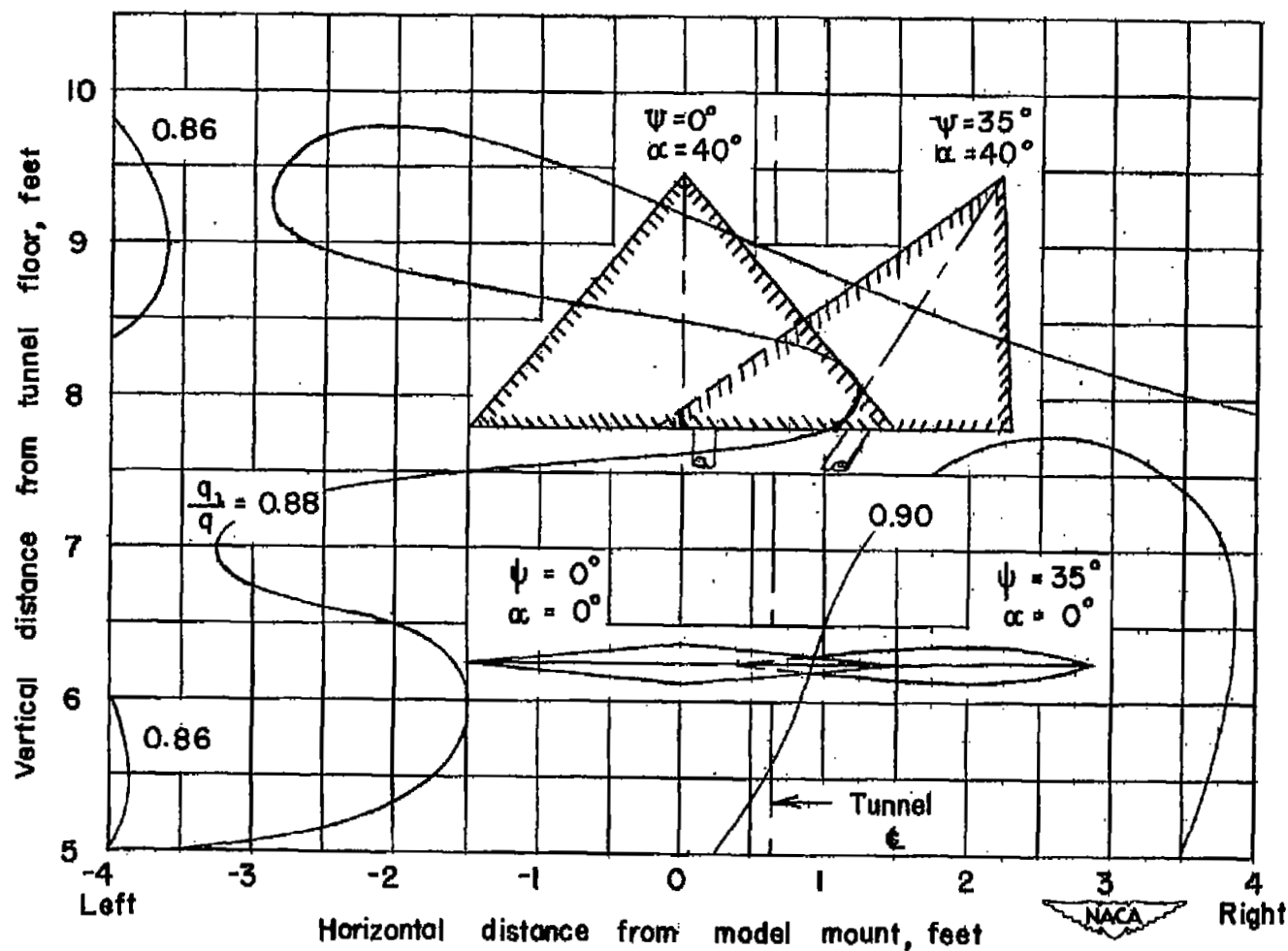


Figure 4.- Distribution of the  $q_1/q$  ratio of the air stream in a vertical plane located approximately 7 inches behind the apexes of the wings when  $\psi = 0^\circ$  and  $\alpha = 0^\circ$  and some representative positions of wing 2 in the surveyed plane.

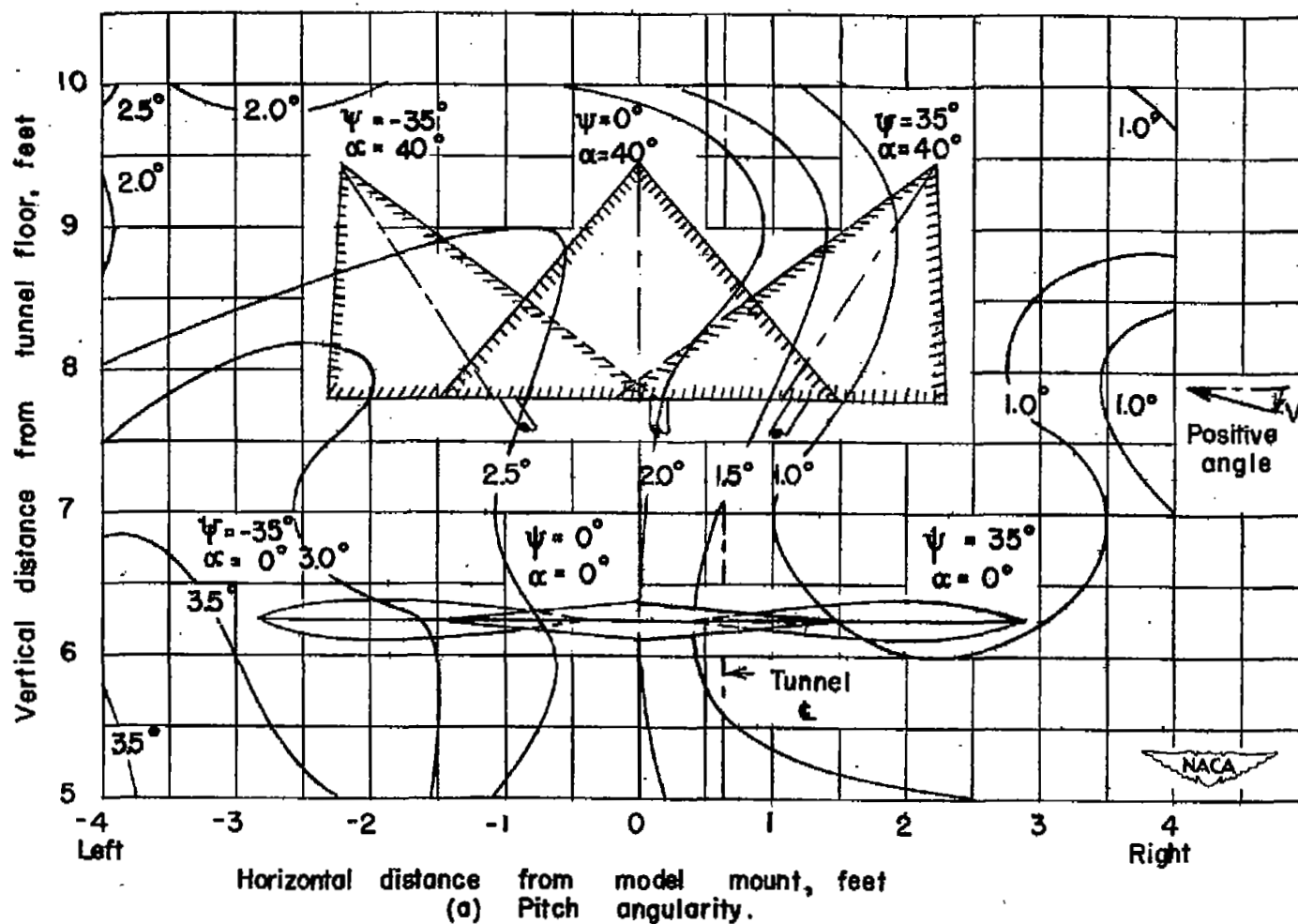
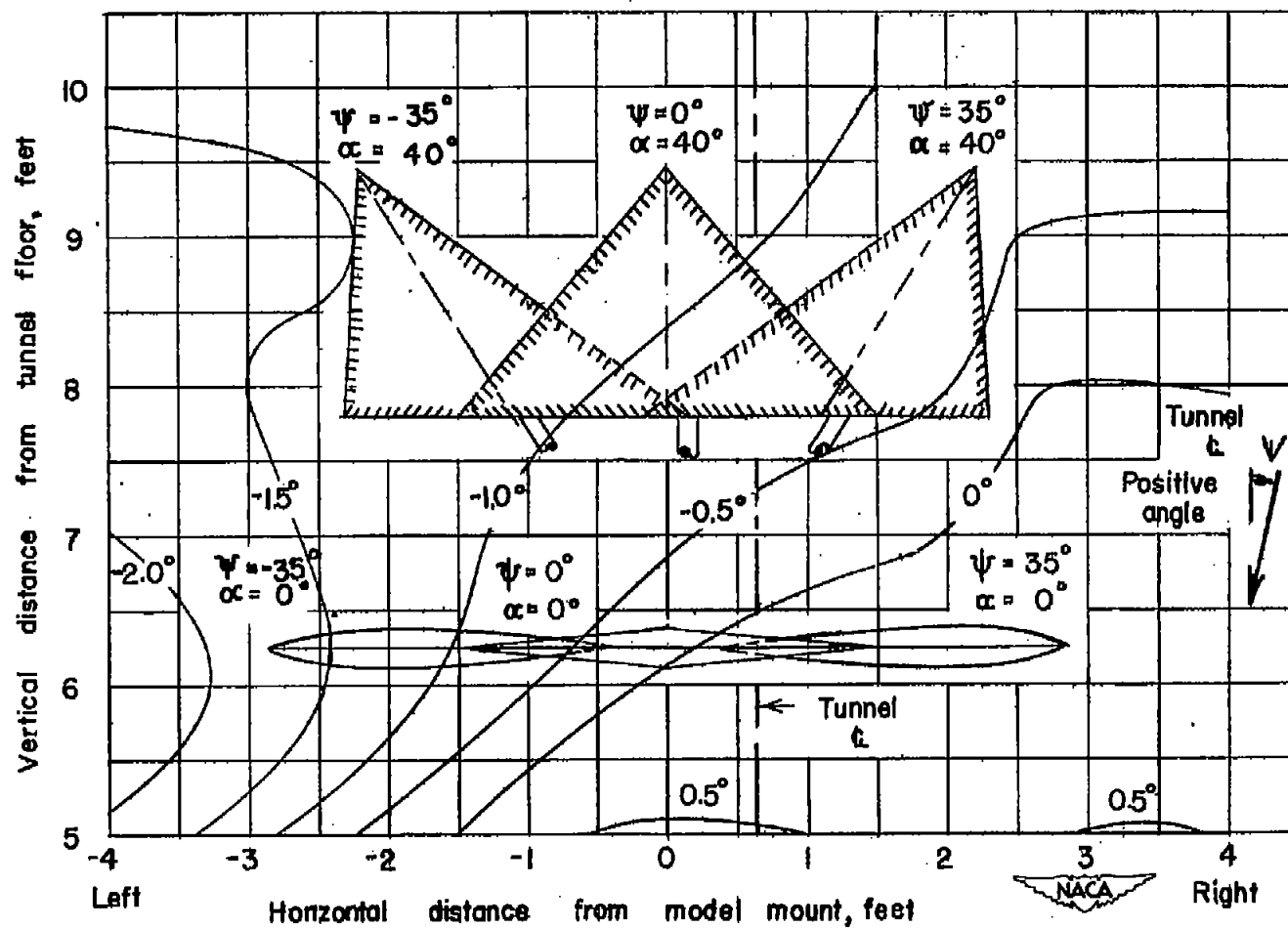
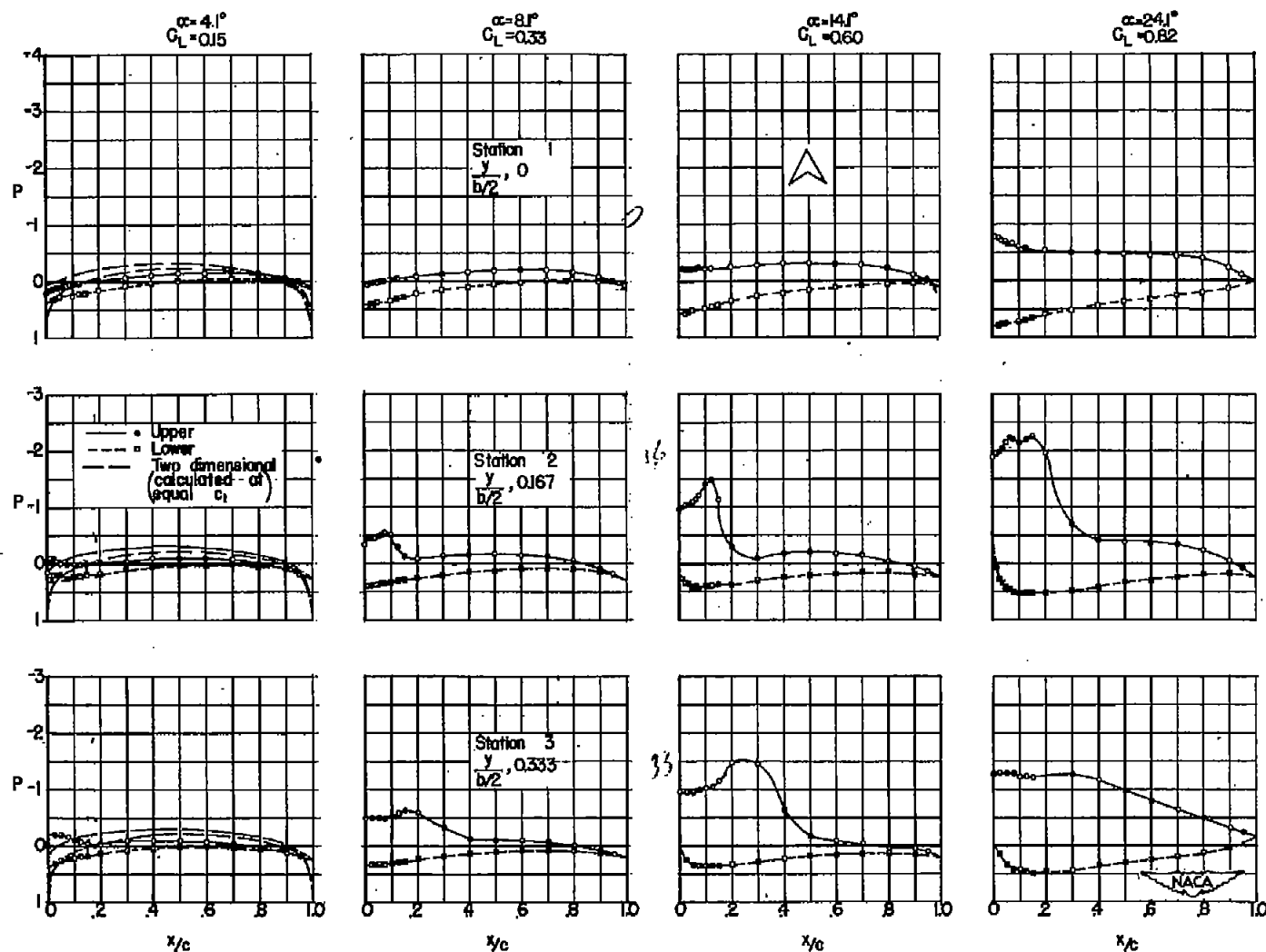


Figure 5.- Angularity of the air stream in a vertical plane located approximately 7 inches behind the apexes of the wings when  $\psi = 0^\circ$  and  $\alpha = 0^\circ$  and some representative positions of wing 2 in the surveyed plane.



(b) Yaw angularity.

Figure 5.- Concluded.



(a) Stations, 1,2,3.

Figure 6.- Chordwise pressure distribution about wing 1 at angles of attack of  $4.1^\circ$ ,  $8.1^\circ$ ,  $14.1^\circ$ , and  $24.1^\circ$ .

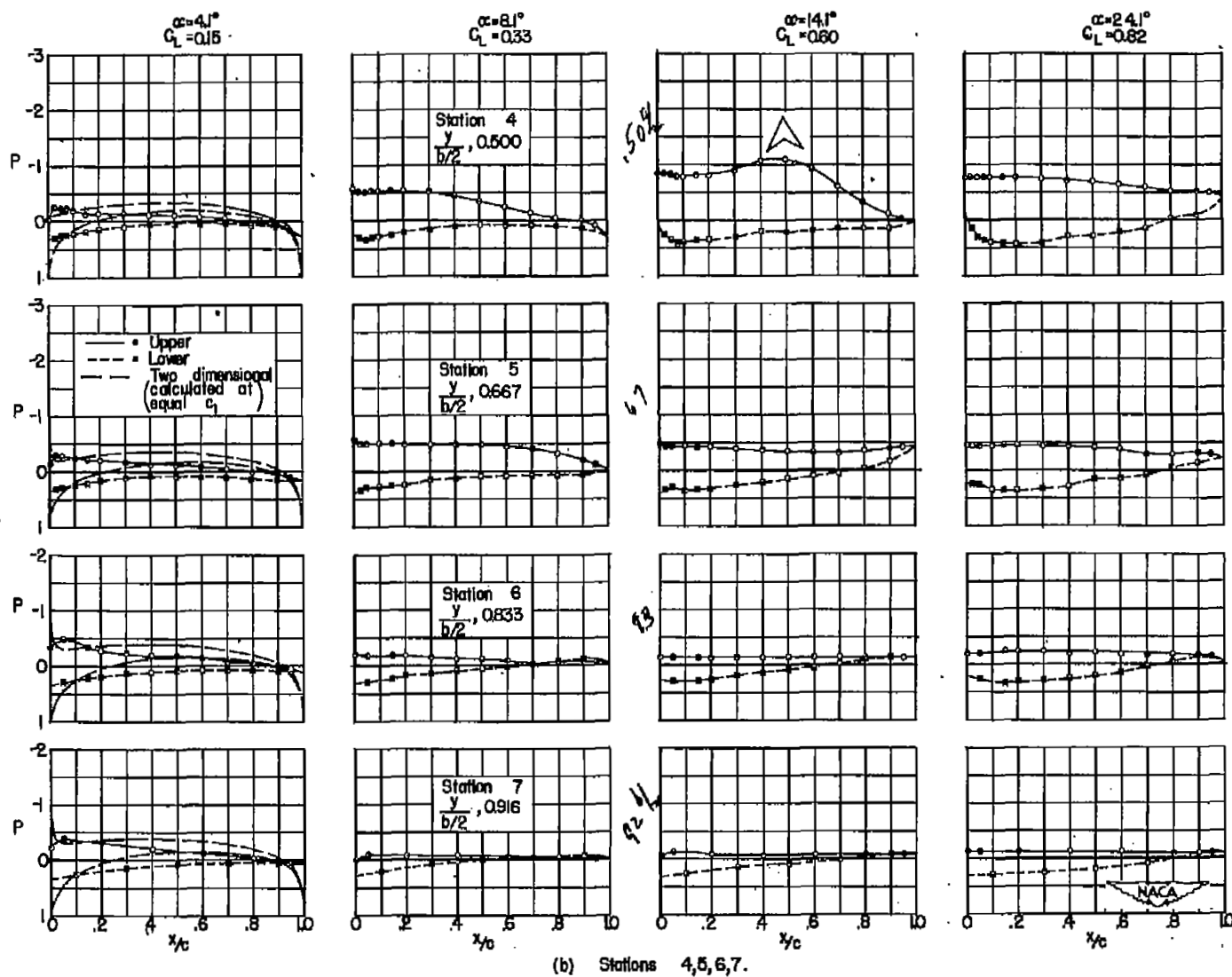


Figure 6.- Concluded.

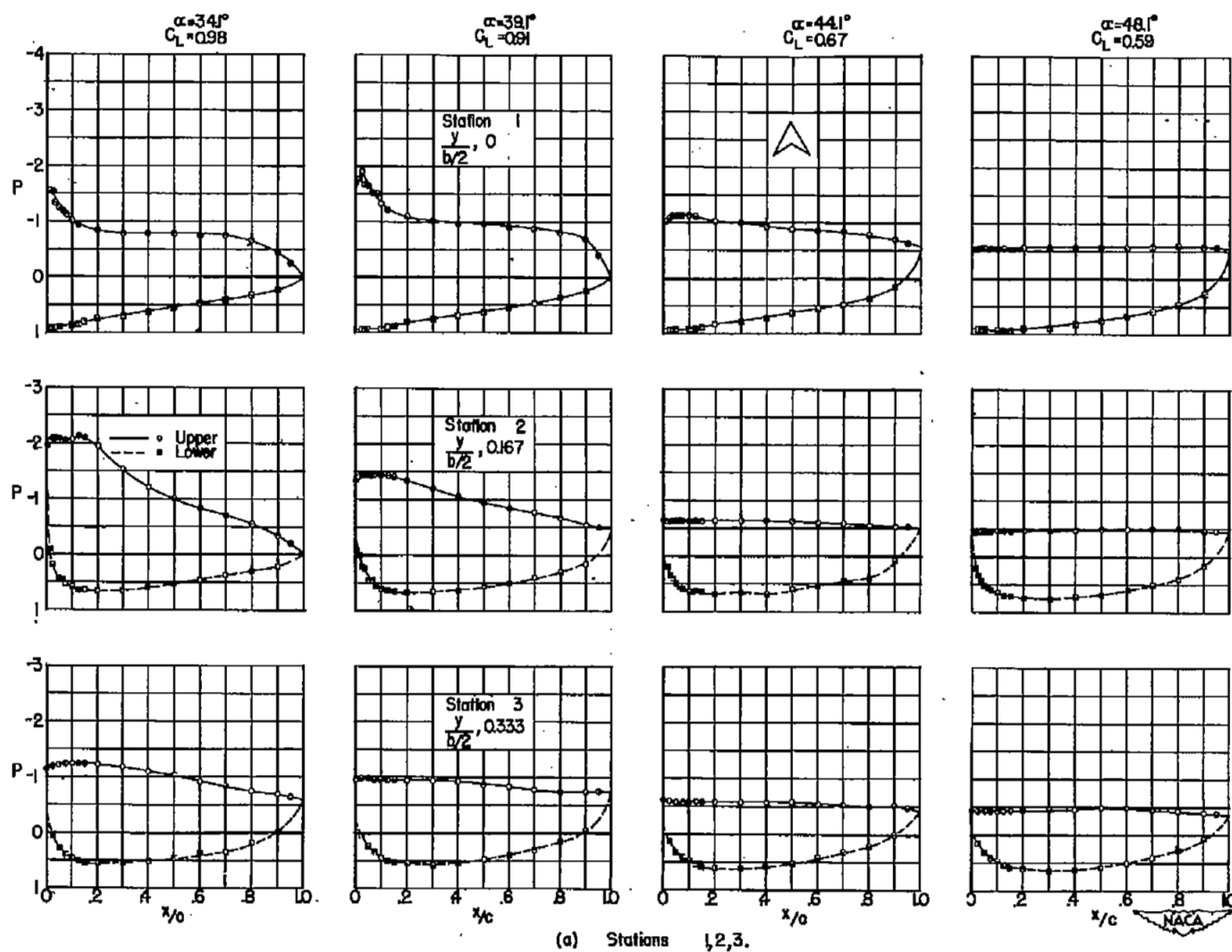
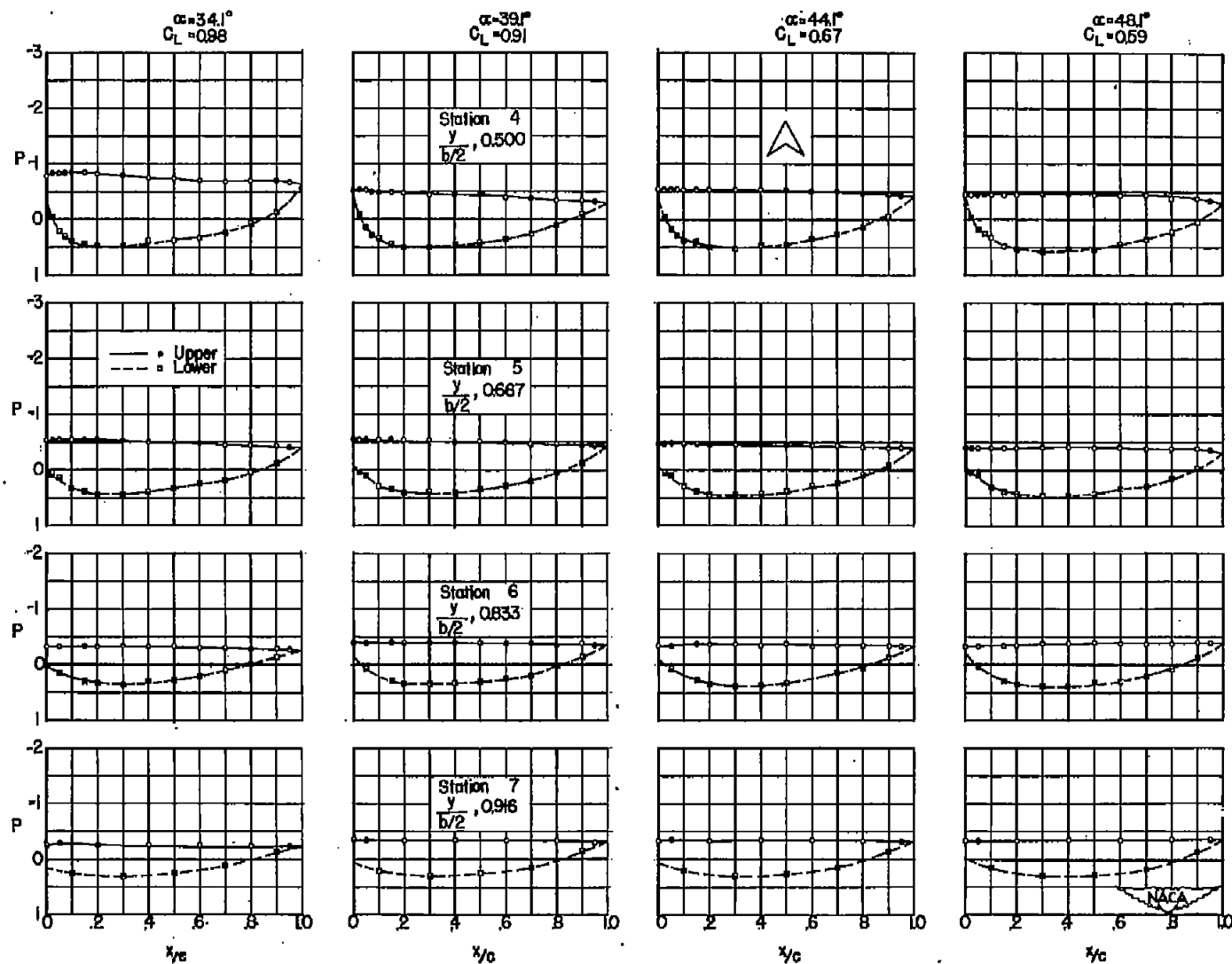


Figure 7.- Chordwise pressure distribution about wing 1 at angles of attack of  $34.1^\circ$ ,  $39.1^\circ$ ,  $44.1^\circ$ , and  $48.1^\circ$ .



(d) Stations: 4,5,6,7.

Figure 7.- Concluded.

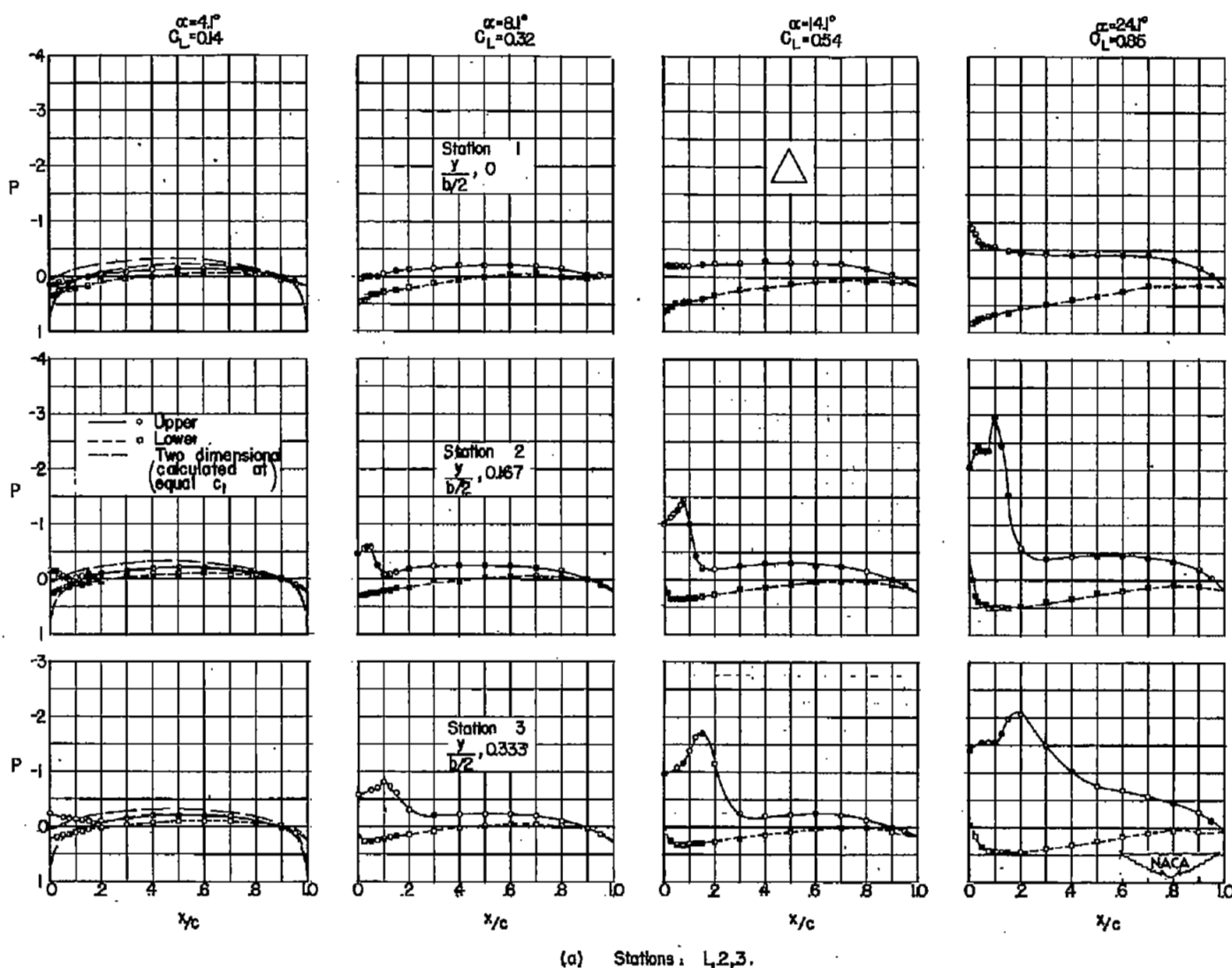
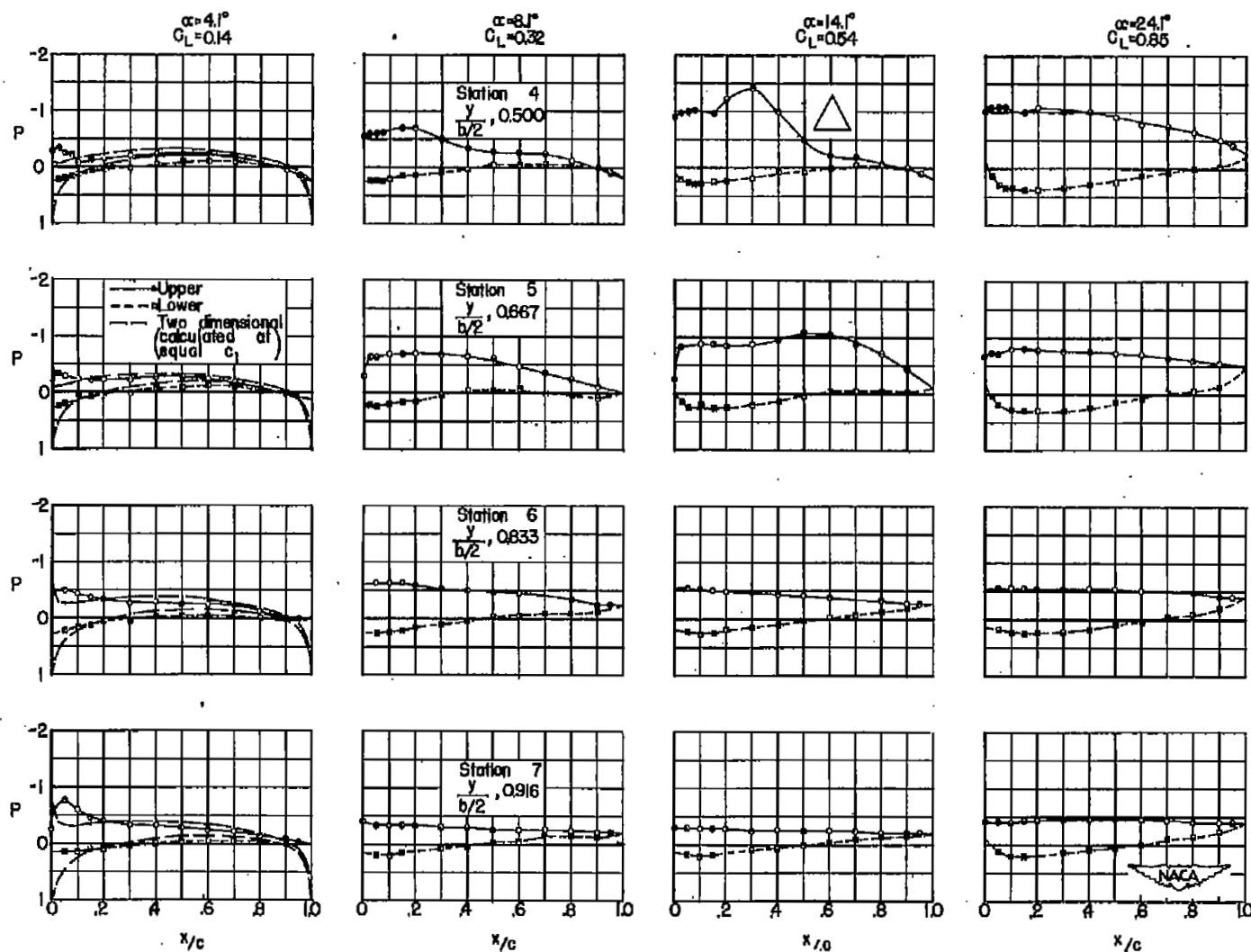


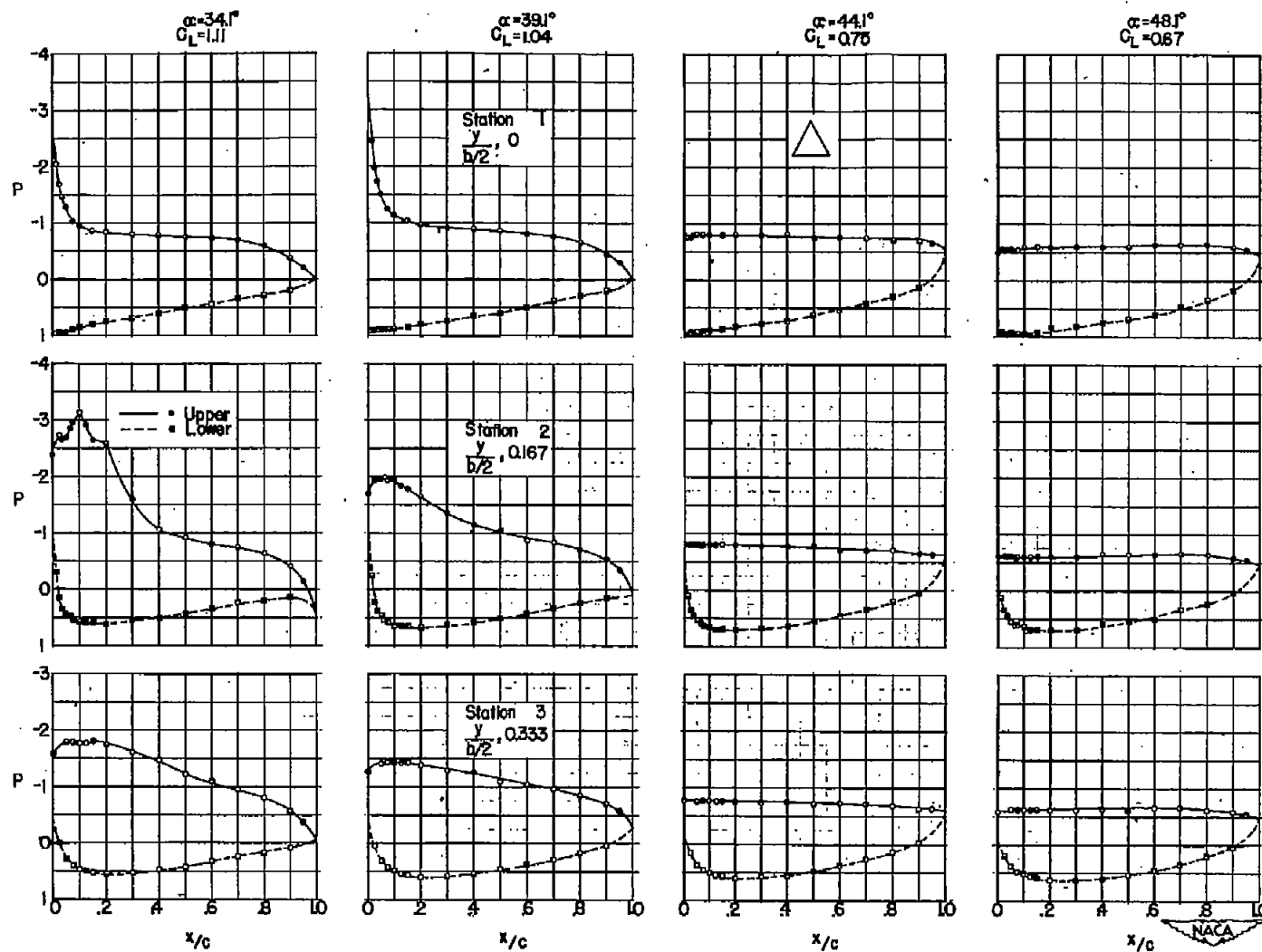
Figure 8.- Chordwise pressure distribution about wing 2 at angles of attack of  $4.1^\circ$ ,  $8.1^\circ$ ,  $14.1^\circ$ , and  $24.1^\circ$ .





(b) Stations, 4,5,6,7.

Figure 8.- Concluded.



(a) Stations 1, 2, 3.

Figure 9.- Chordwise pressure distribution about wing 2 at angles of attack of  $34.1^\circ$ ,  $39.1^\circ$ ,  $44.1^\circ$ , and  $48.1^\circ$ .

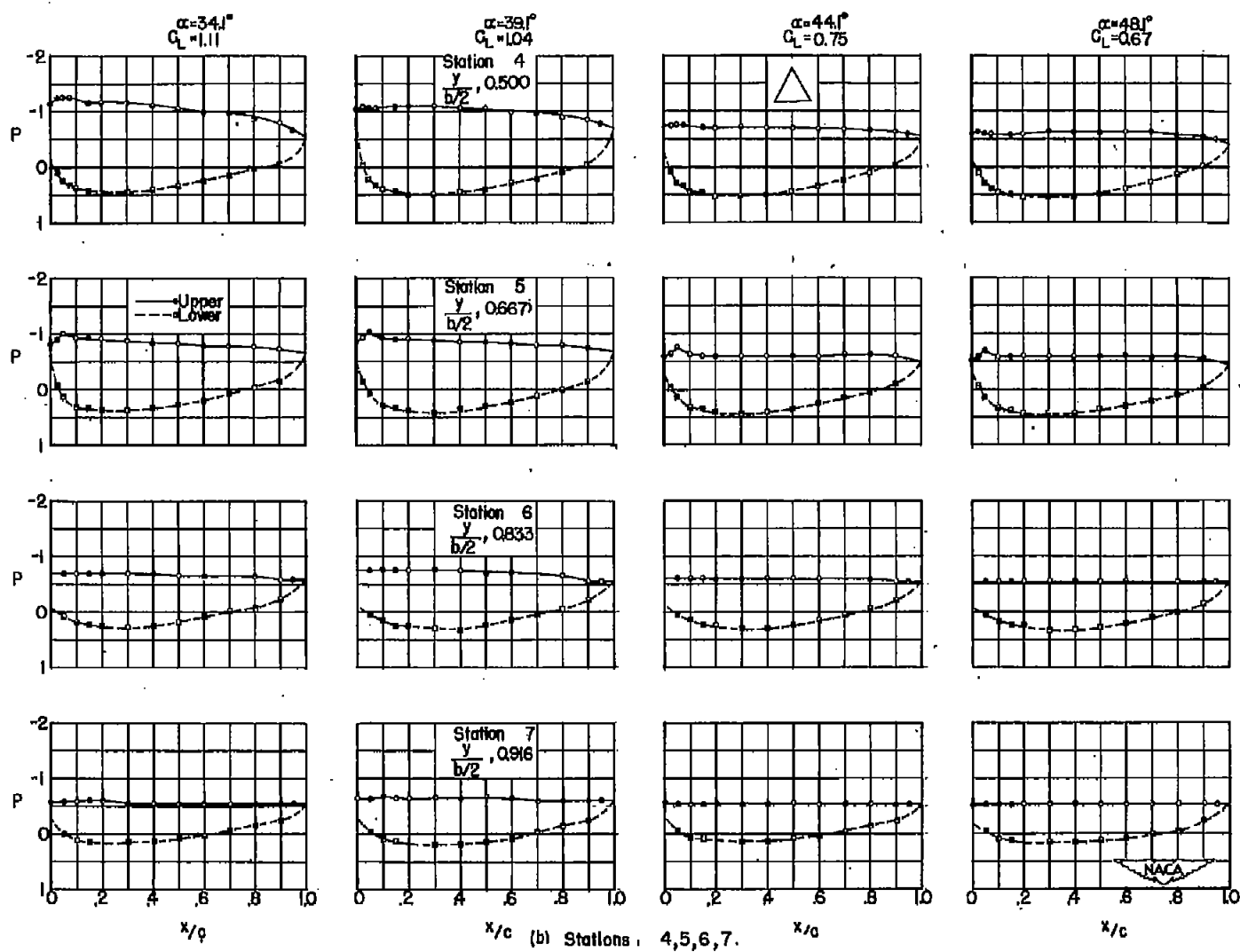


Figure 9.- Concluded.

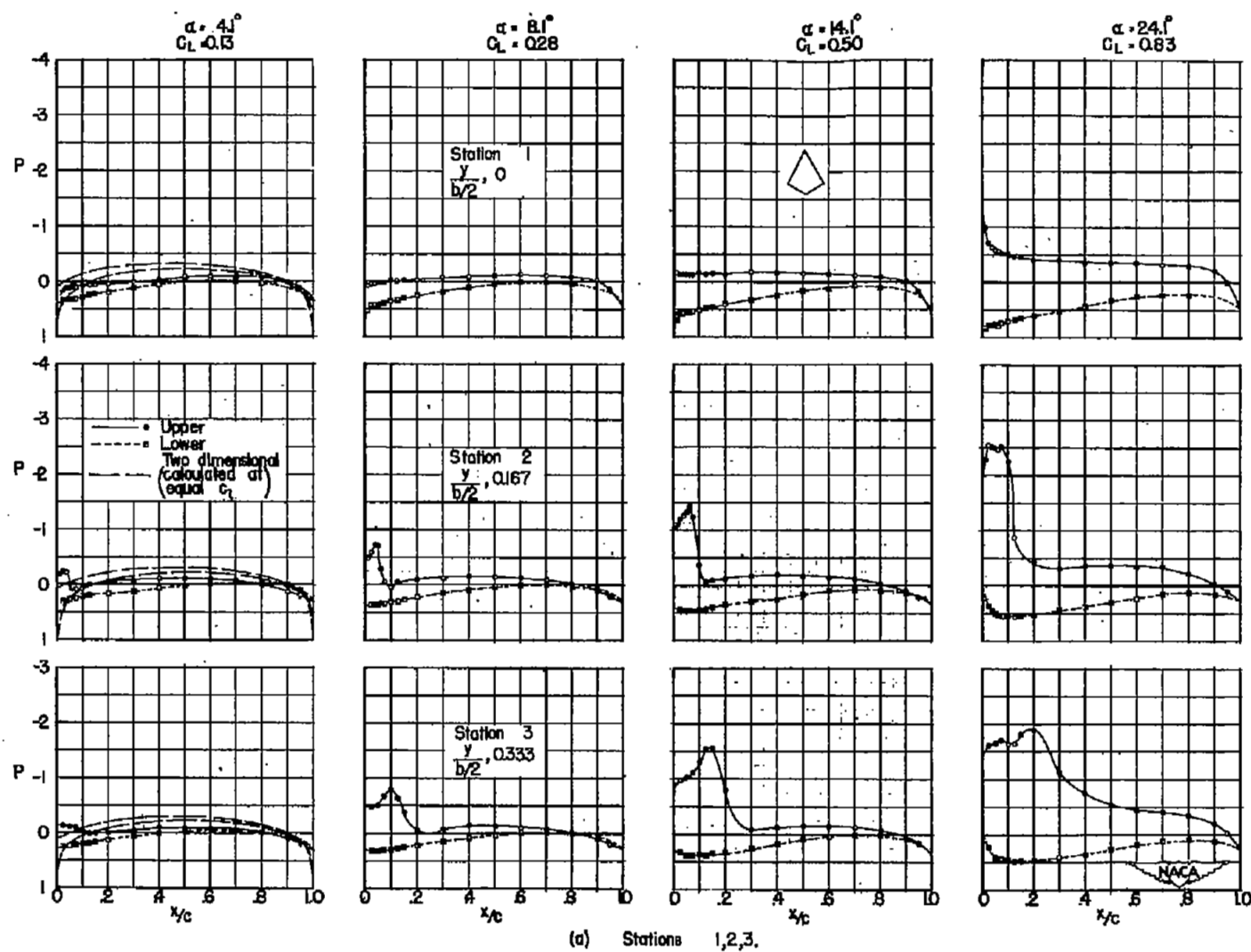
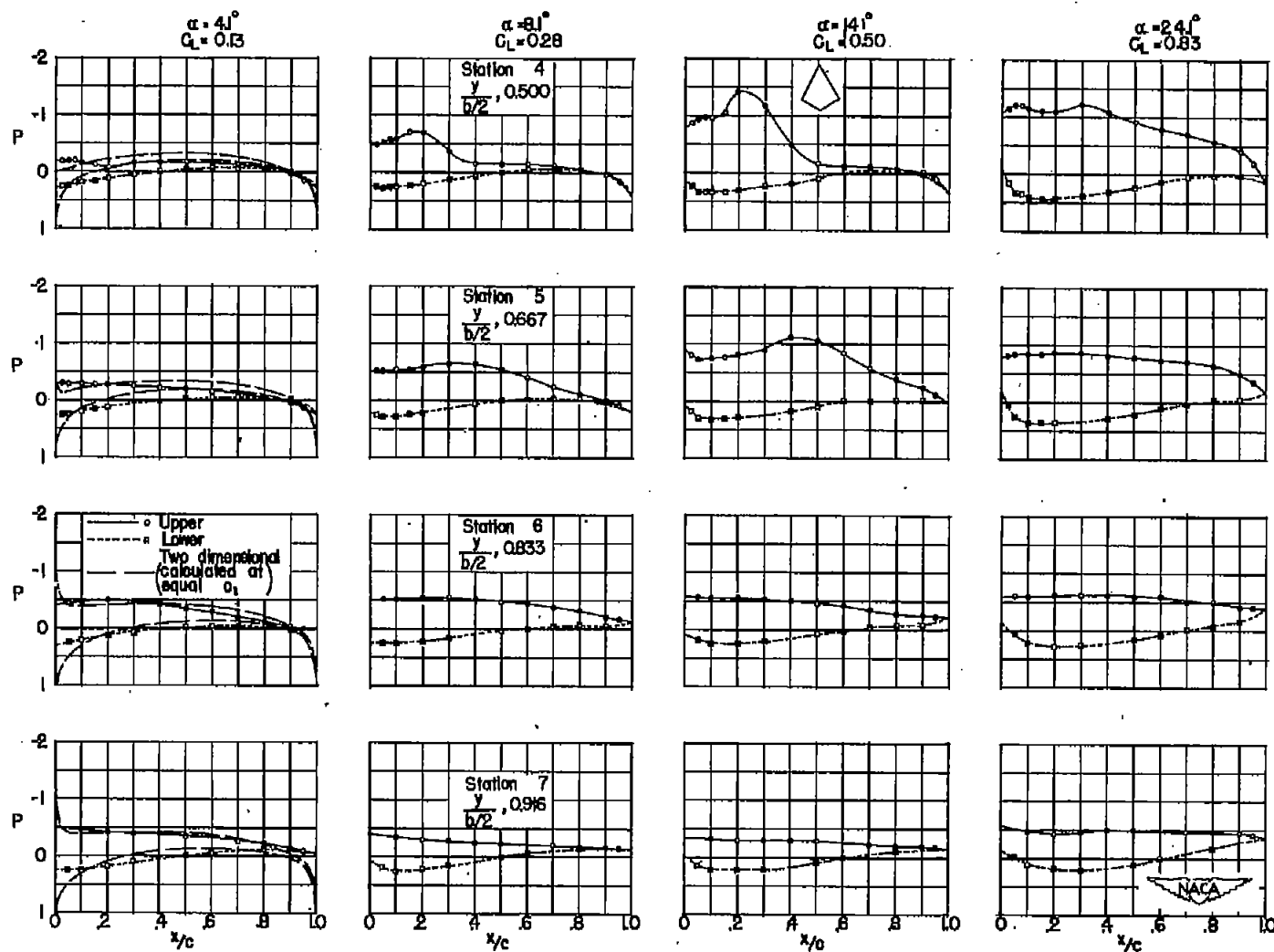


Figure 10.- Chordwise pressure distribution about wing 3 at angles of attack of  $4.1^\circ$ ,  $8.1^\circ$ ,  $14.1^\circ$ , and  $24.1^\circ$ ;  $\psi = 0^\circ$ .



(b) Stations : 4,5,6,7.

Figure 10.- Concluded.

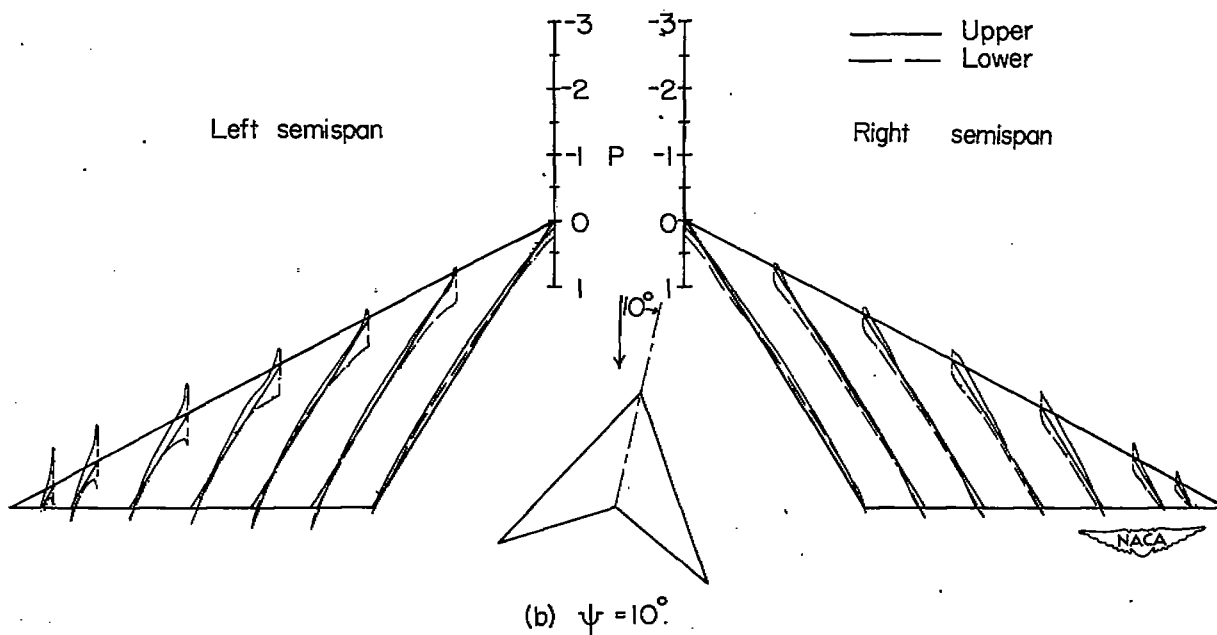
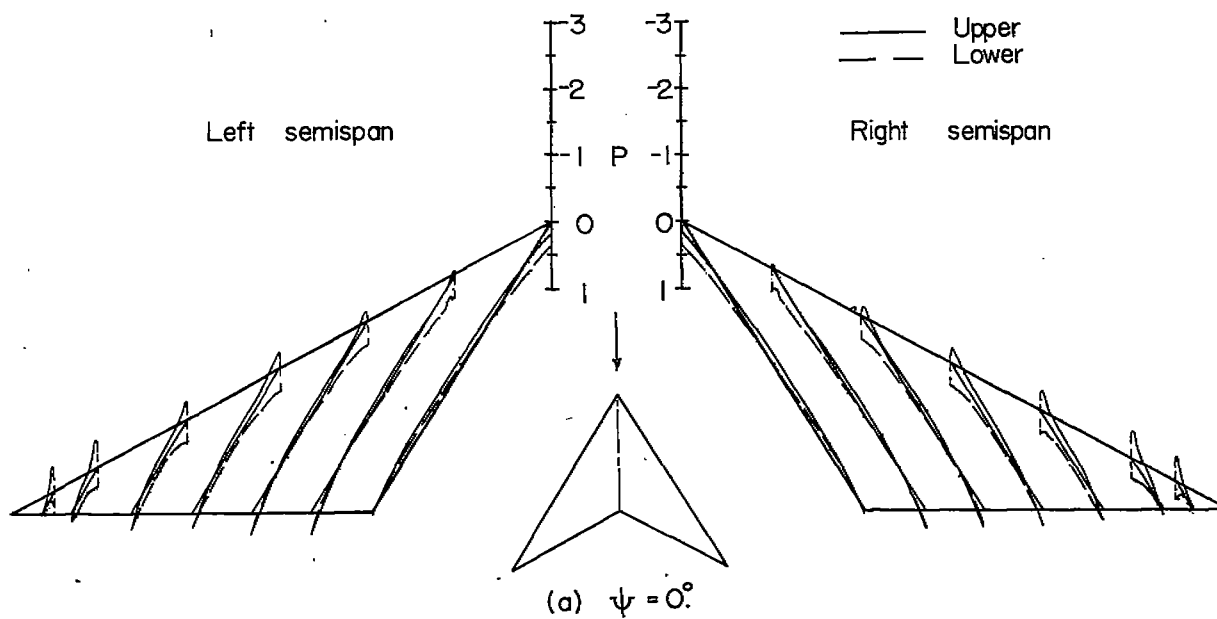


Figure 12.- Pressure distribution about wing 1 at various angles of yaw;  
 $\alpha = 4.1^\circ$ .

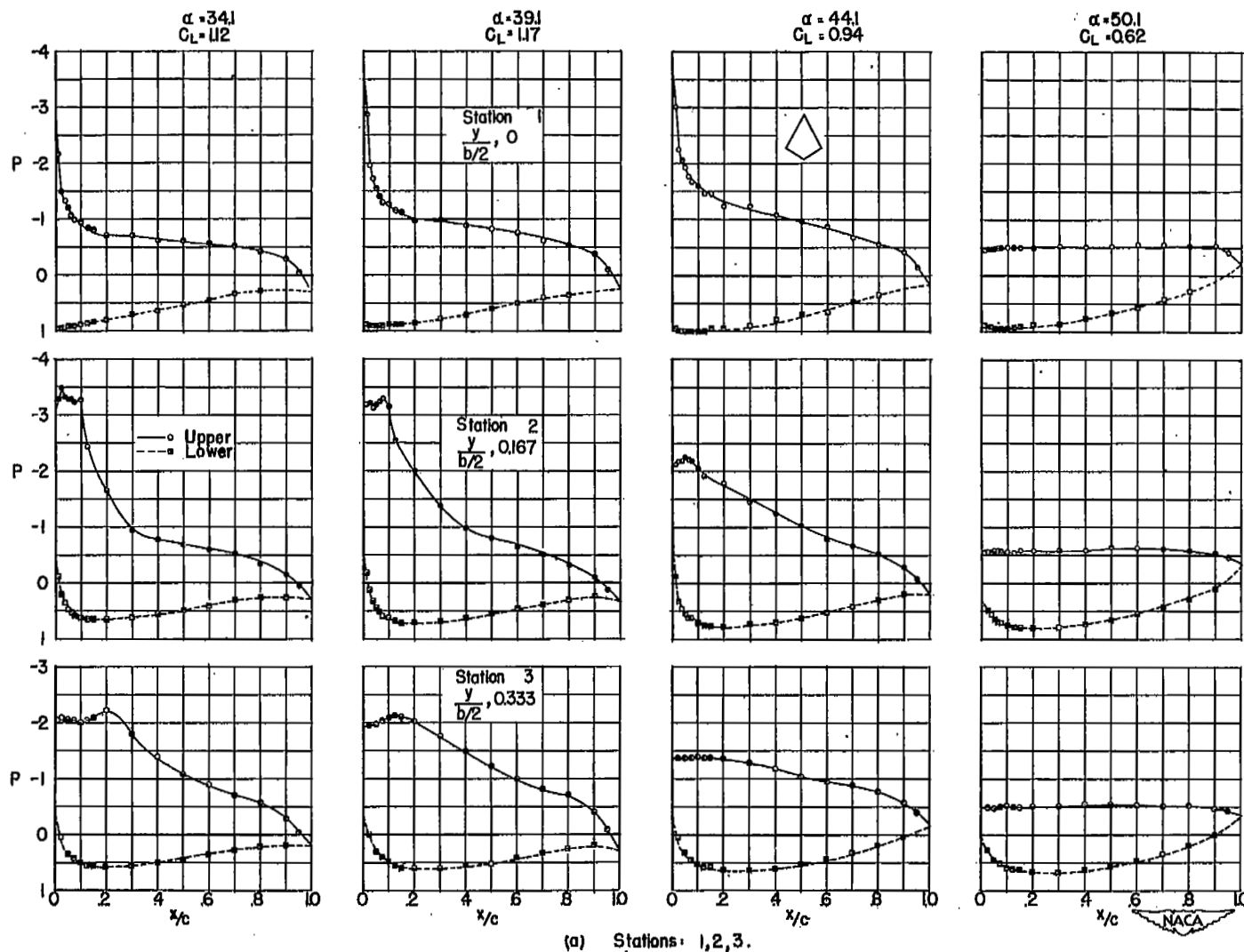
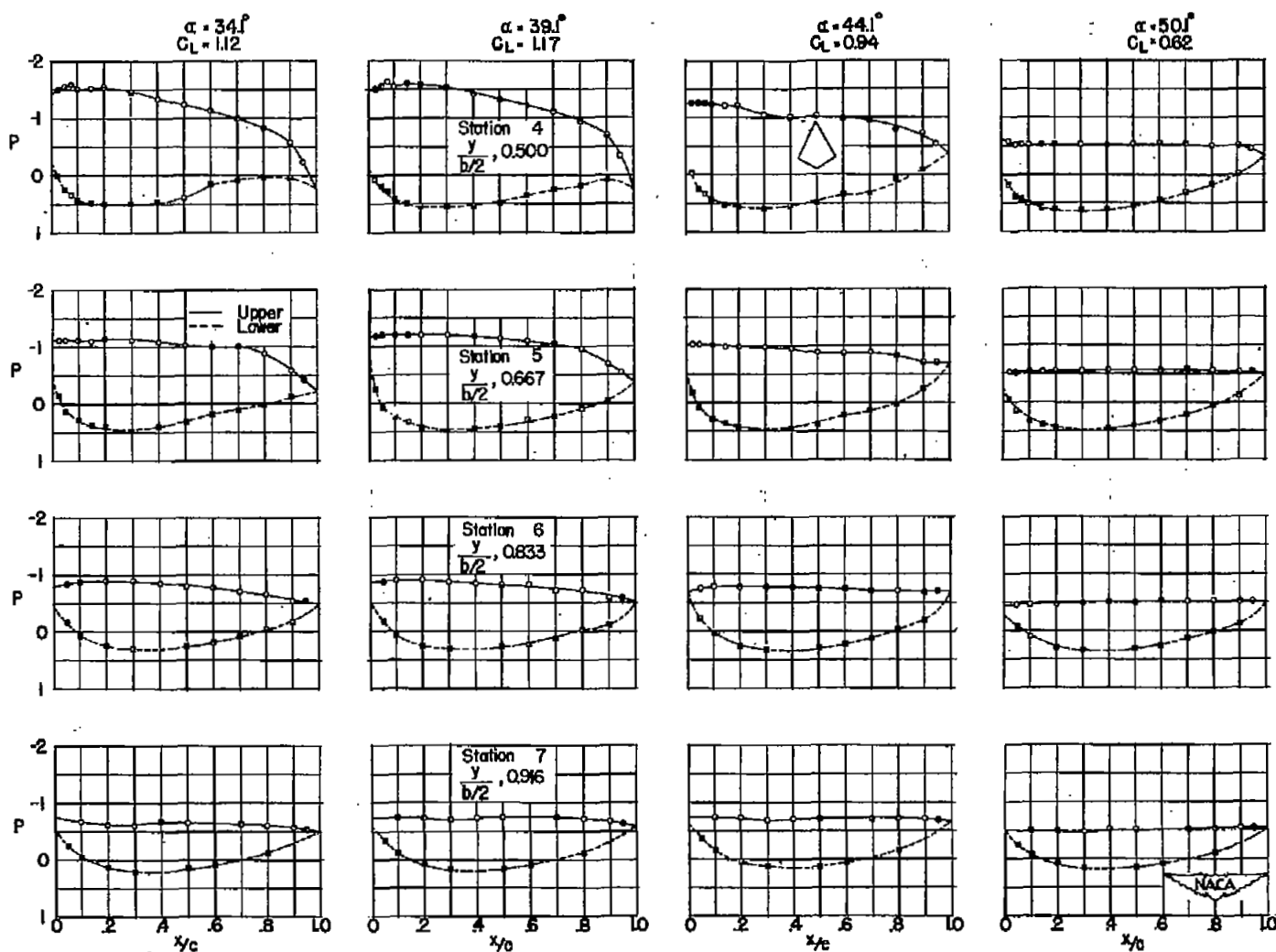


Figure 11.- Chordwise pressure distribution about wing 3 at angles of attack of 34.1°, 39.1°, 44.1°, and 50.1°;  $\psi = 0^\circ$ .



(b) Stations: 4, 5, 6, 7.

Figure 11.- Concluded.



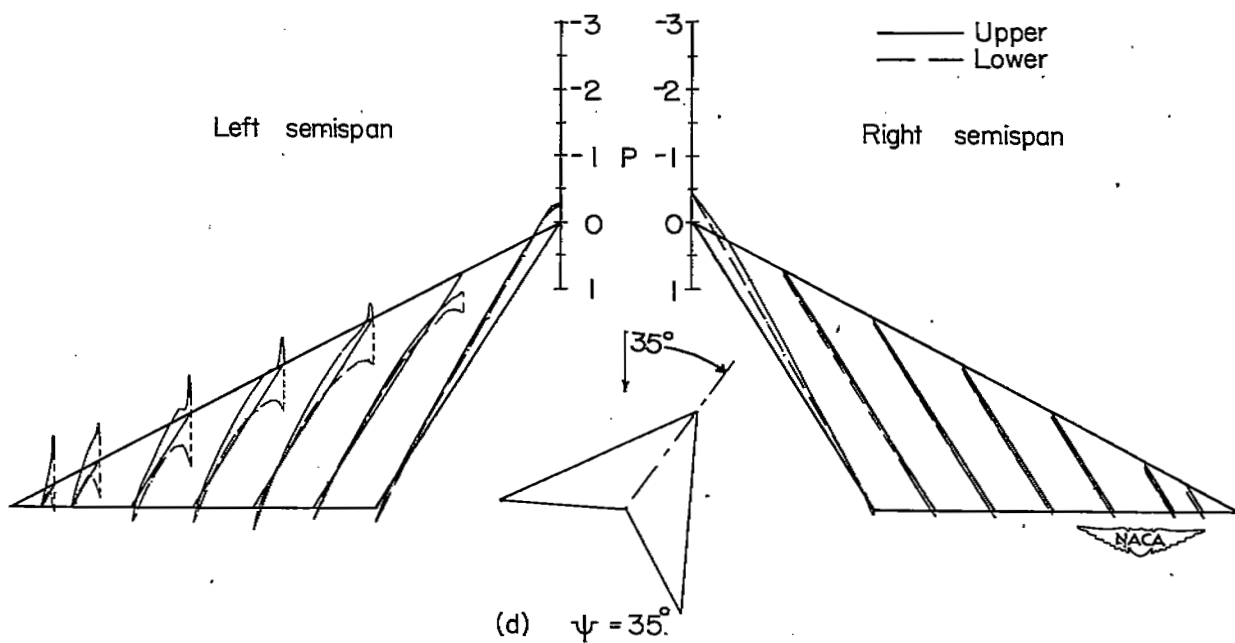
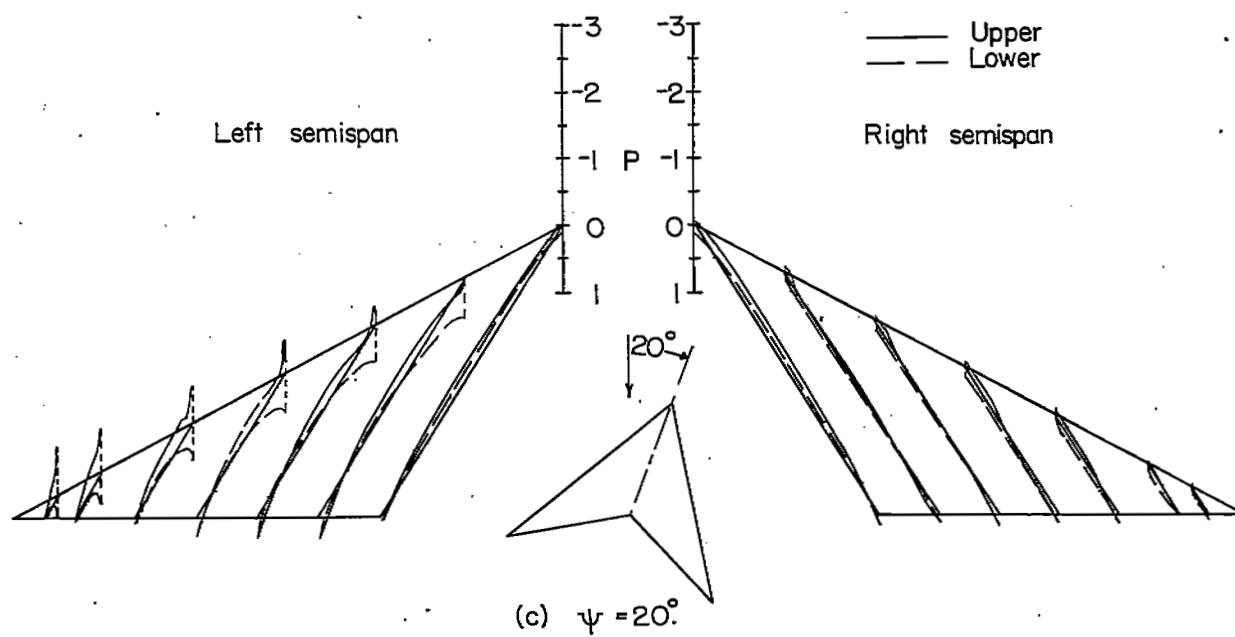


Figure 12.- Concluded.

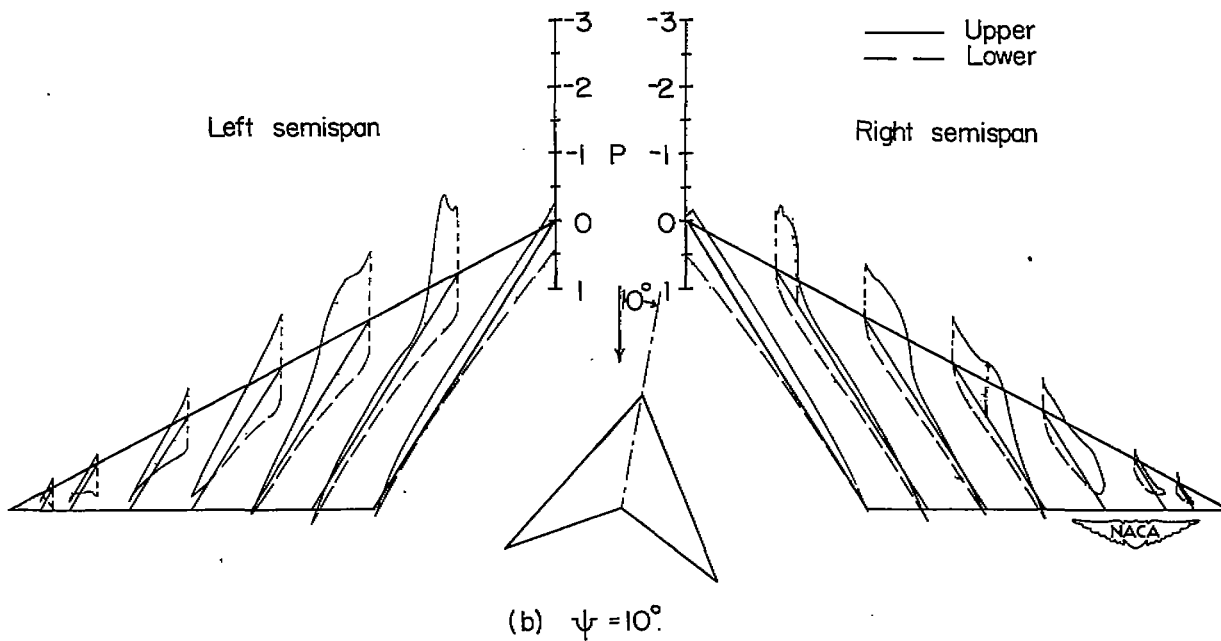
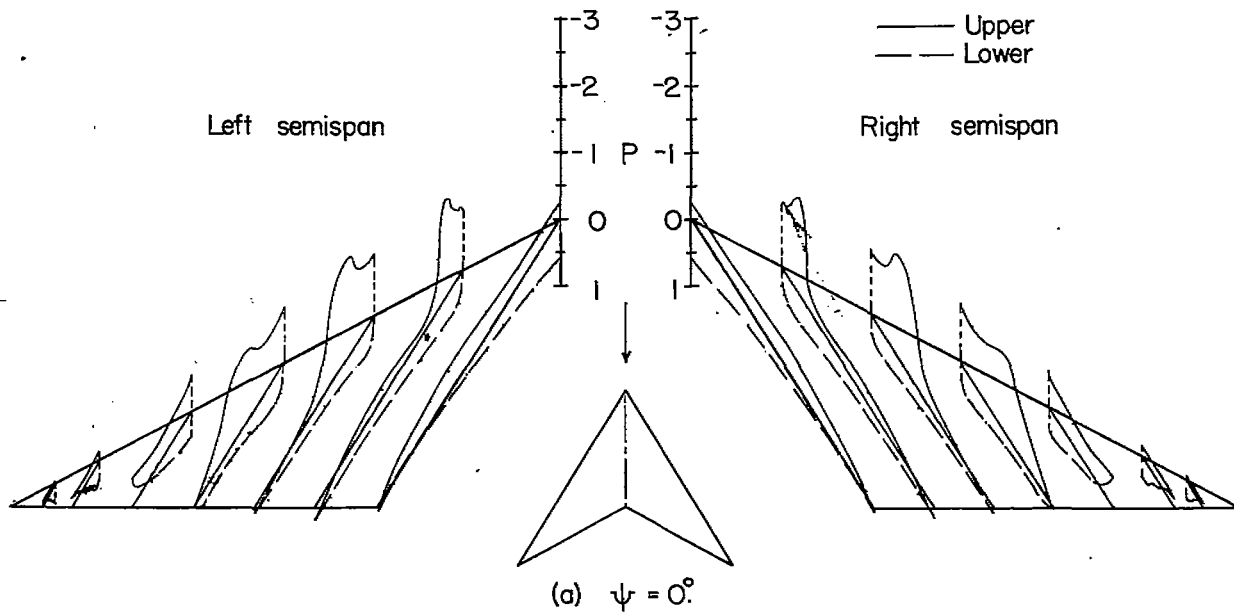


Figure 13.- Pressure distribution about wing 1 at various angles of yaw;  
 $\alpha = 14.1^\circ$ .

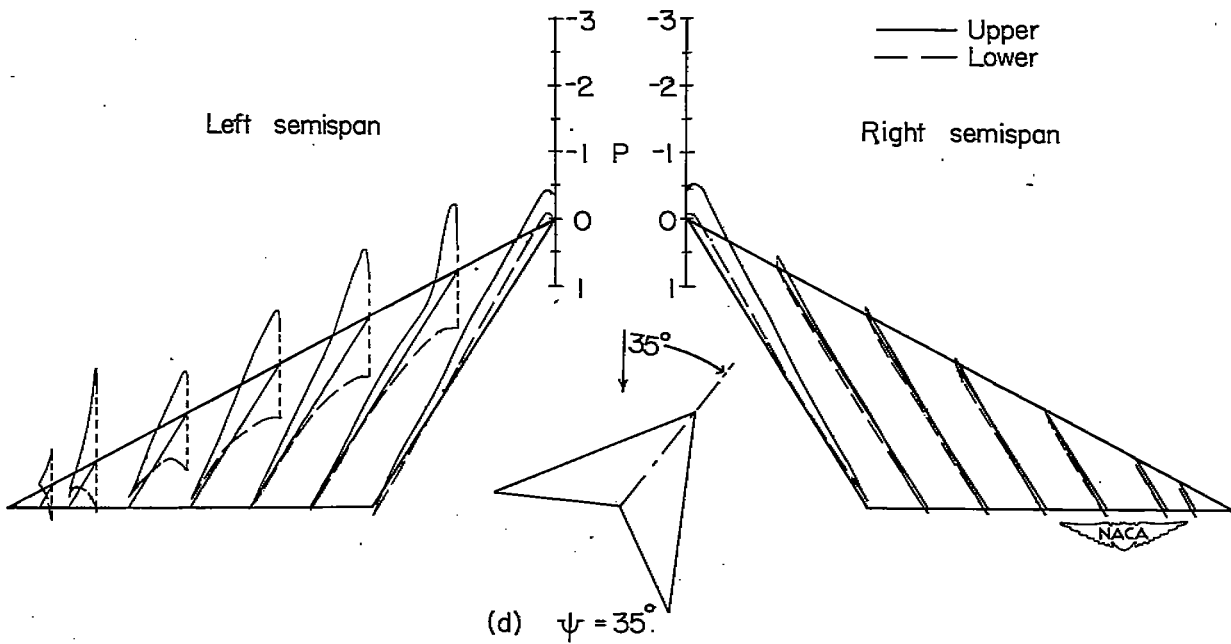
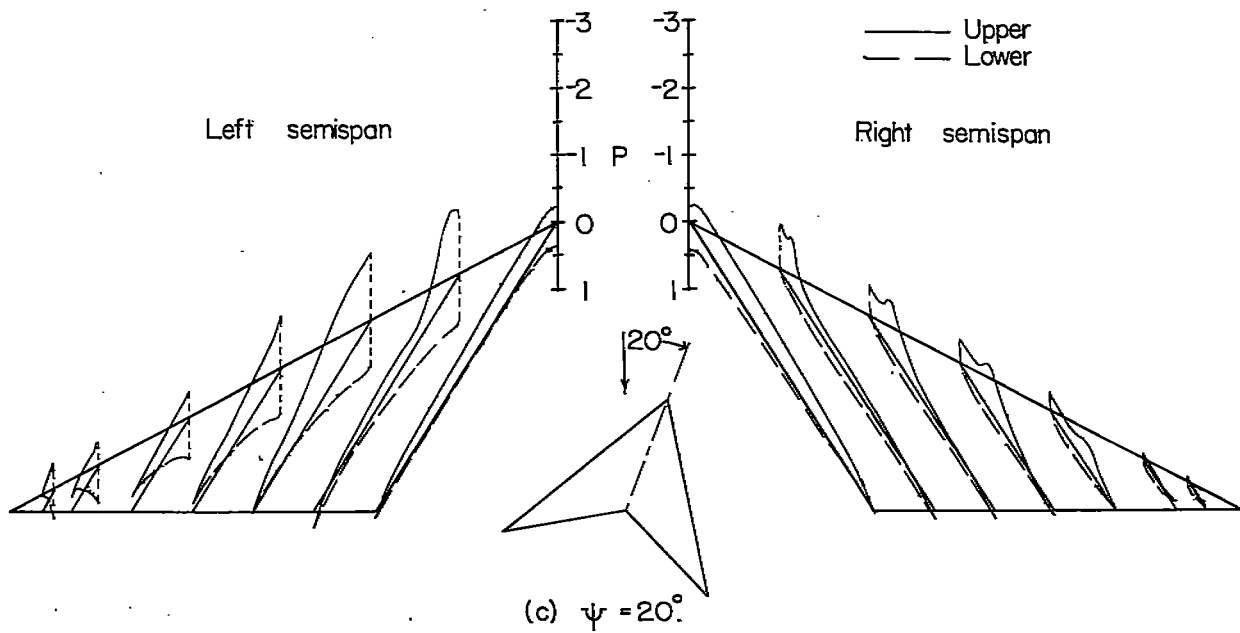


Figure 13.- Concluded.

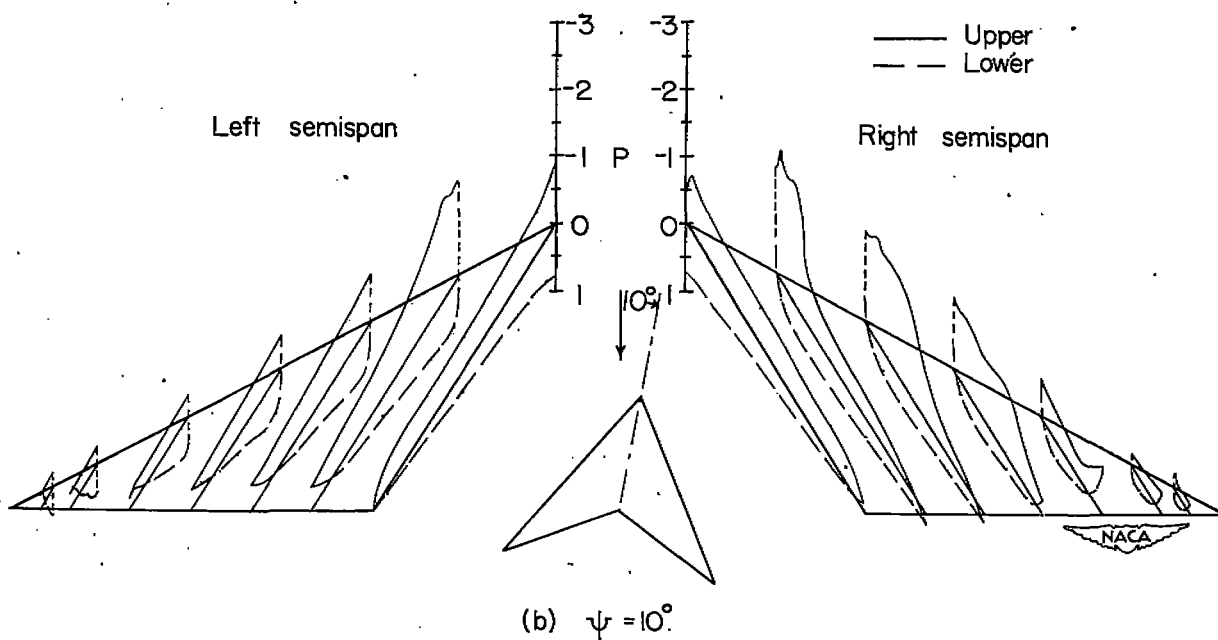
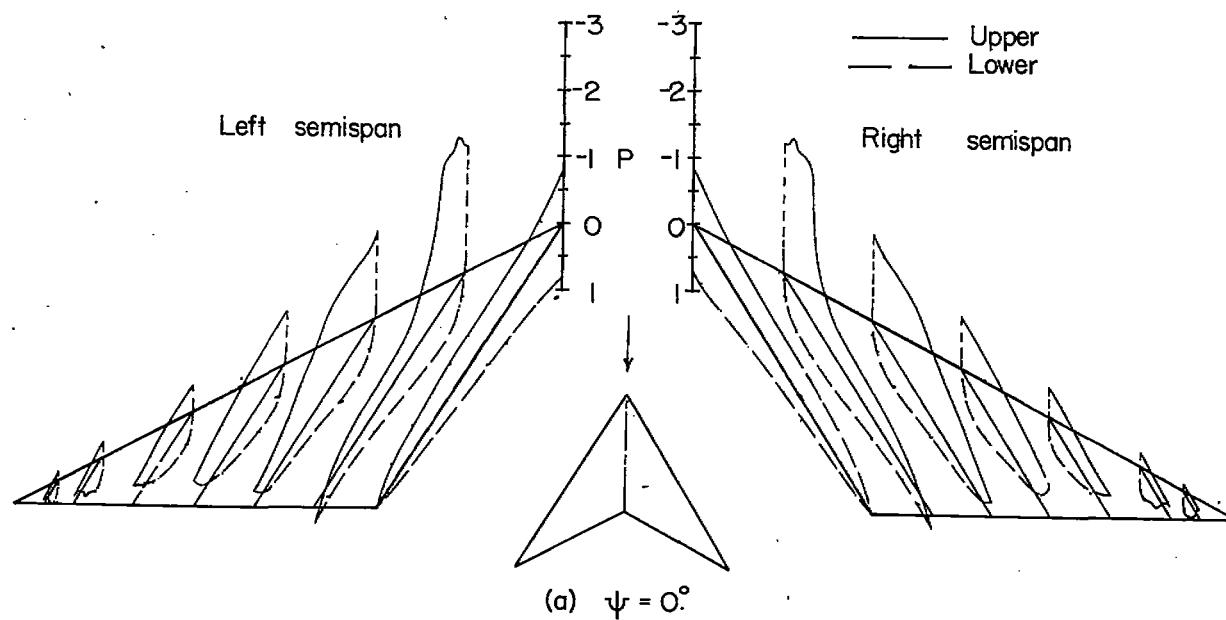


Figure 14.- Pressure distribution about wing 1 at various angles of yaw;  
 $\alpha = 24.1^\circ$ .

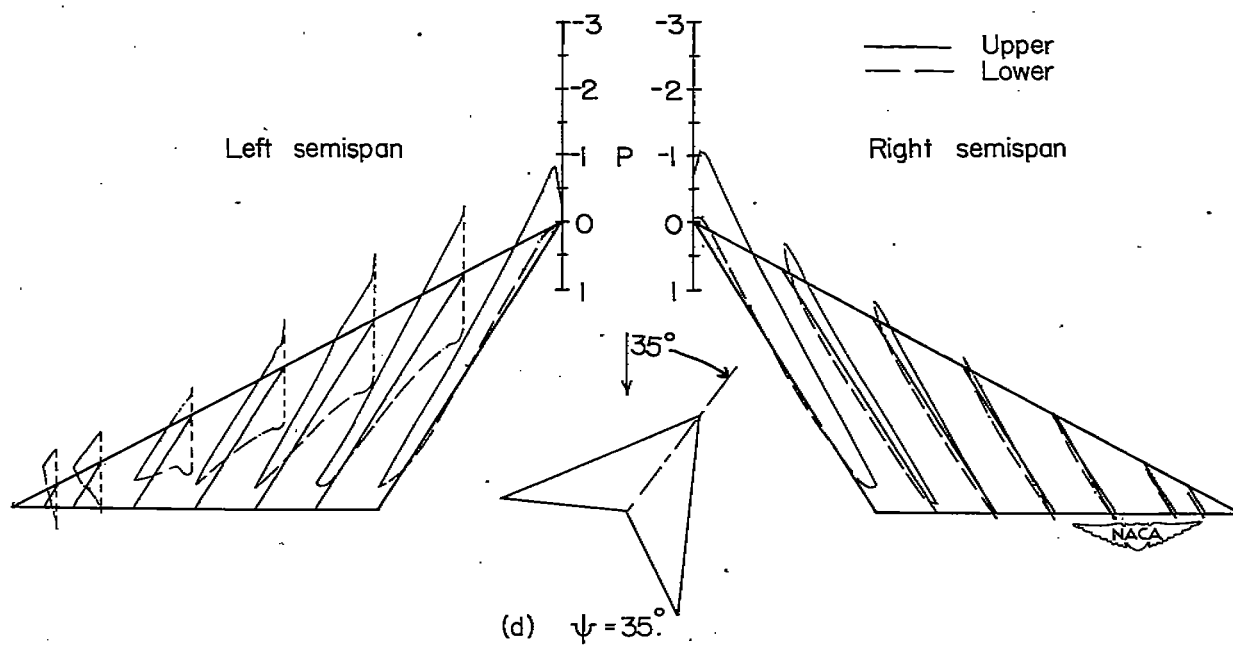
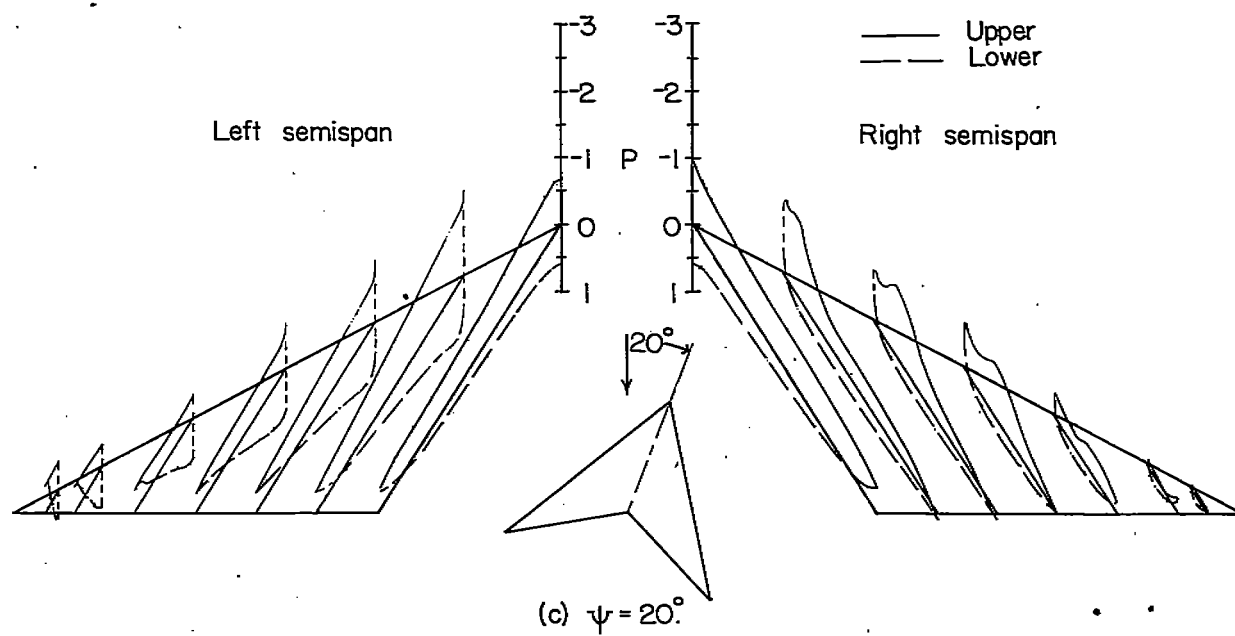


Figure 14.- Concluded.

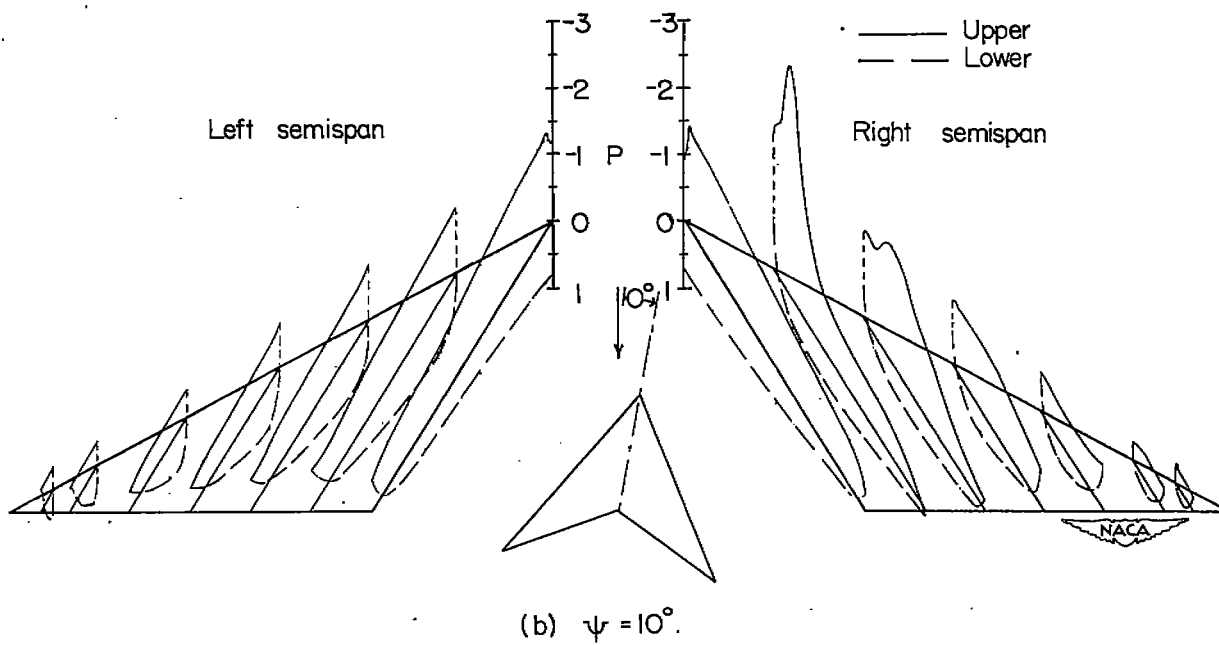
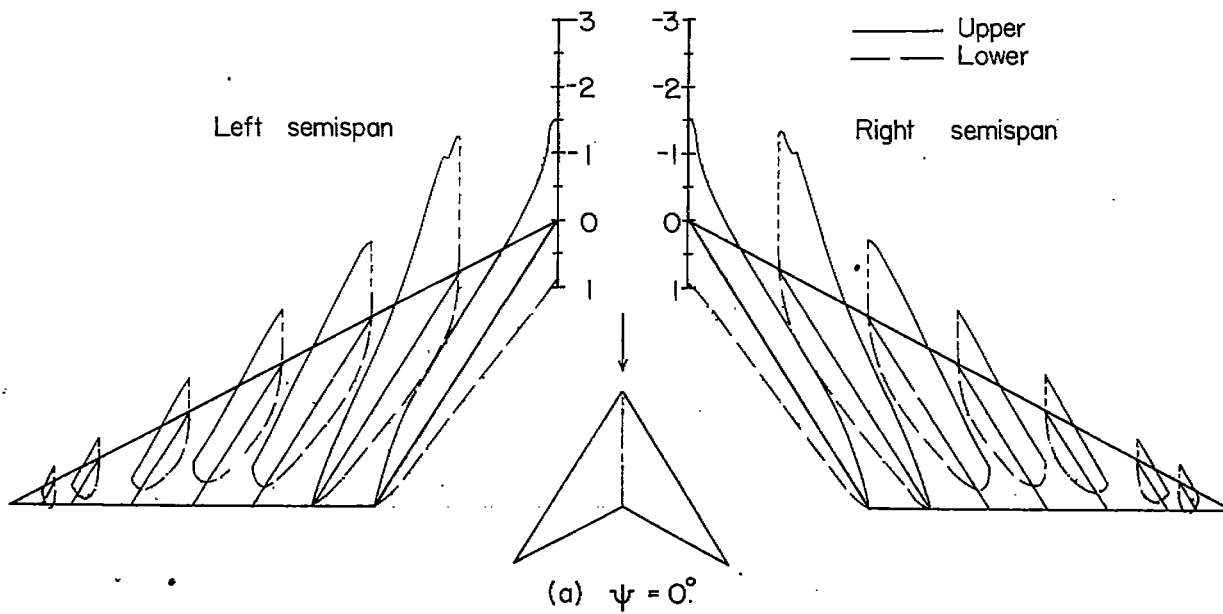


Figure 15.- Pressure distribution about wing 1 at various angles of yaw;  
 $\alpha = 34.1^\circ$ .

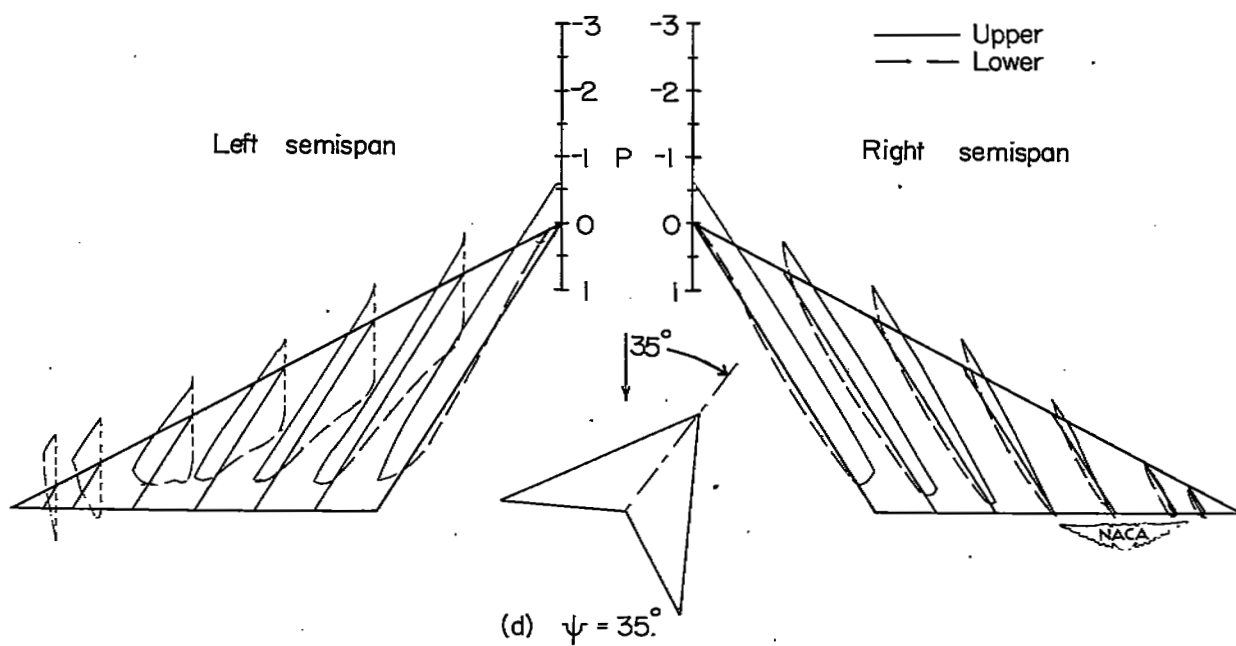
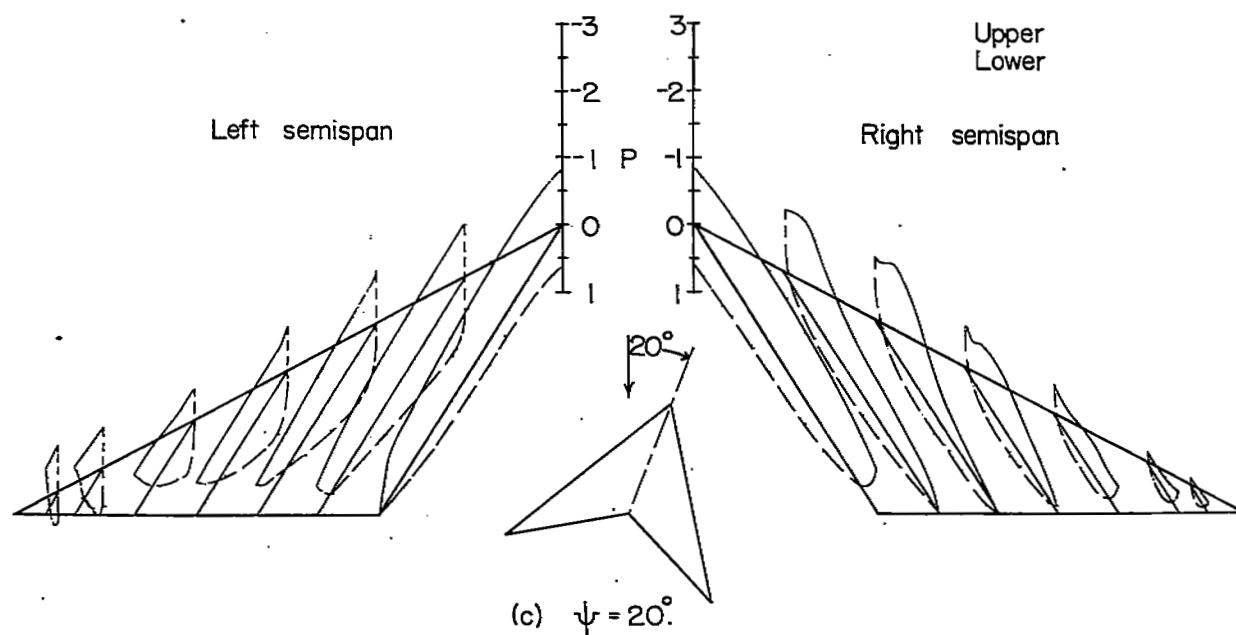


Figure 15.- Concluded.

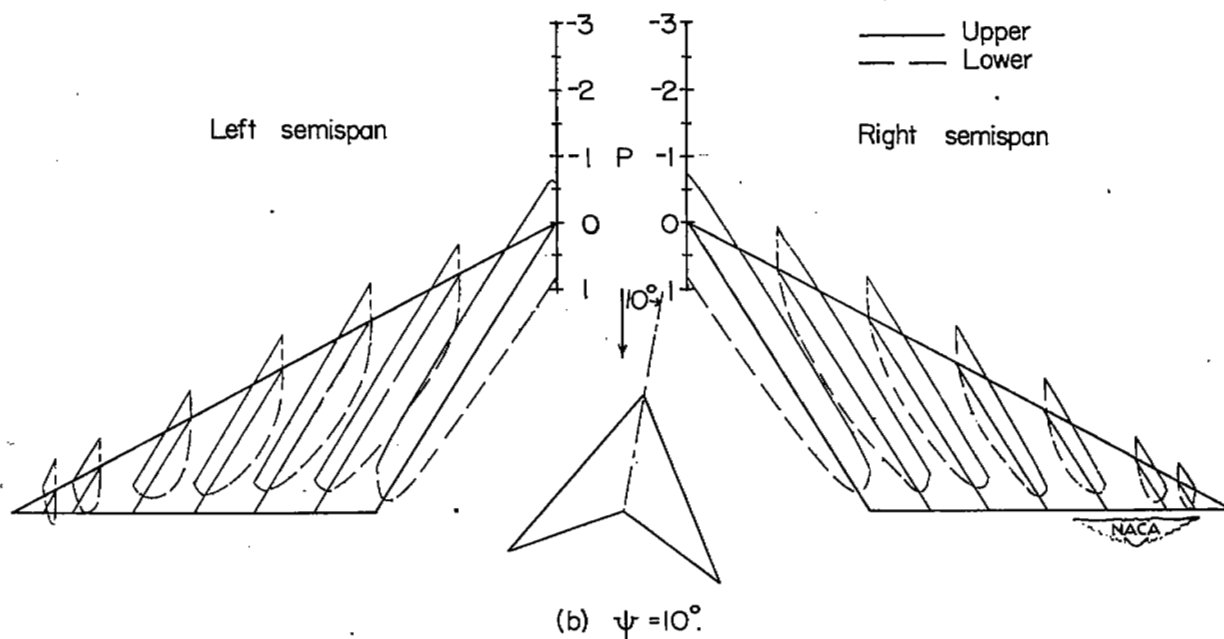
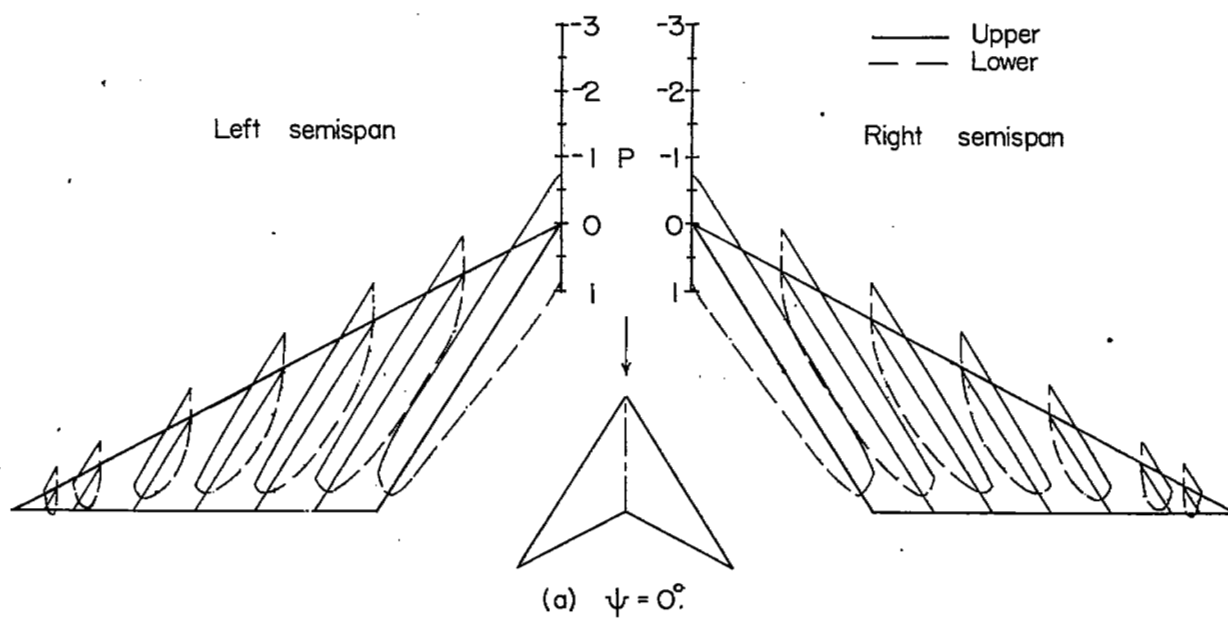


Figure 16.- Pressure distribution about wing 1 at various angles of yaw;  
 $\alpha = 44.1^\circ$ .



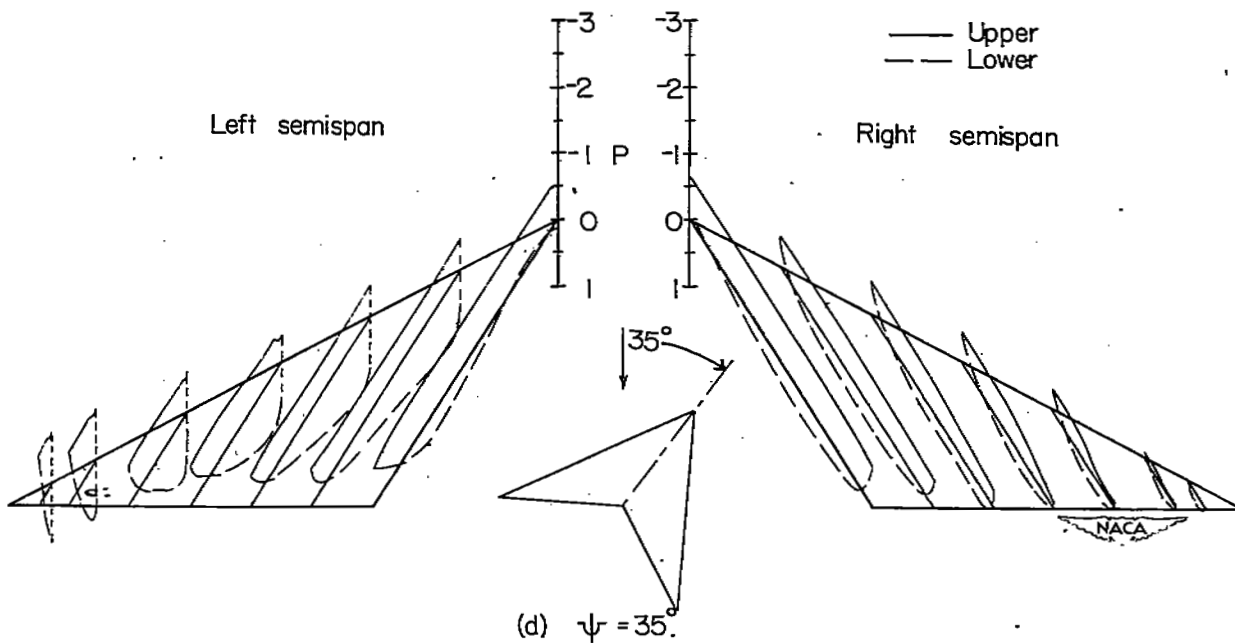
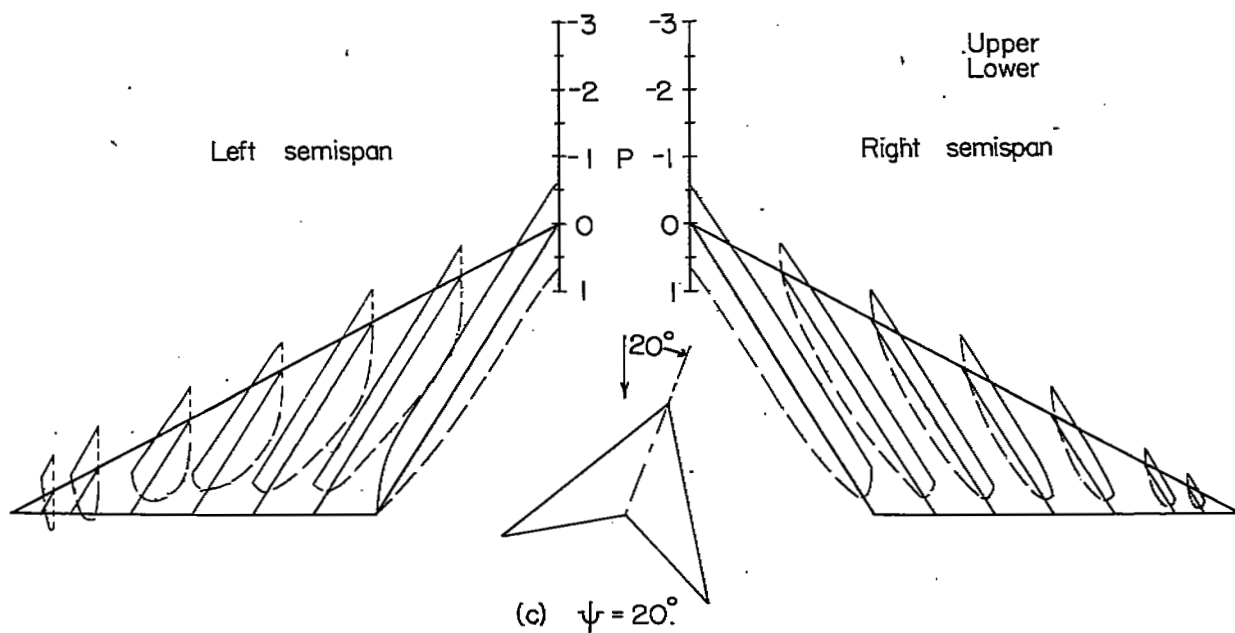


Figure 16.- Concluded.

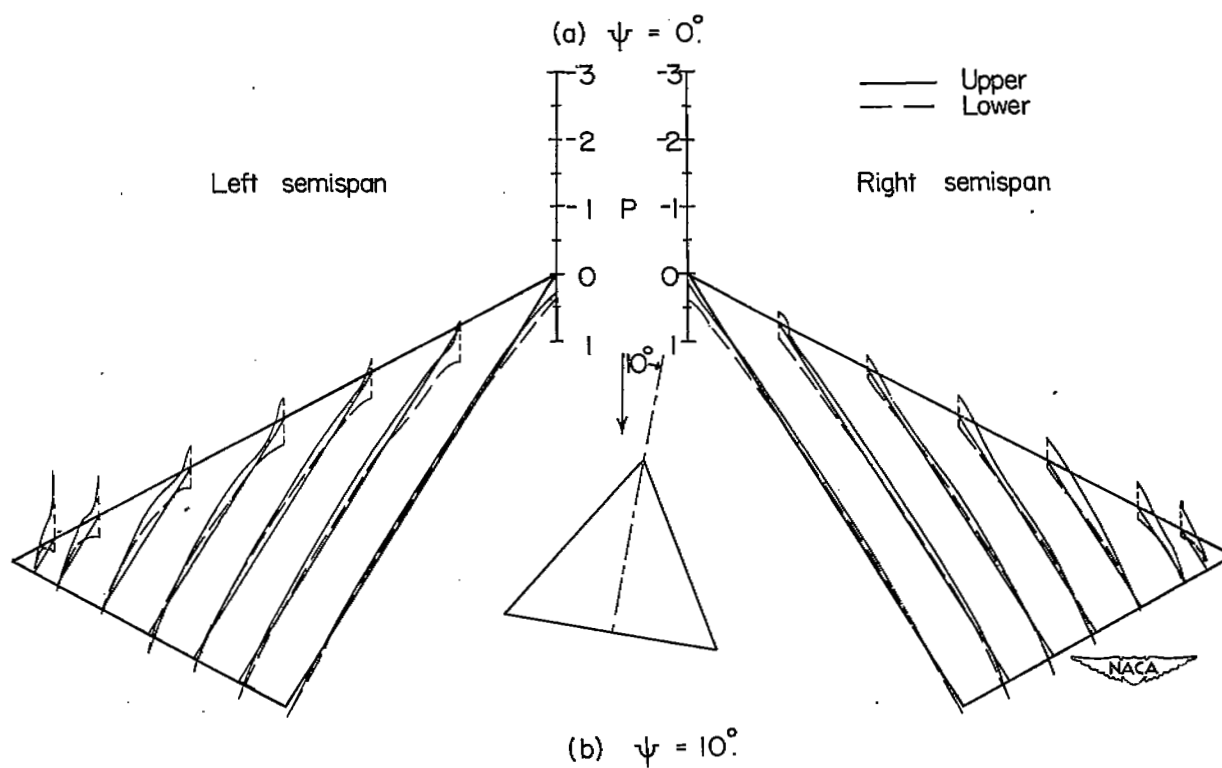
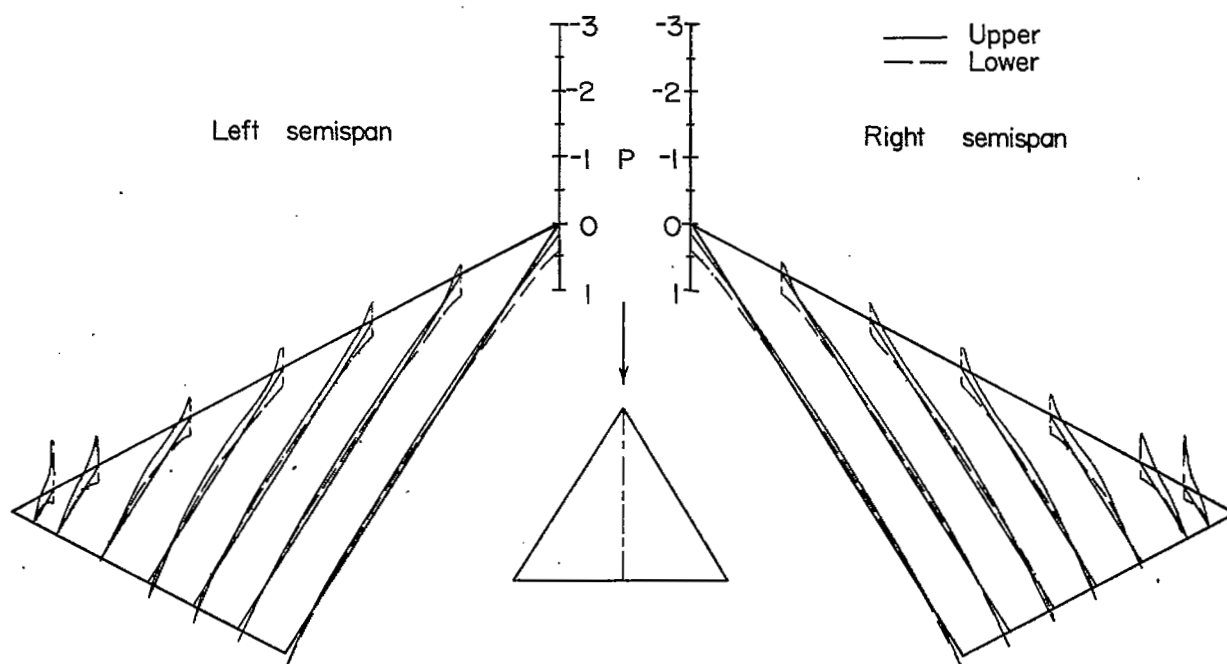


Figure 17.- Pressure distribution about wing 2 at various angles of yaw;  
 $\alpha = 4.1^\circ$ .

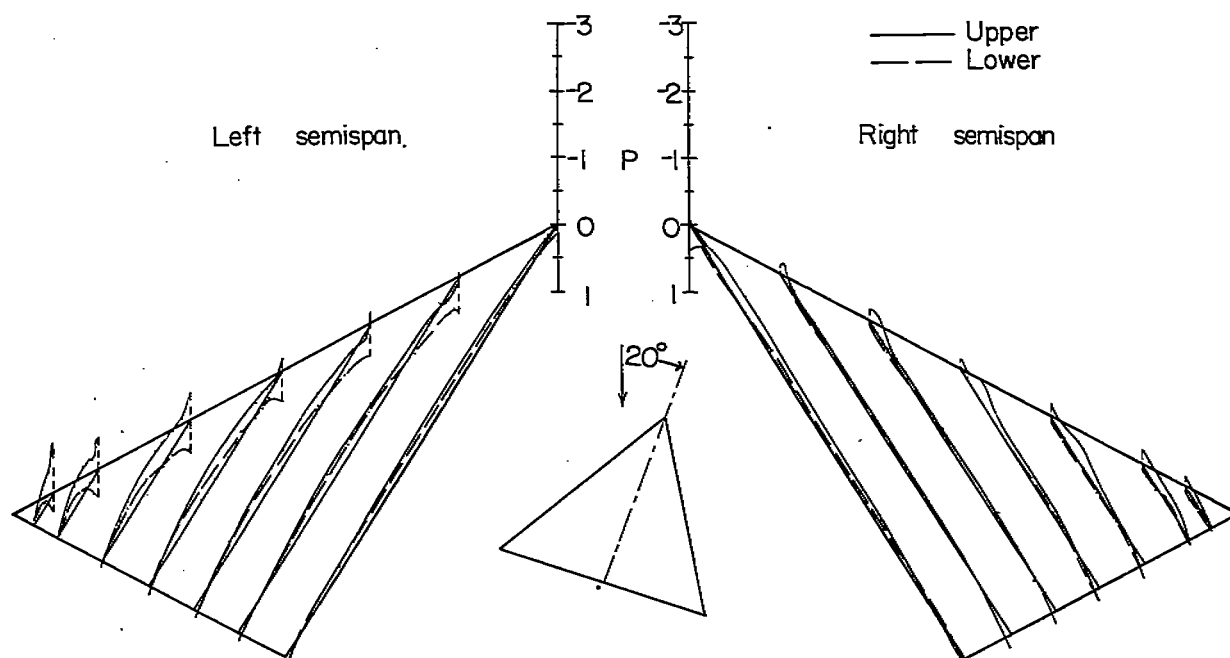
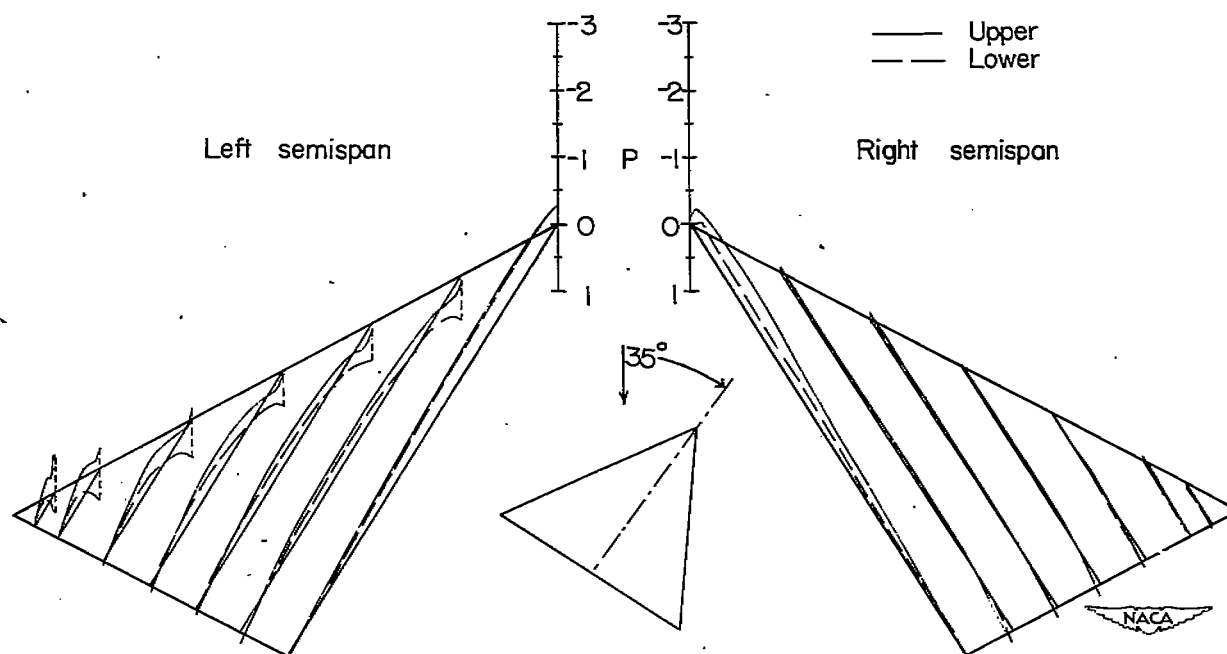
(c)  $\psi = 20^\circ$ (d)  $\psi = 35^\circ$ 

Figure 17.- Concluded.

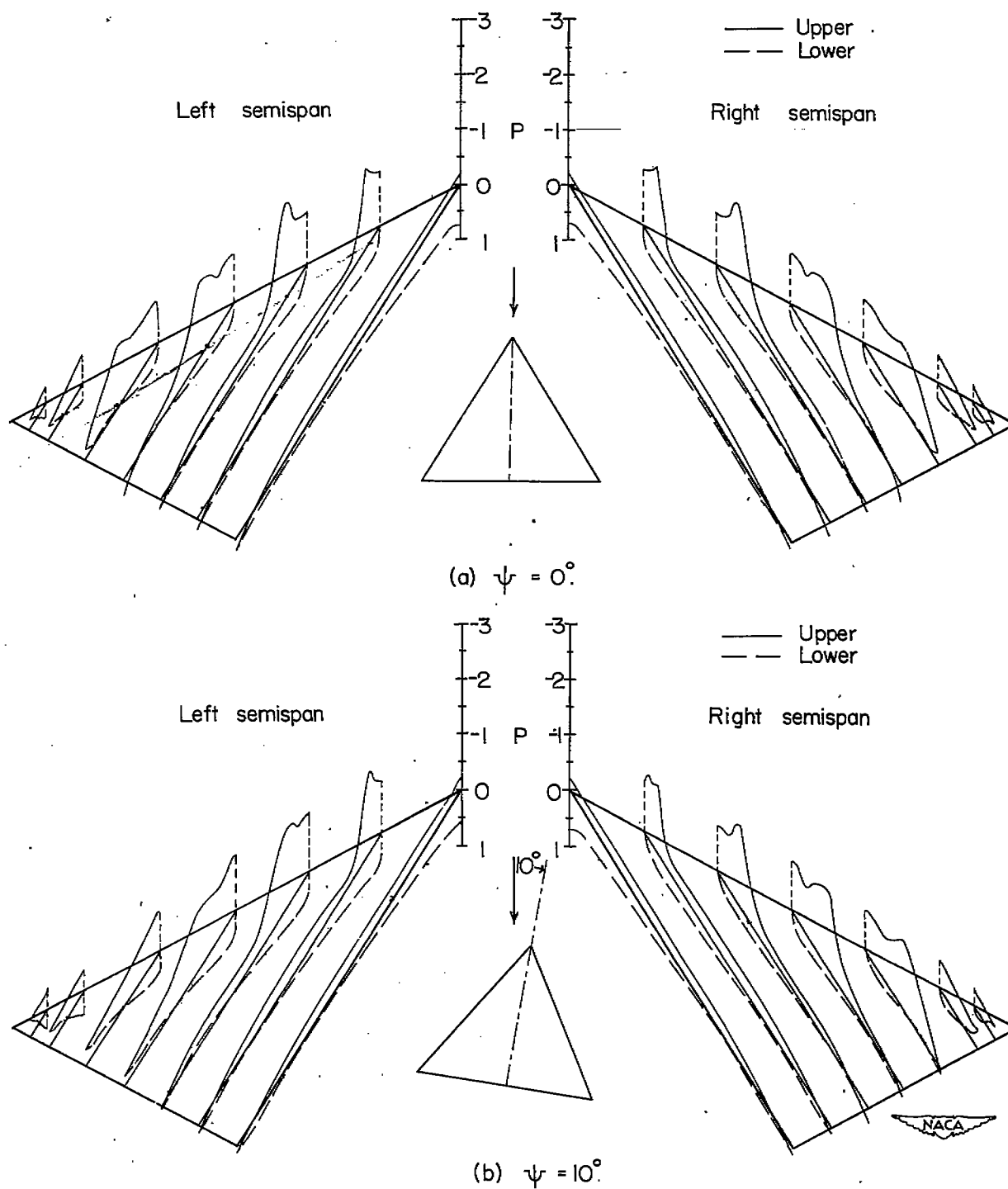


Figure 18.- Pressure distribution about wing 2 at various angles of yaw;  
 $\alpha = 14.1^\circ$ .

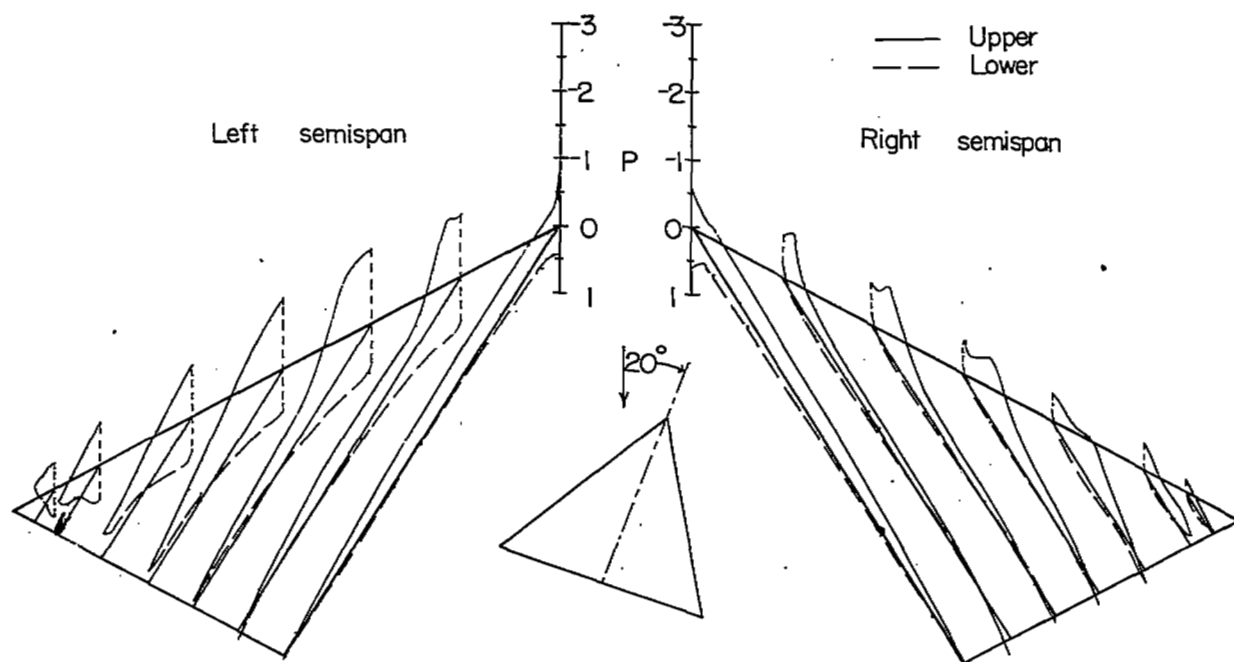
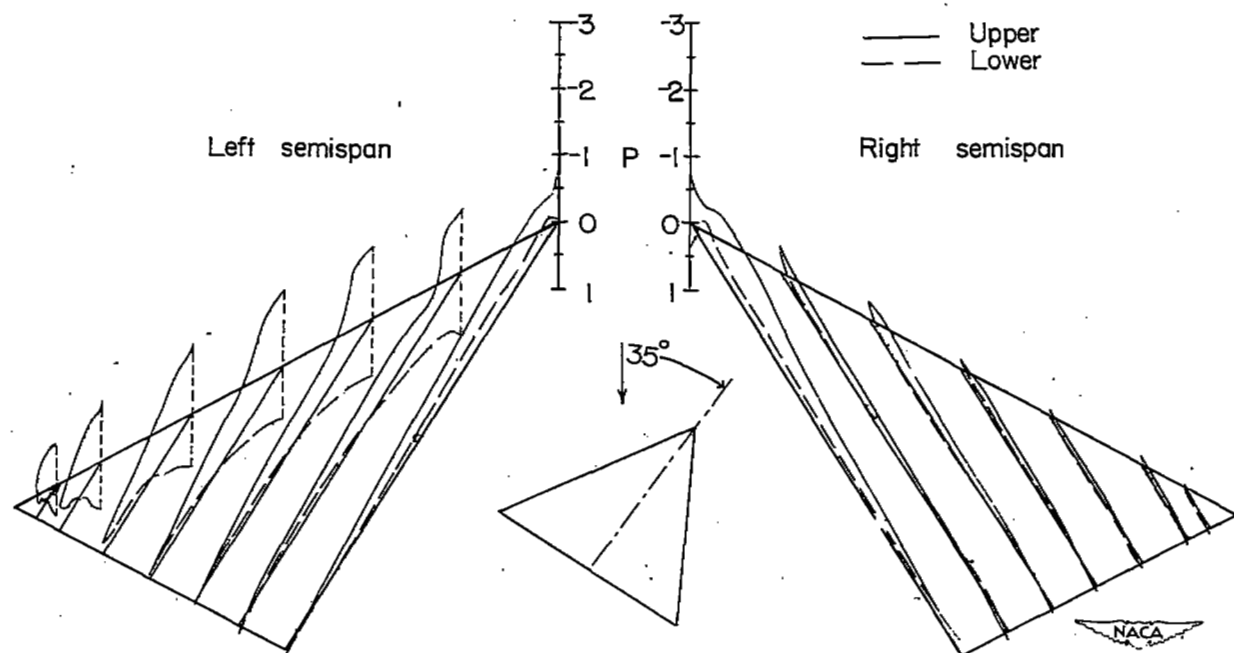
(c)  $\psi = 20^\circ$ (d)  $\psi = 35^\circ$ 

Figure 18.- Concluded.

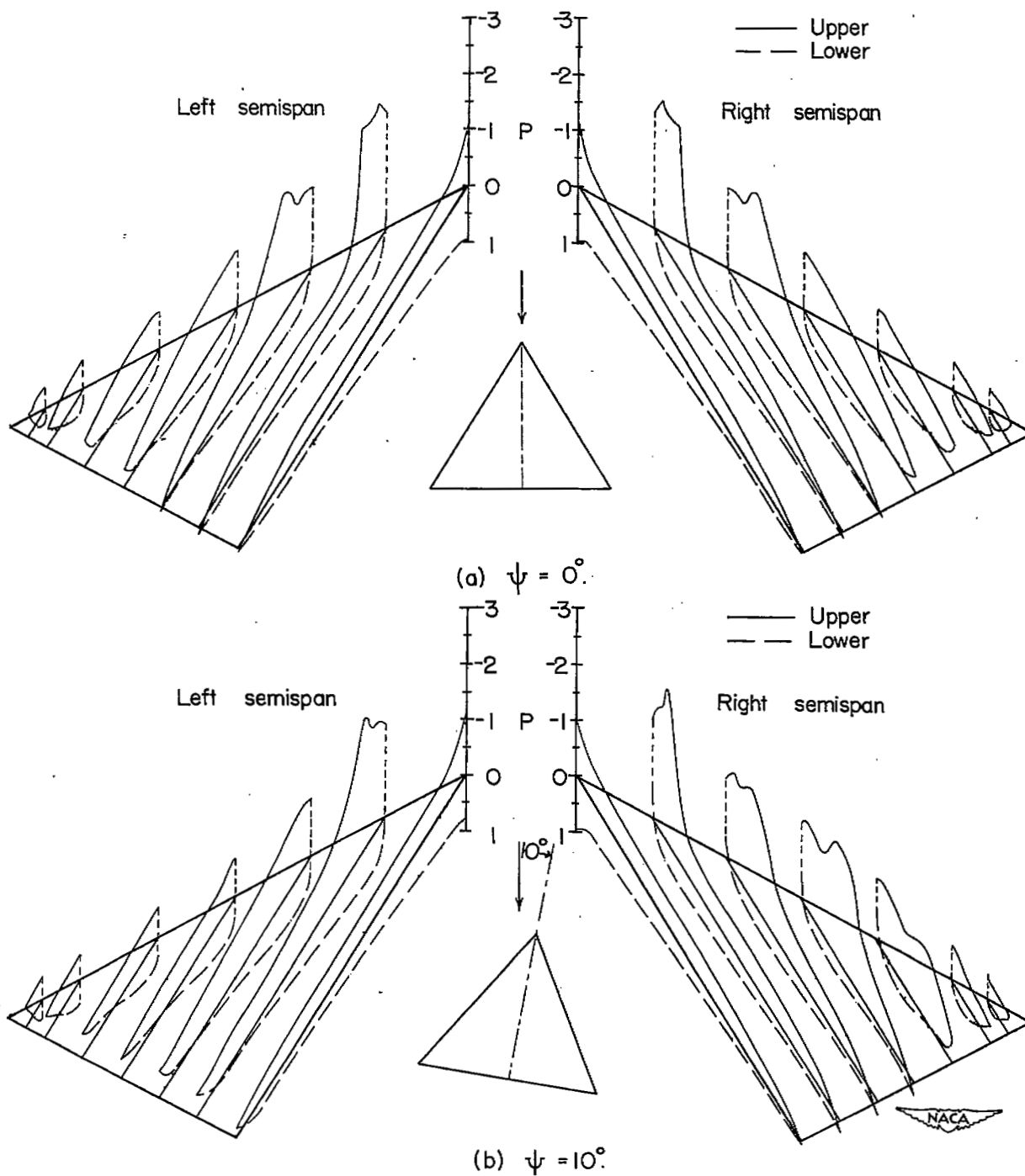


Figure 19.- Pressure distribution about wing 2 at various angles of yaw;  
 $\alpha = 24.1^\circ$ .

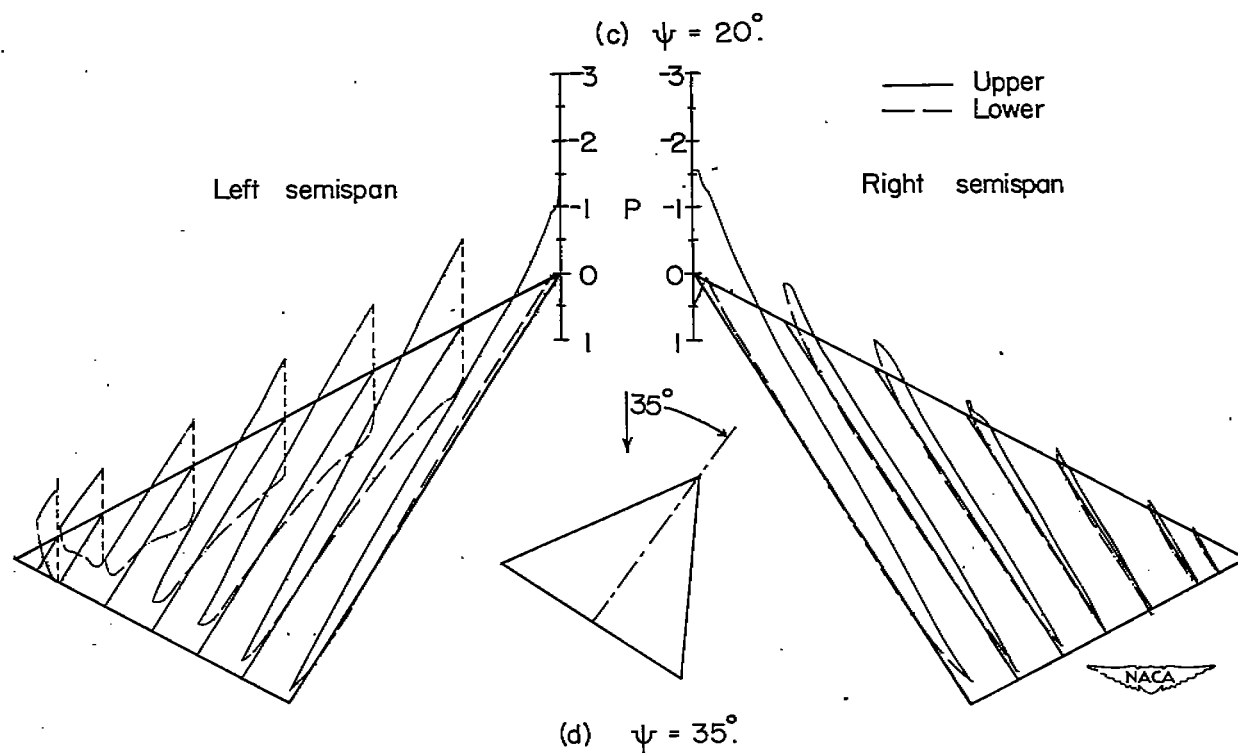
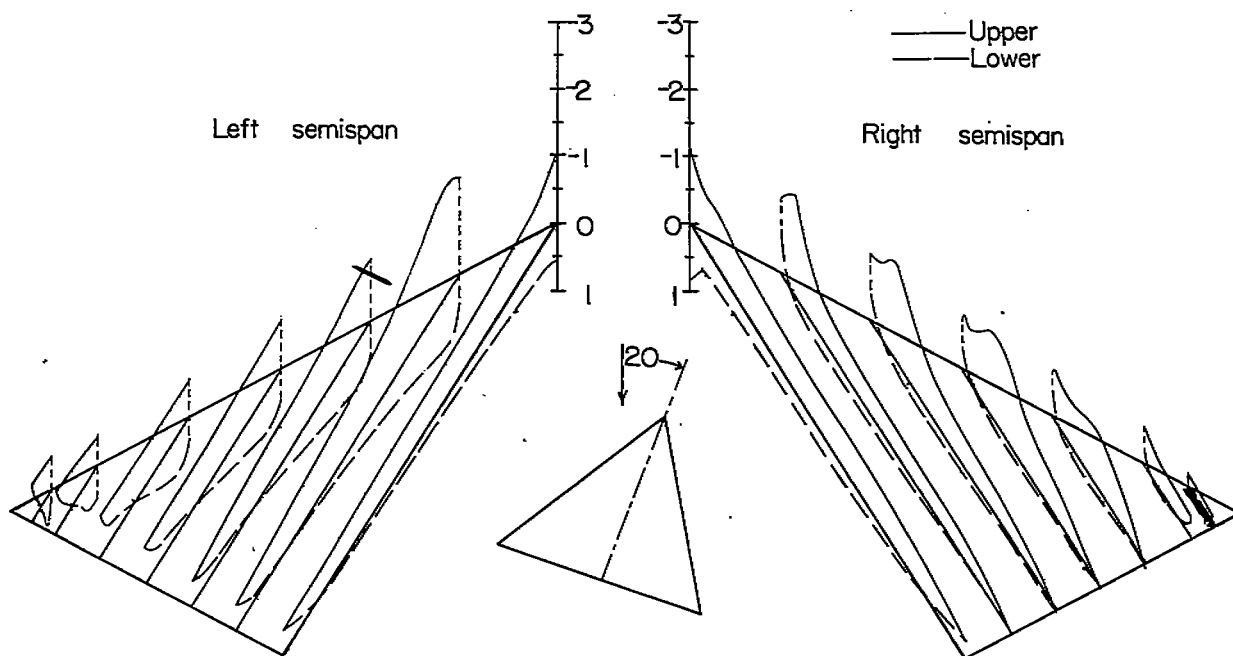


Figure 19.- Concluded.

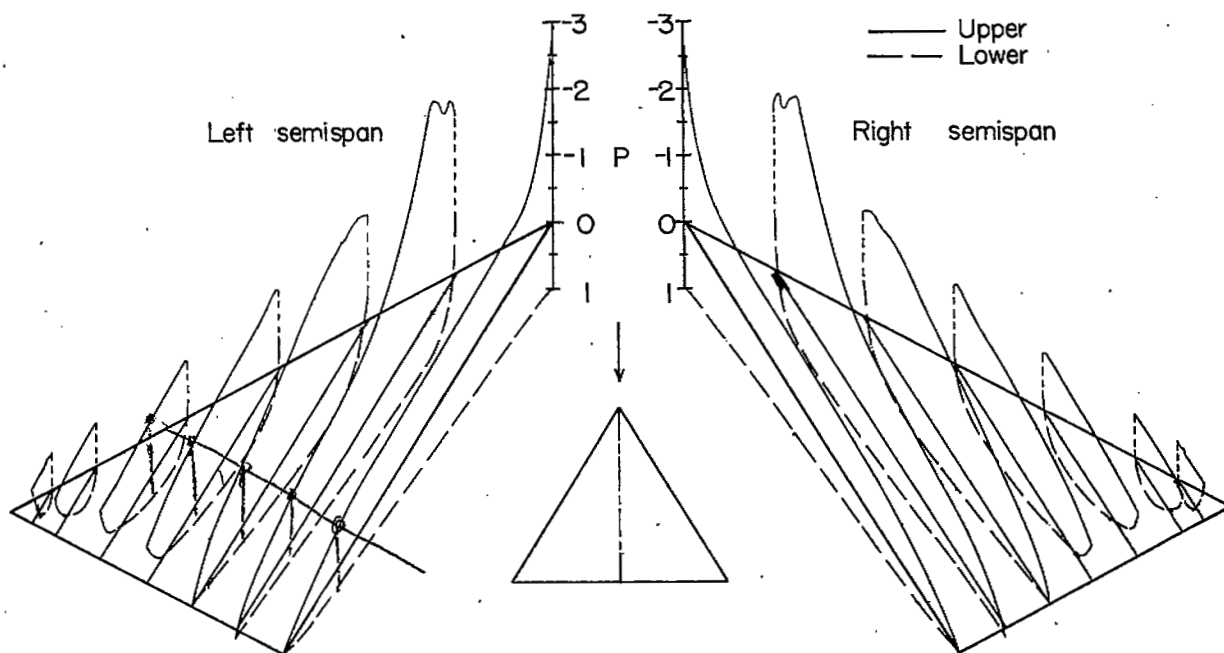
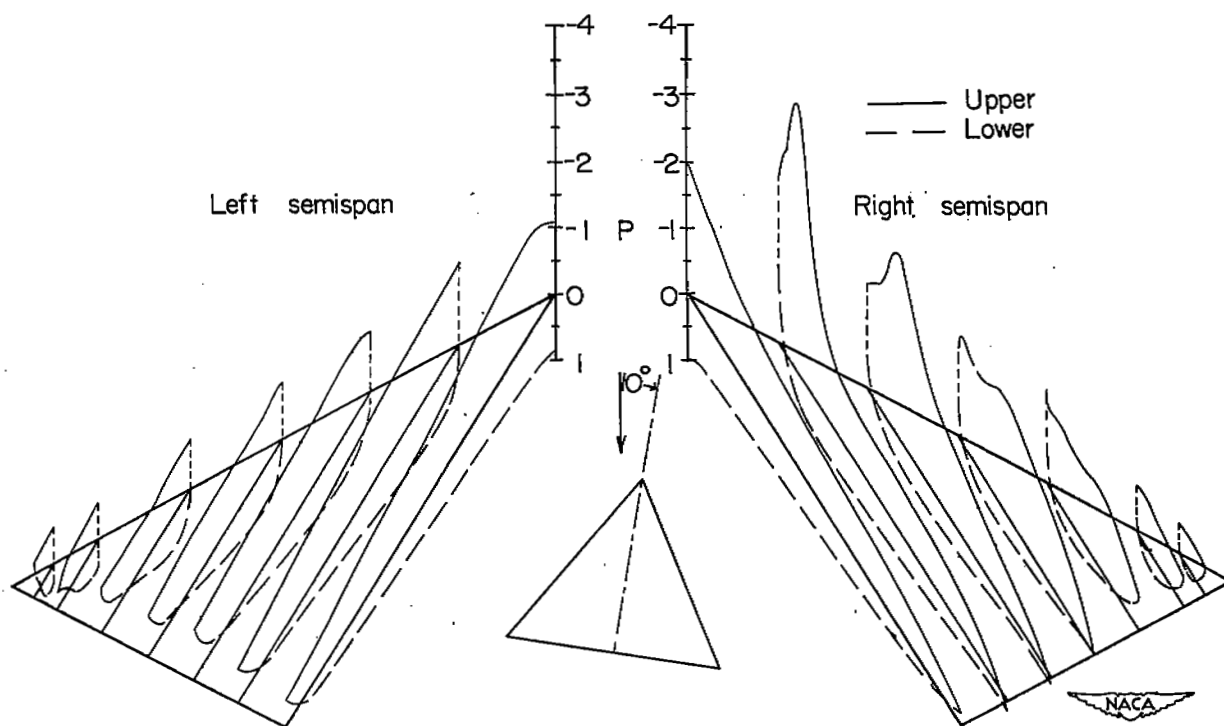
(a)  $\psi = 0^\circ$ (b)  $\psi = 10^\circ$ 

Figure 20.- Pressure distribution about wing 2 at various angles of yaw;  
 $\alpha = 34.1^\circ$ .



NACA RM L9J07

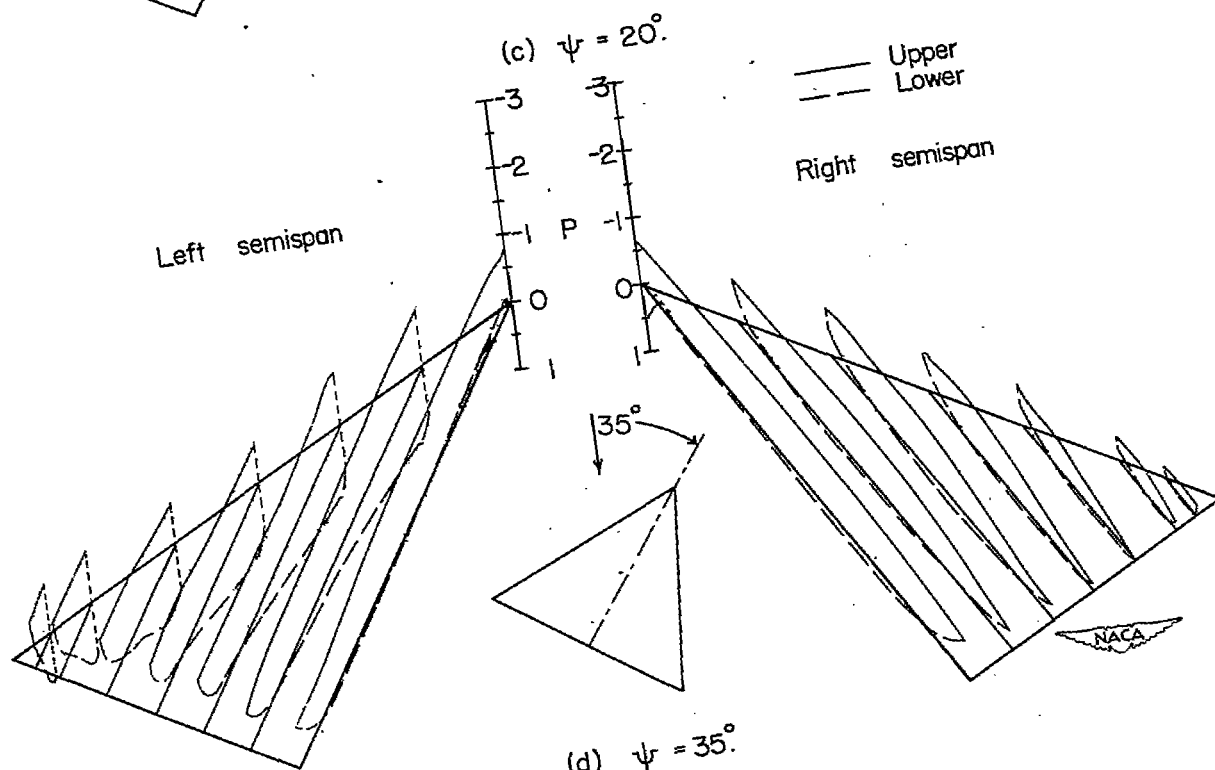
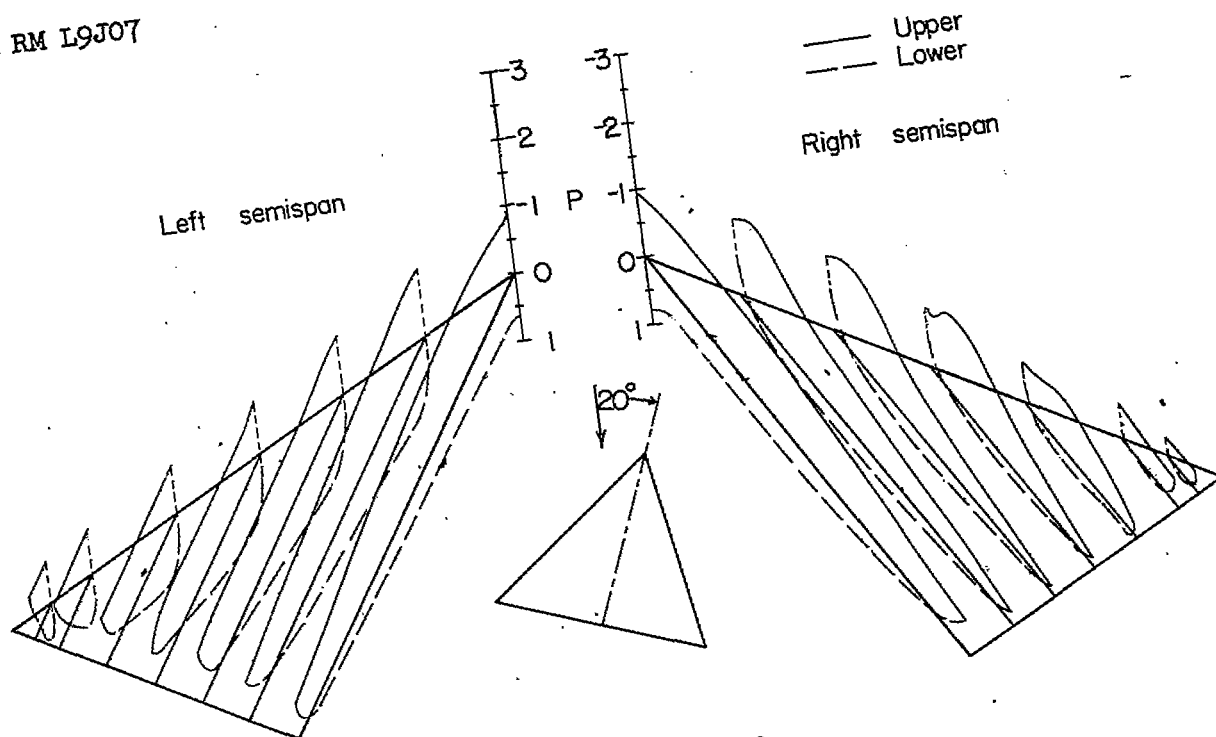


Figure 20.- Concluded.

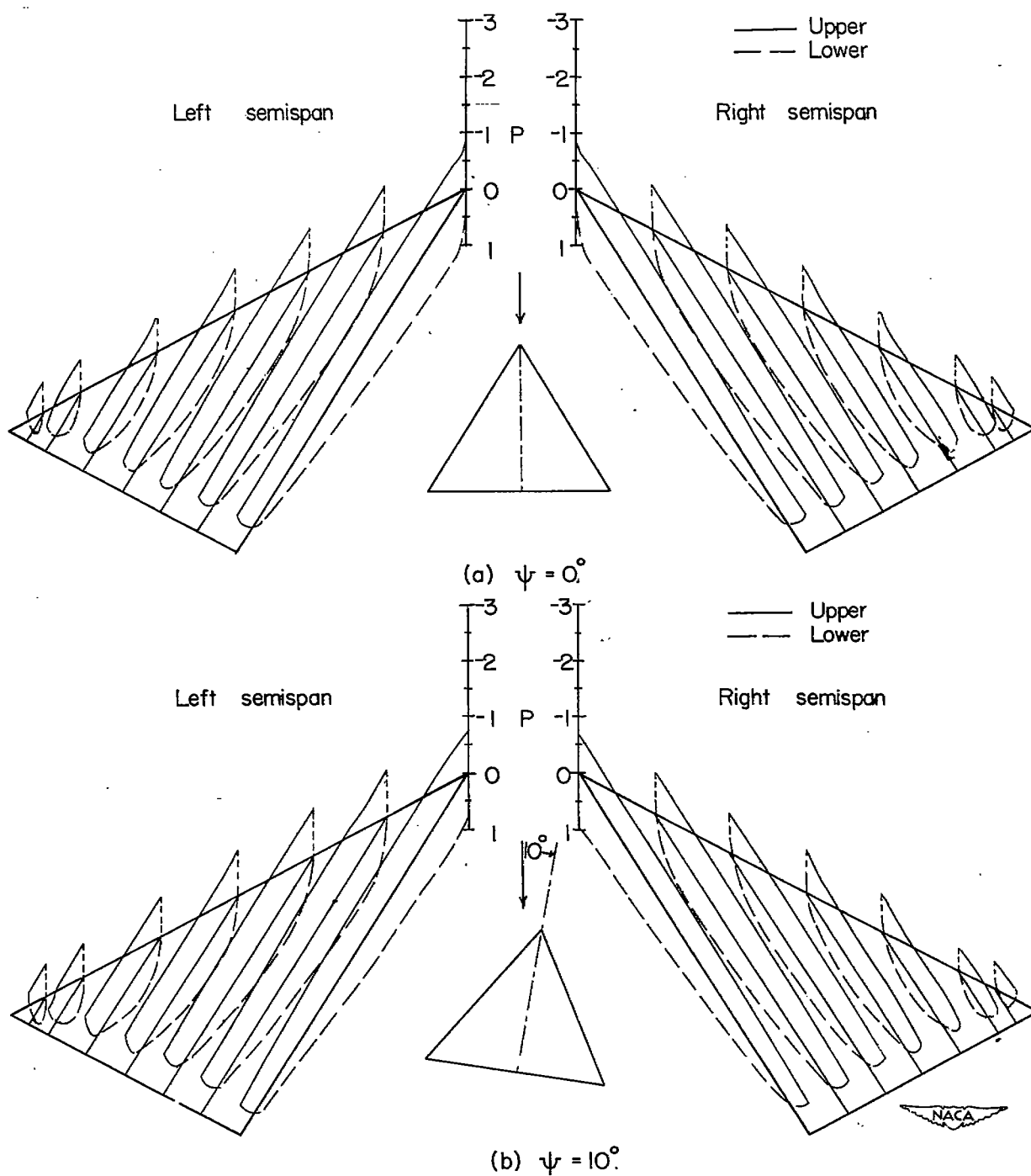


Figure 21.- Pressure distribution about wing 2 at various angles of yaw;  
 $\alpha = 44.1^\circ$ .

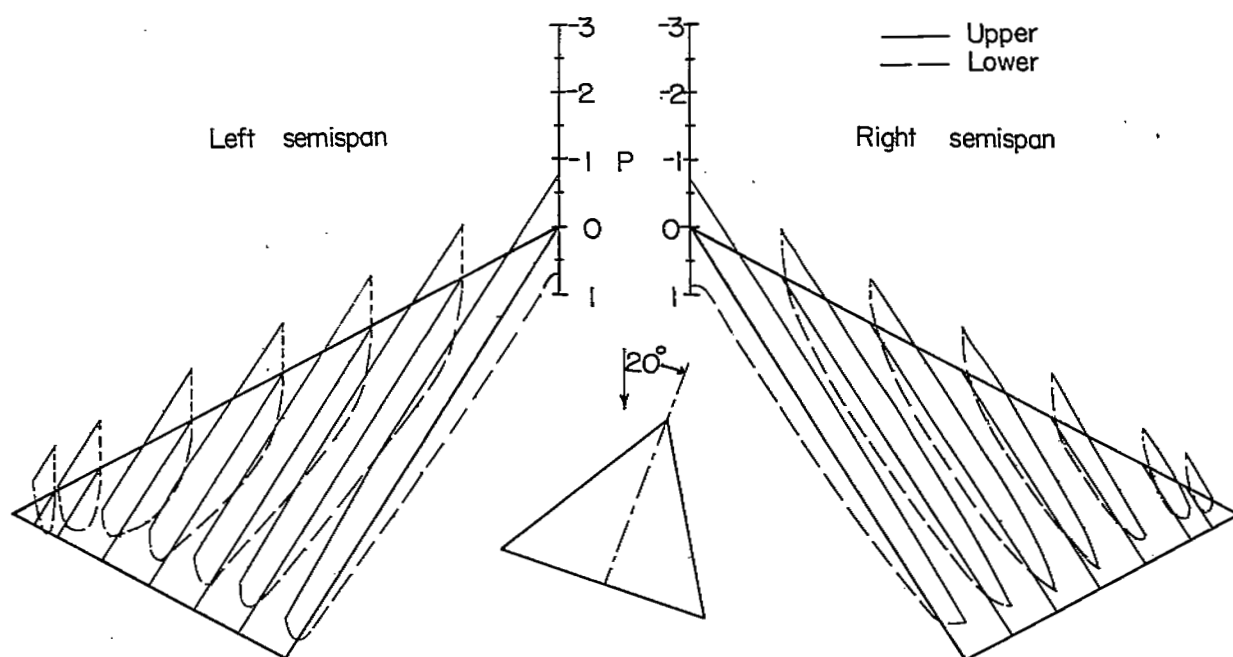
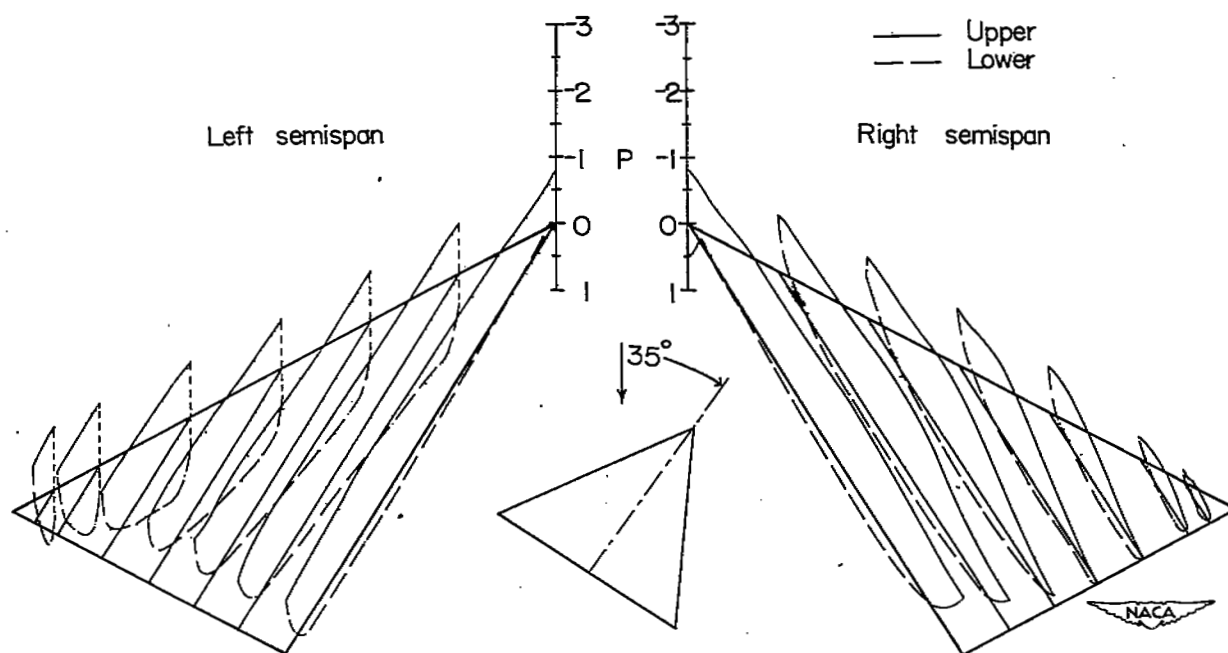
(c)  $\psi = 20^\circ$ (d)  $\psi = 35^\circ$ 

Figure 21.- Concluded.

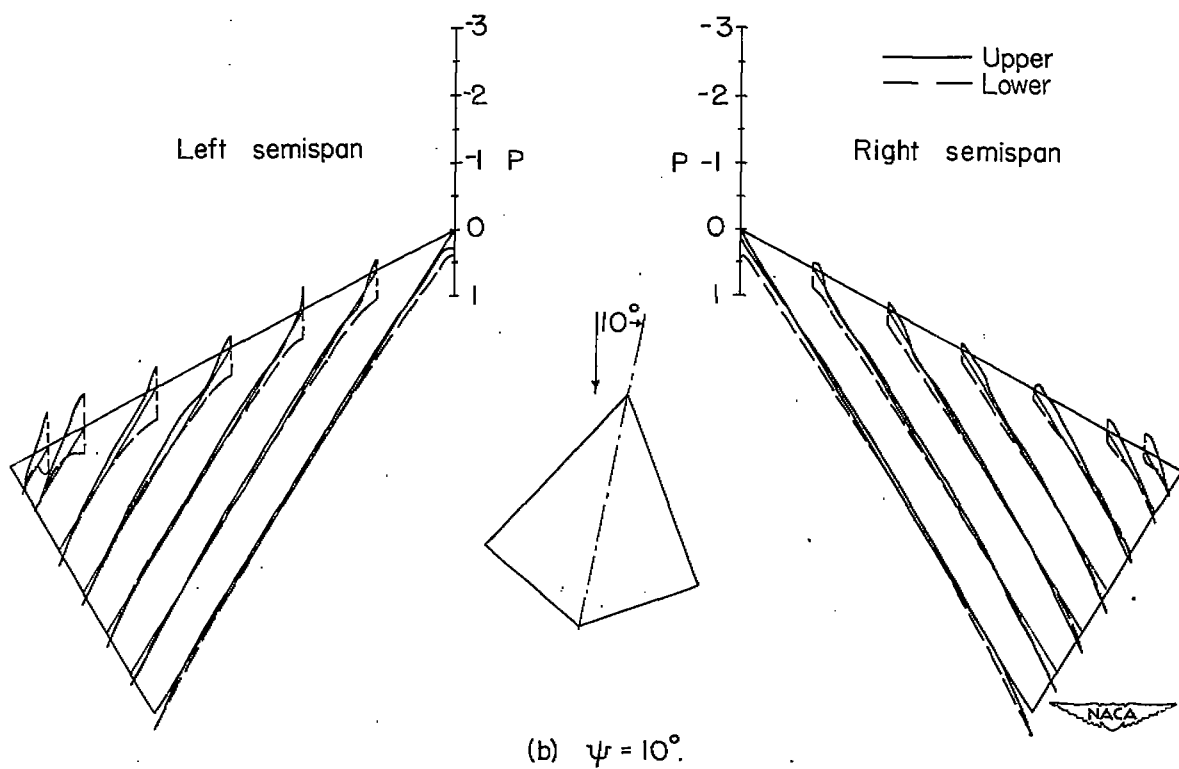
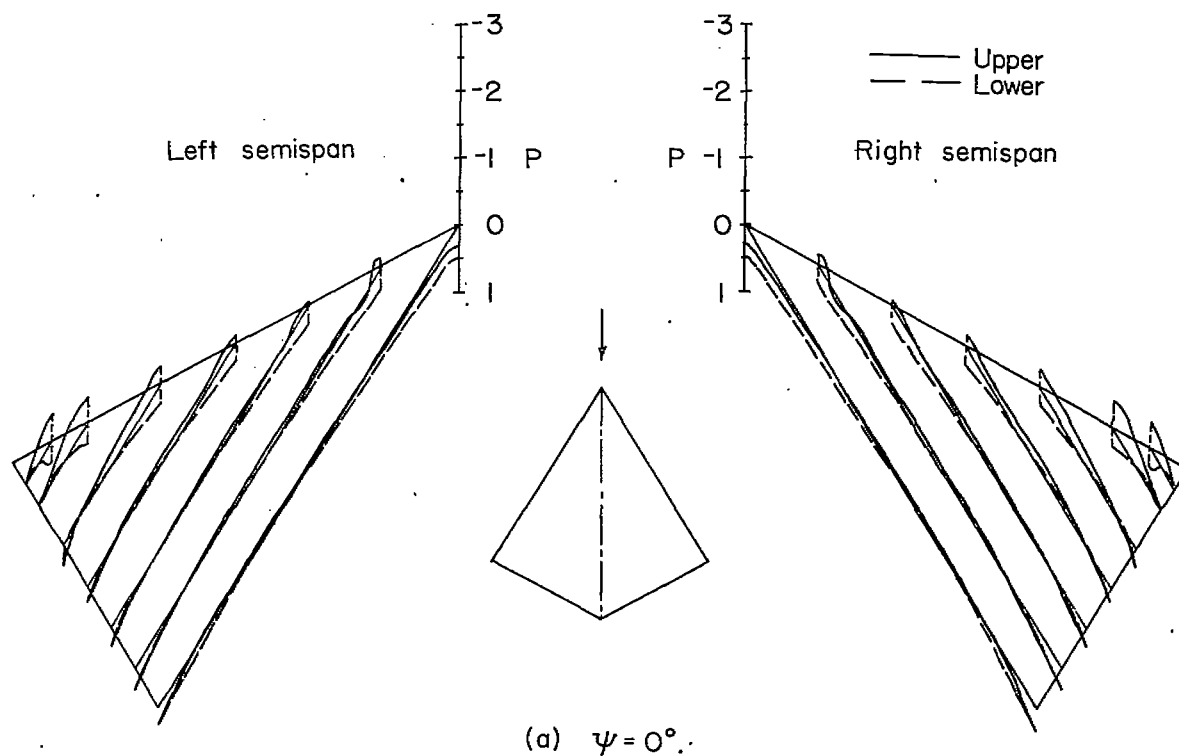


Figure 22.- Pressure distribution about wing 3. at various angles of yaw;  
 $\alpha = 4.1^\circ$ .

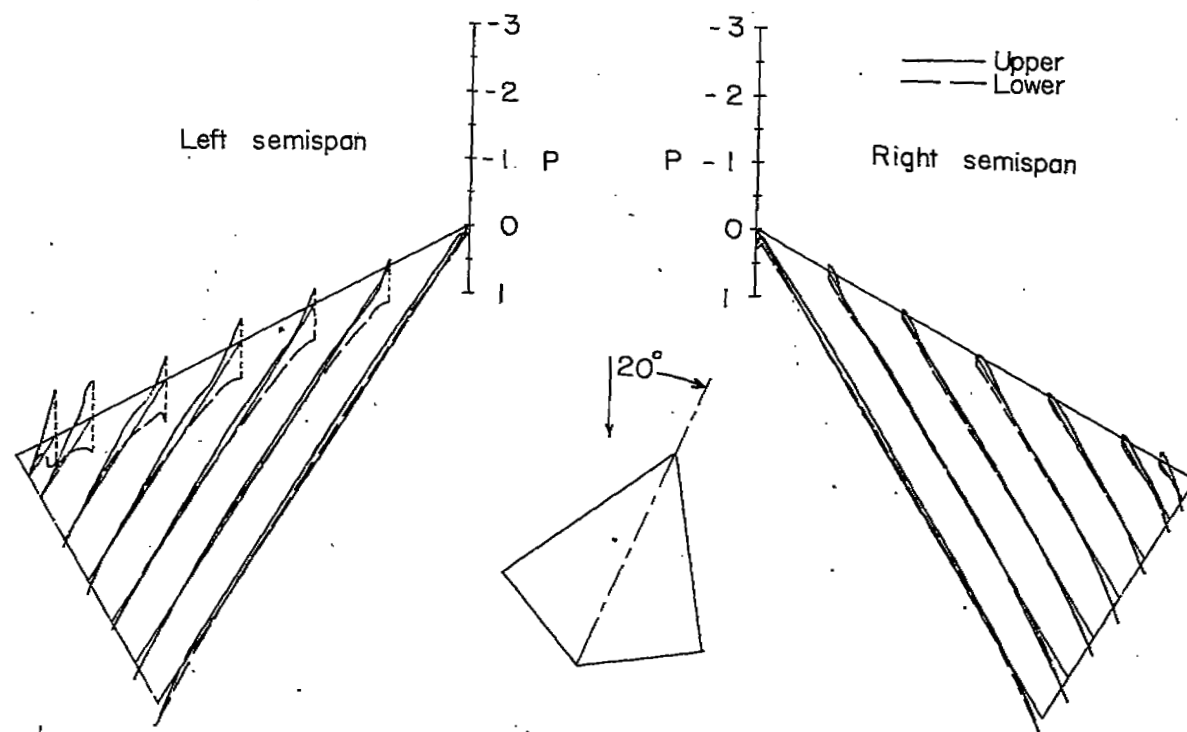
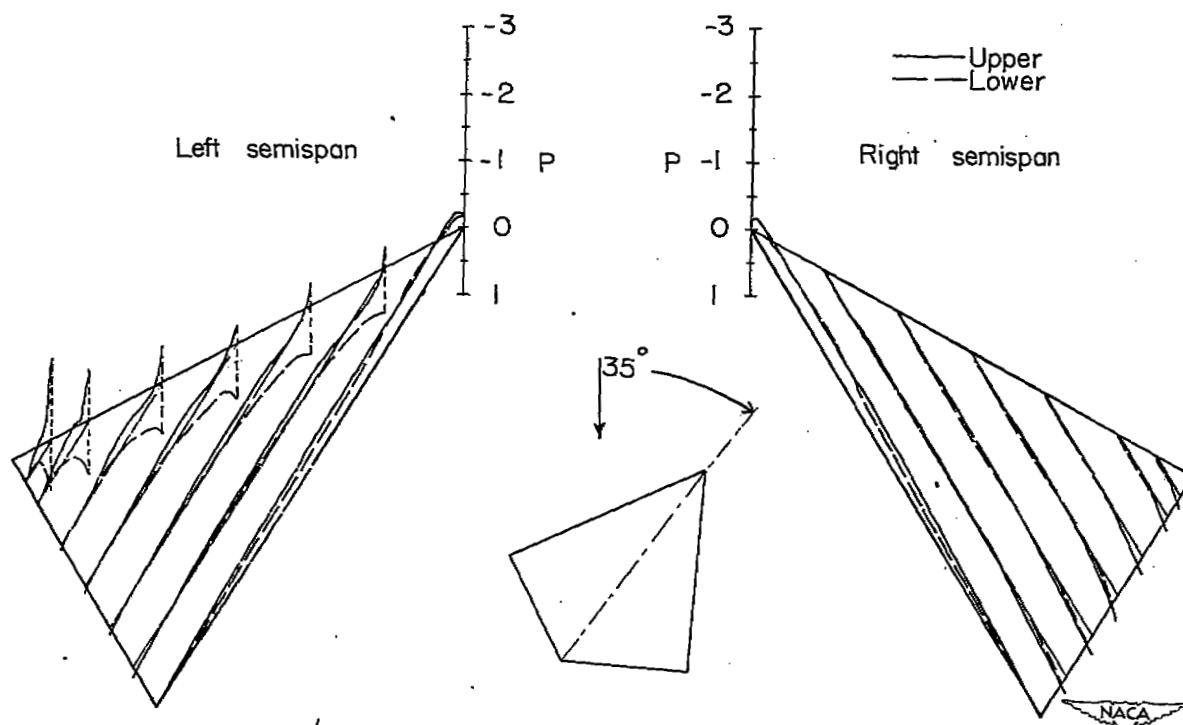
(c)  $\psi = 20^\circ$ .(d)  $\psi = 35^\circ$ .

Figure 22.- Concluded.

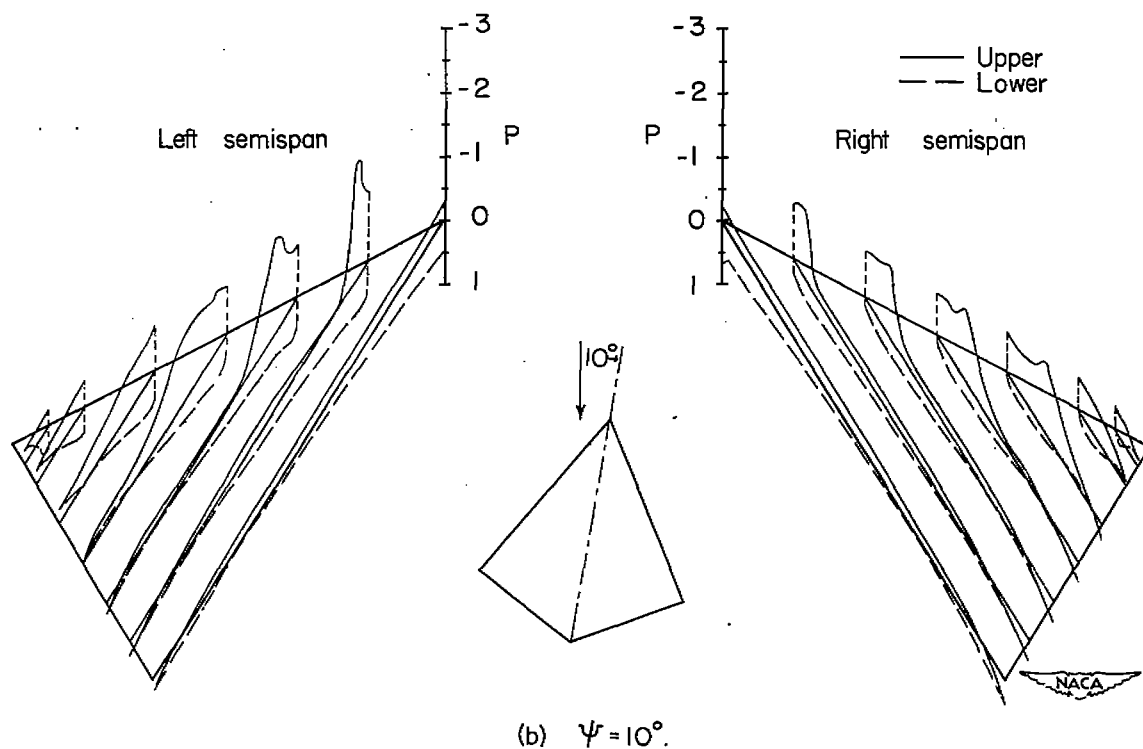
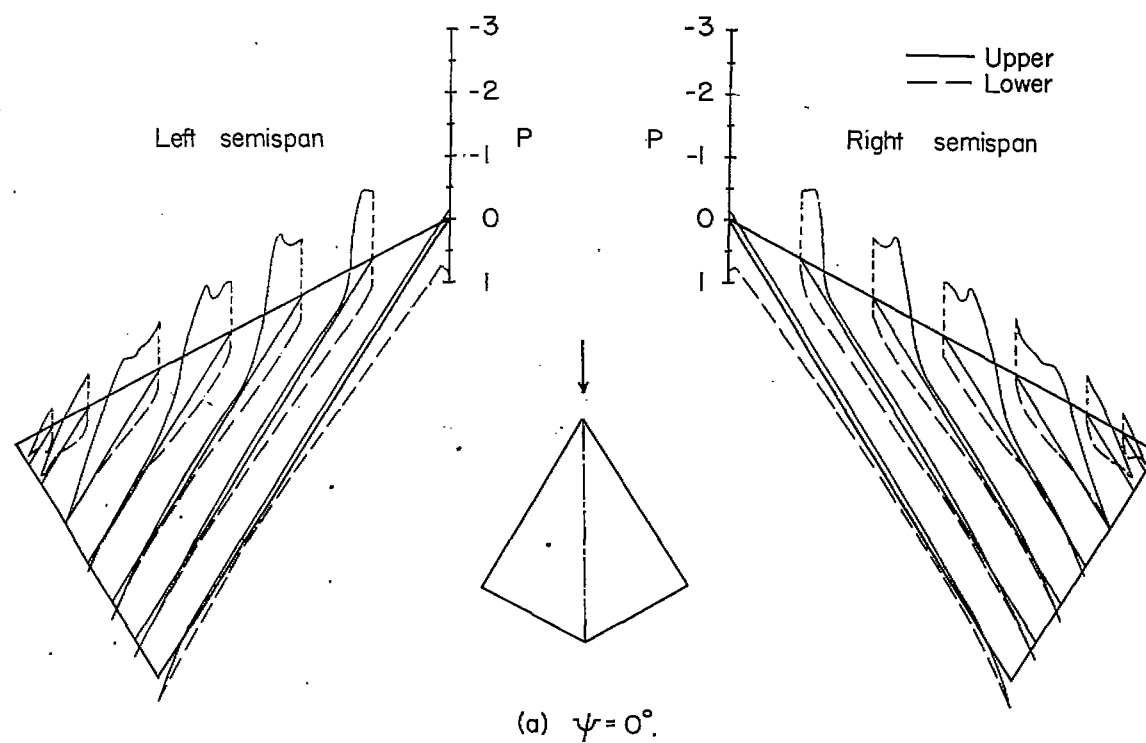


Figure 23.- Pressure distribution about wing 3 at various angles of yaw;  
 $\alpha = 14.1^\circ$ .

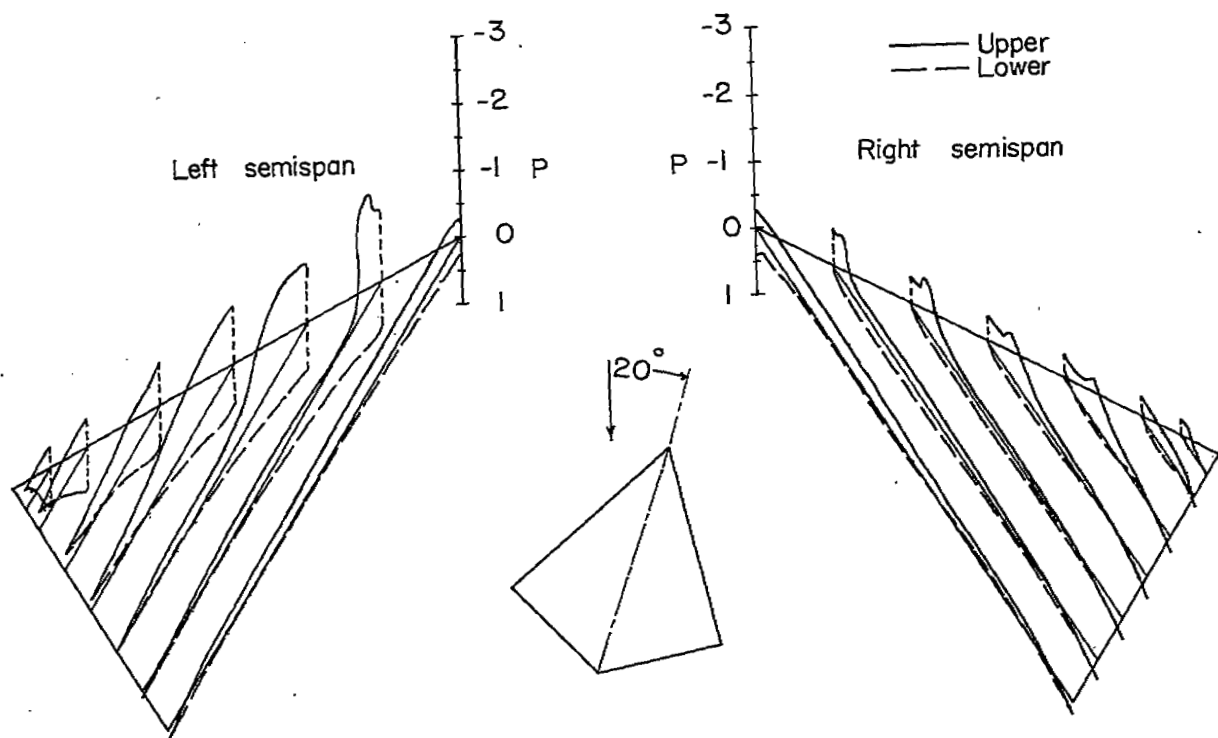
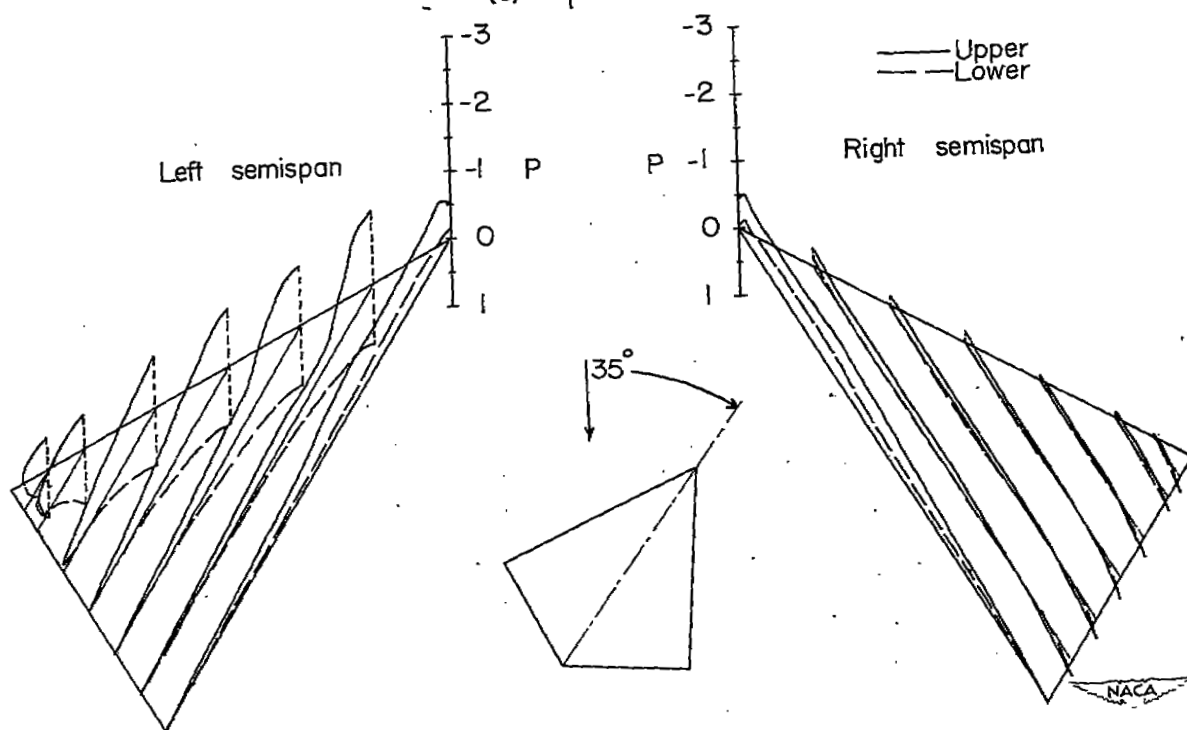
(c)  $\psi = 20^\circ$ .(d)  $\psi = 35^\circ$ .

Figure 23.- Concluded.

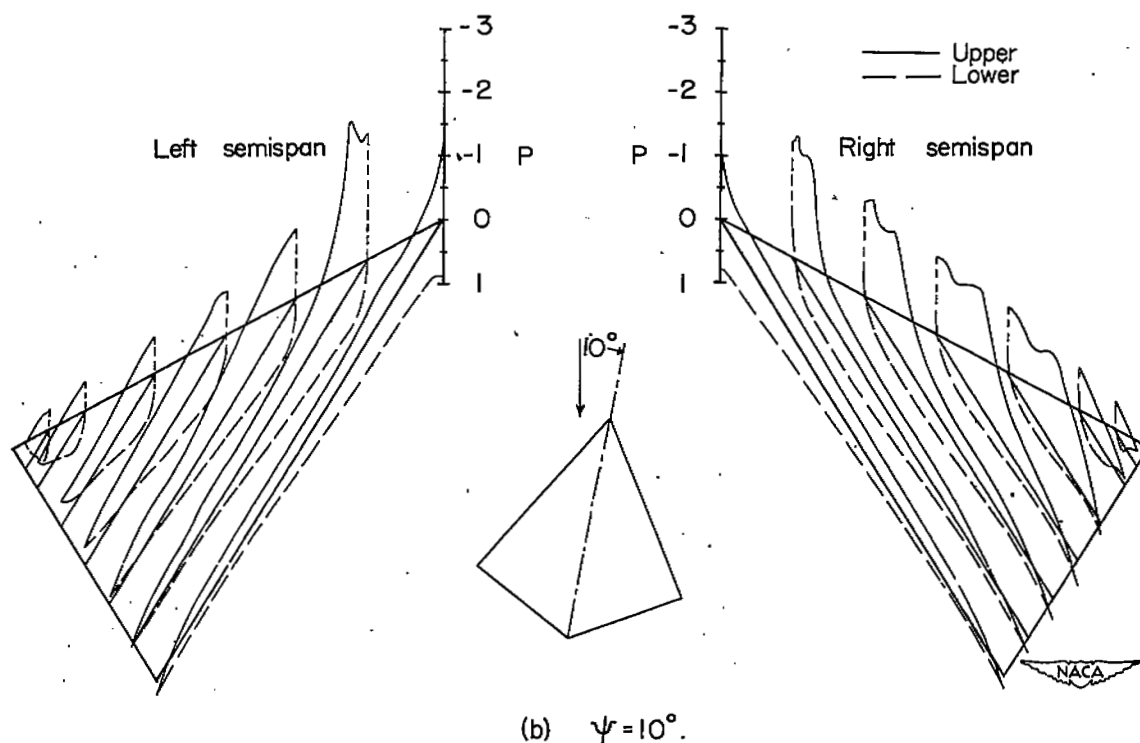
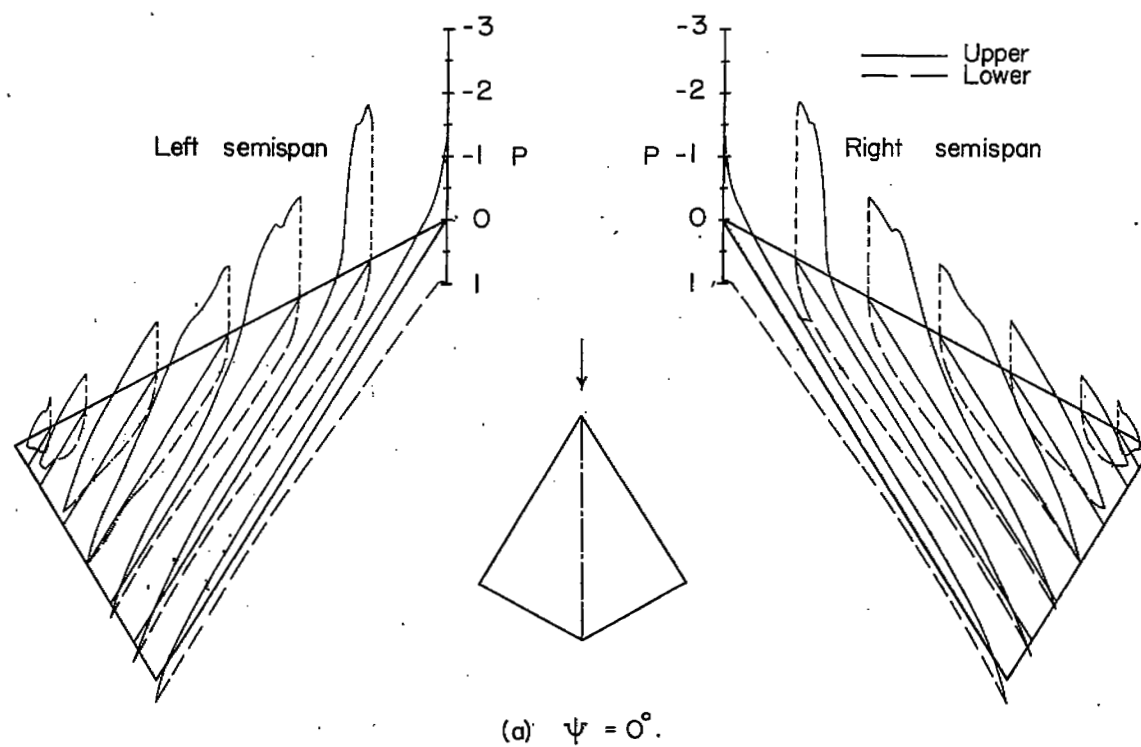


Figure 24.- Pressure distribution about wing 3 at various angles of yaw;  
 $\alpha = 24.1^\circ$ .



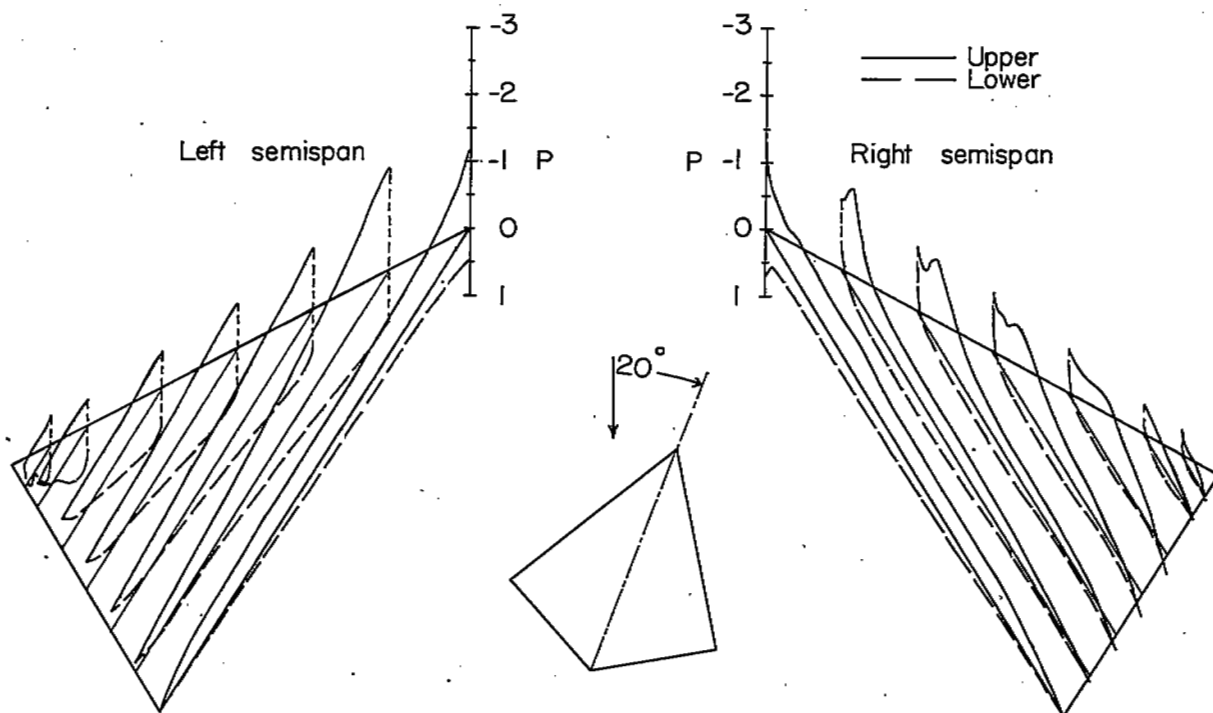
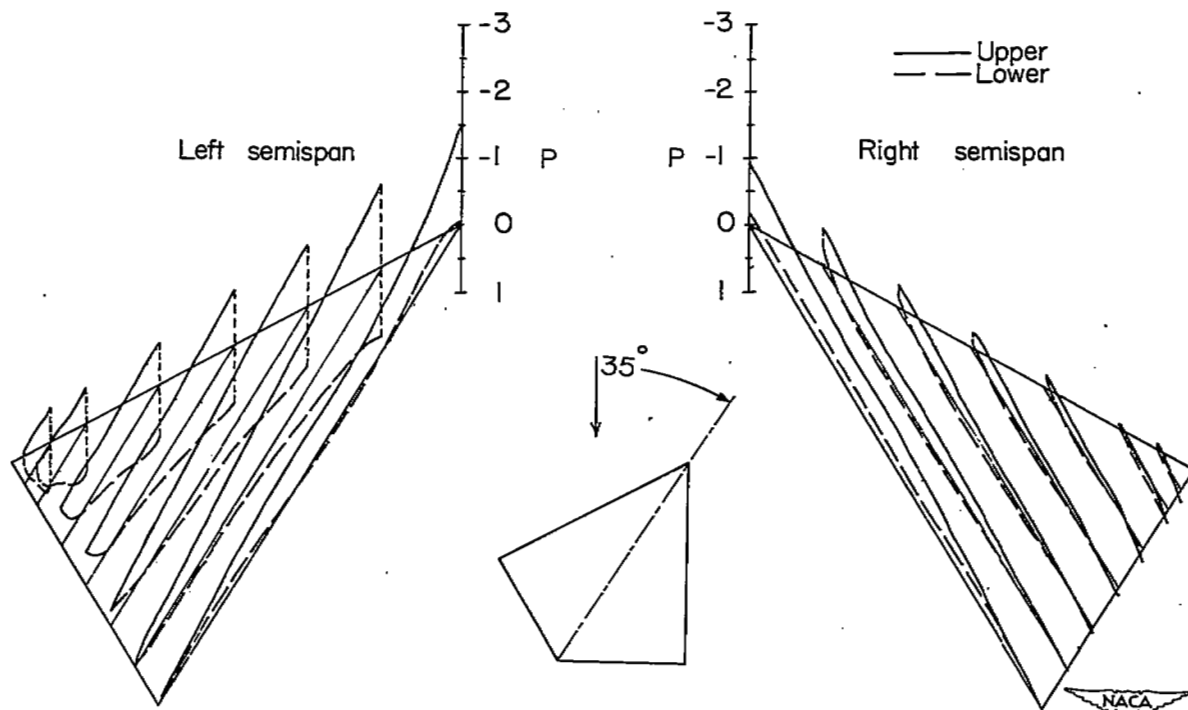
(c)  $\psi = 20^\circ$ .(d)  $\psi = 35^\circ$ .

Figure 24.- Concluded.

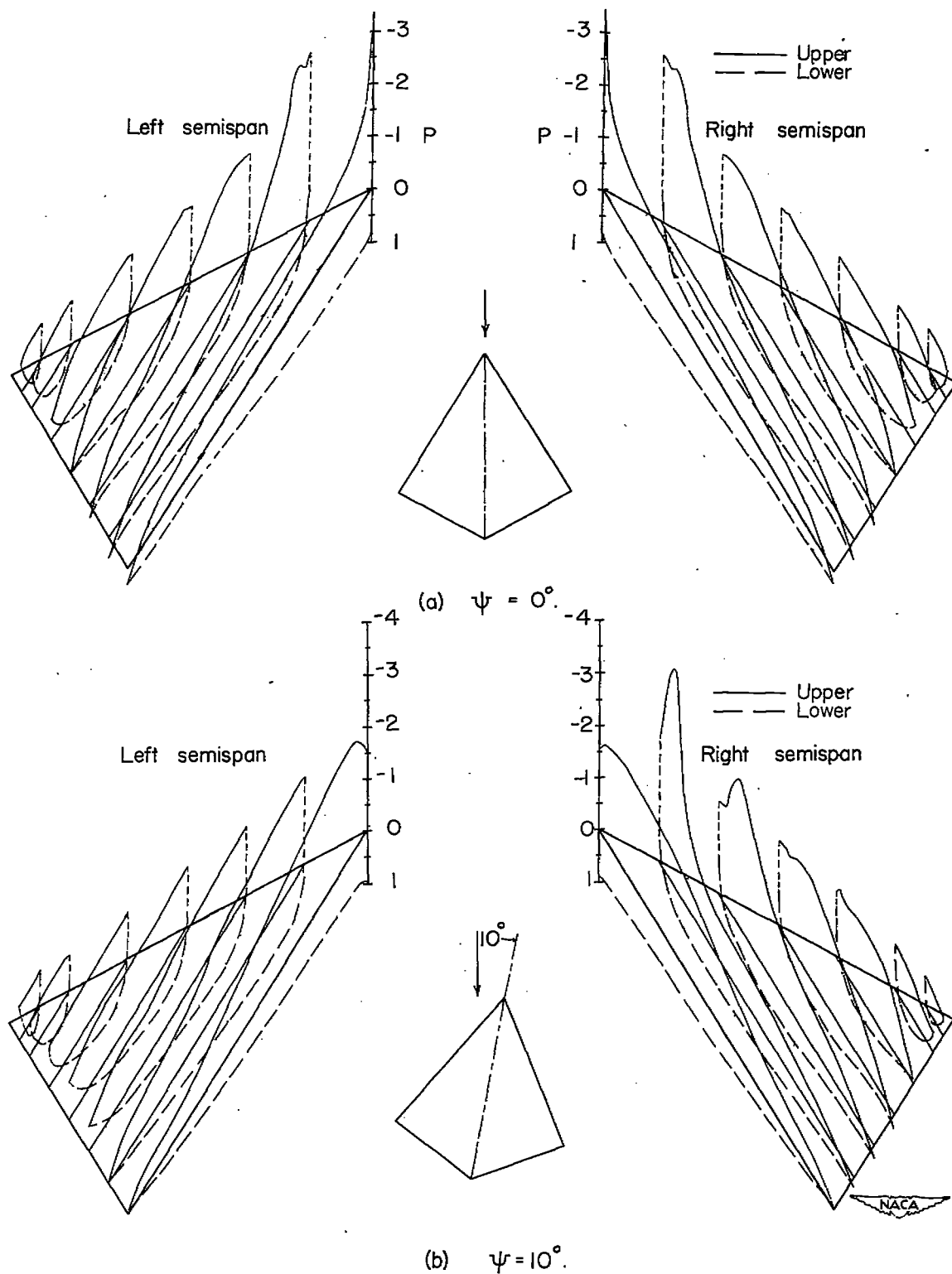


Figure 25.- Pressure distribution about wing 3 at various angles of yaw;  
 $\alpha = 39.1^\circ$ .

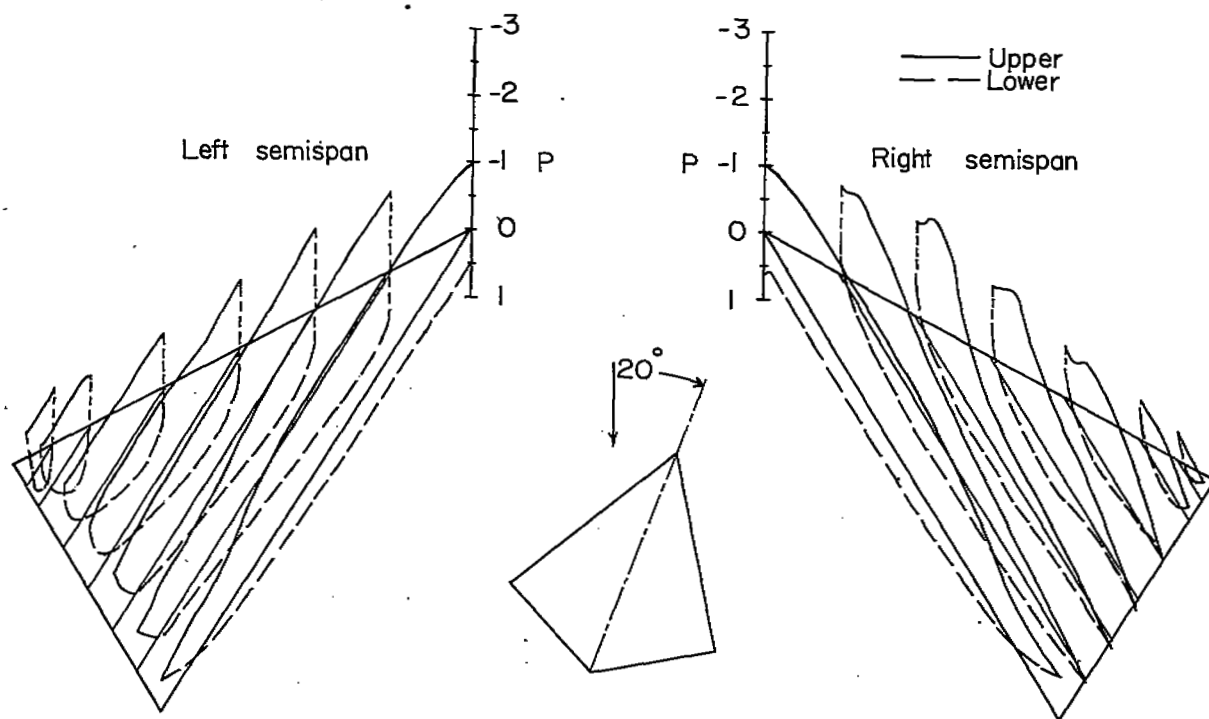
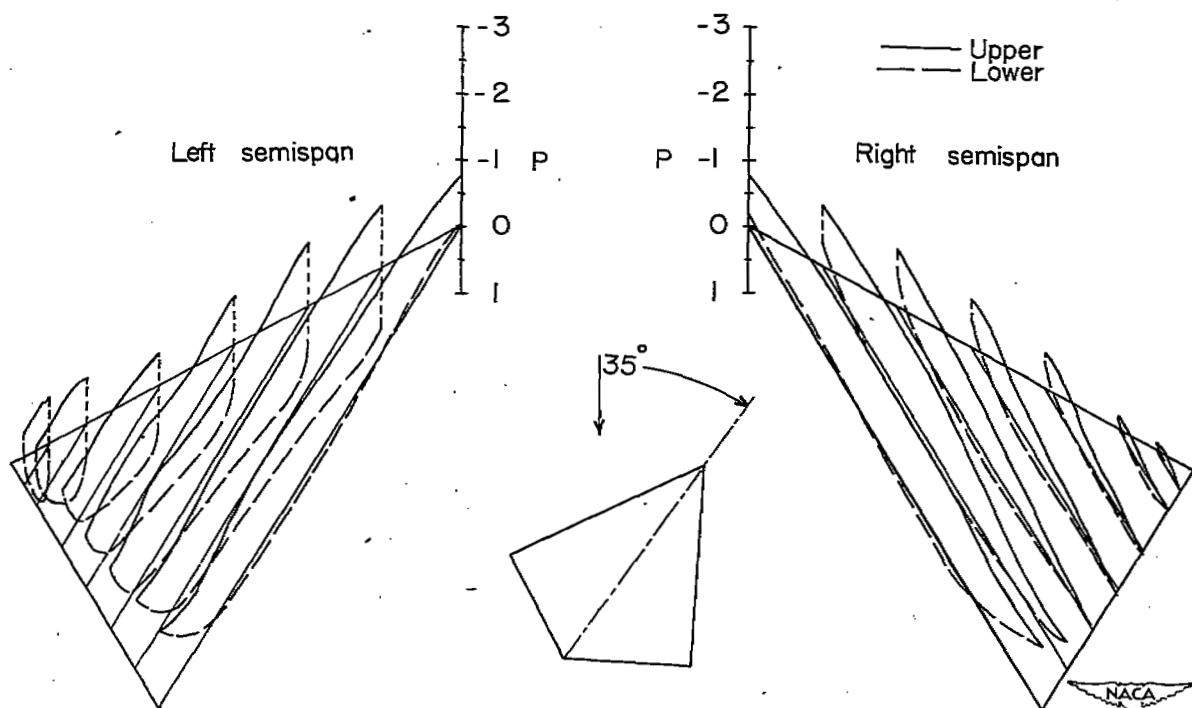
(c)  $\psi = 20^\circ$ .(d)  $\psi = 35^\circ$ .

Figure 25.- Concluded.

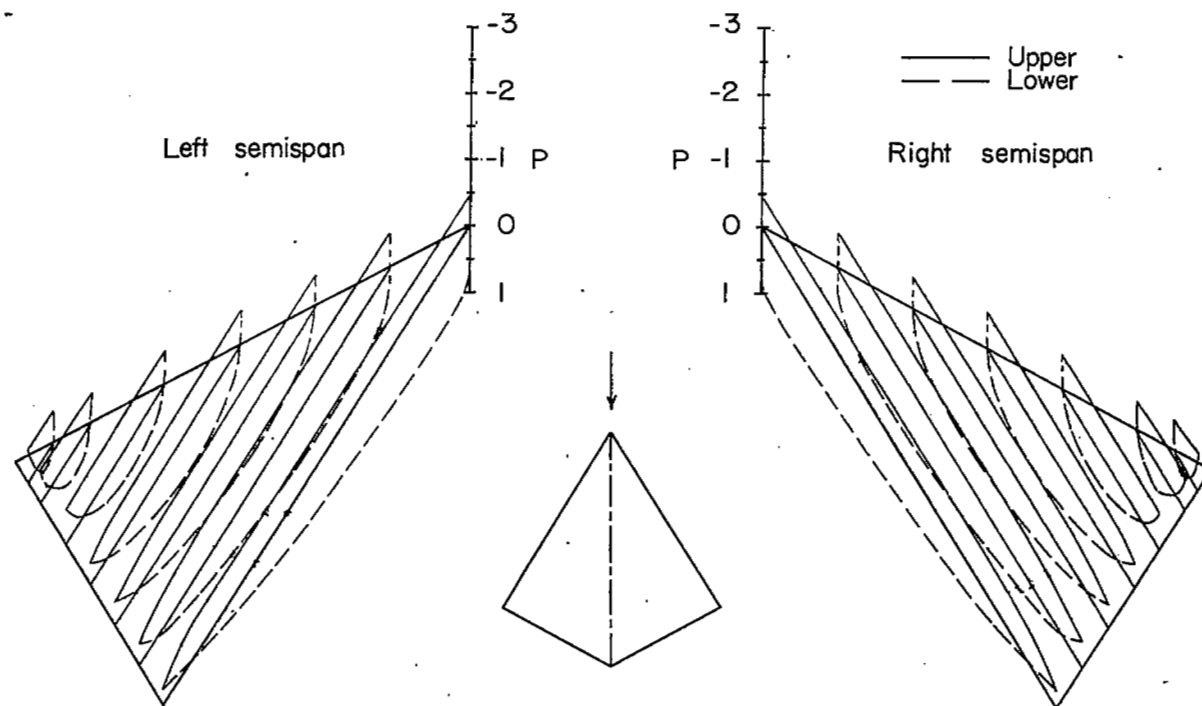
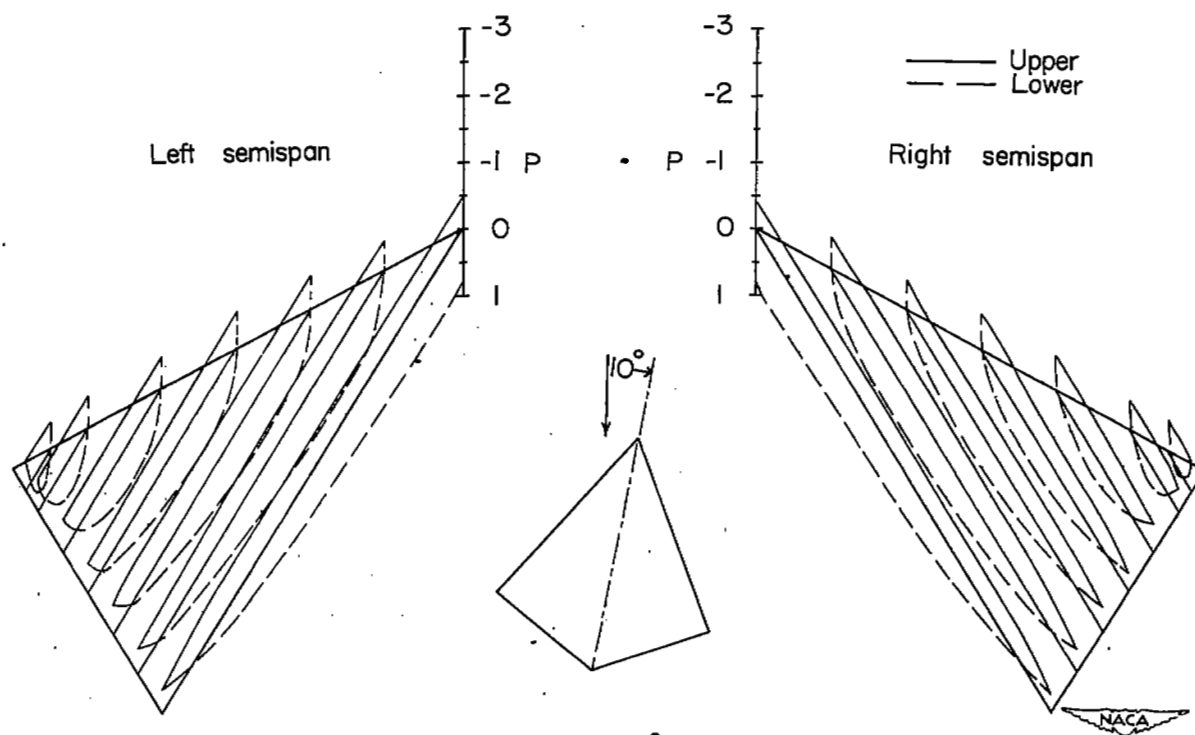
(a)  $\psi = 0^\circ$ .(b)  $\psi = 10^\circ$ .

Figure 26.- Pressure distribution about wing 3 at various angles of yaw;  
 $\alpha = 50.1^\circ$ .

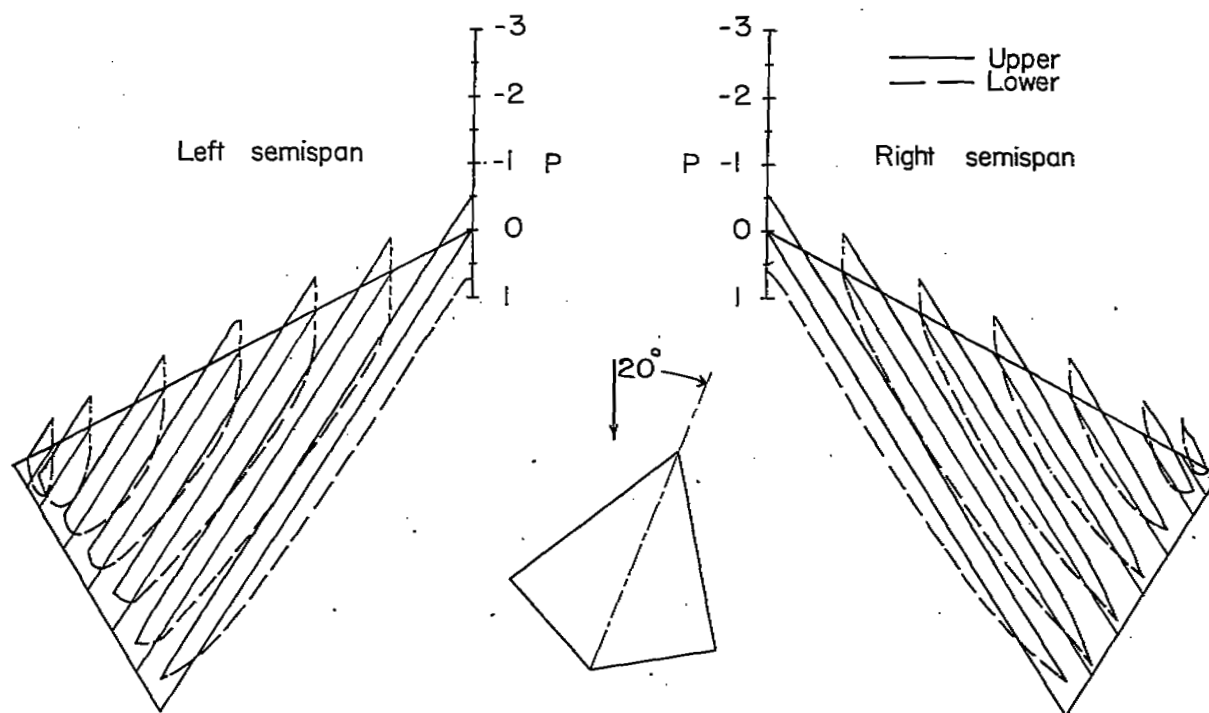
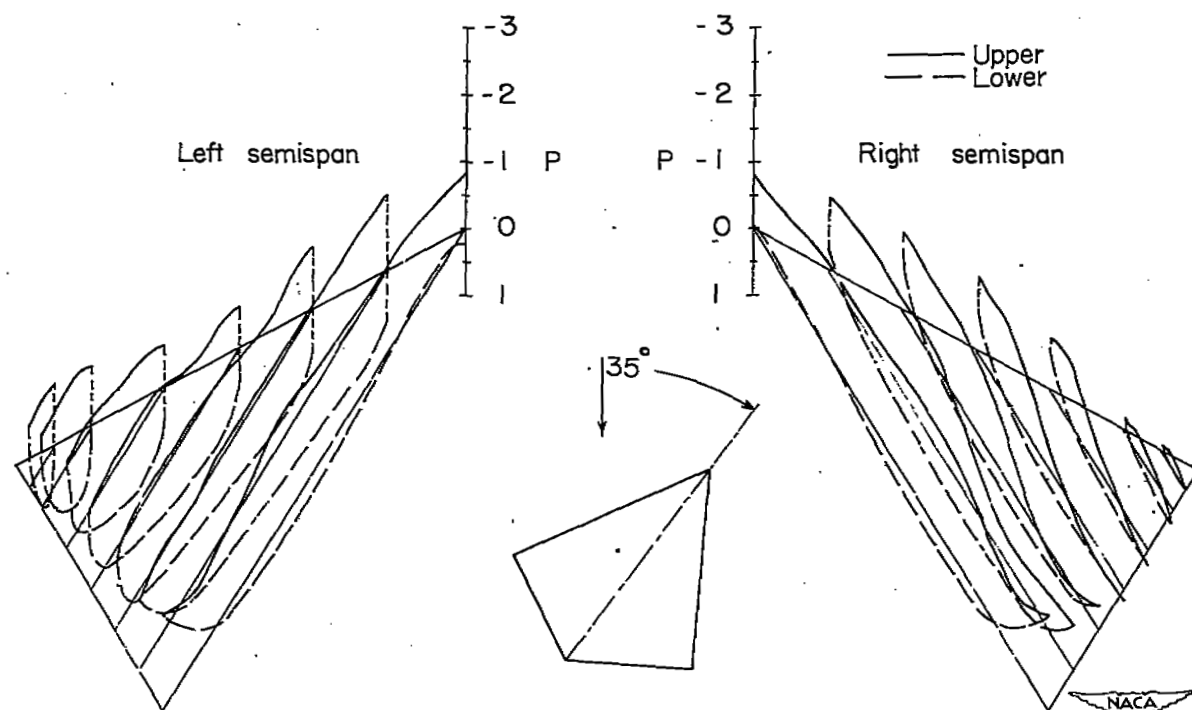
(c)  $\psi = 20^\circ$ .(d)  $\psi = 35^\circ$ .

Figure 26.- Concluded.

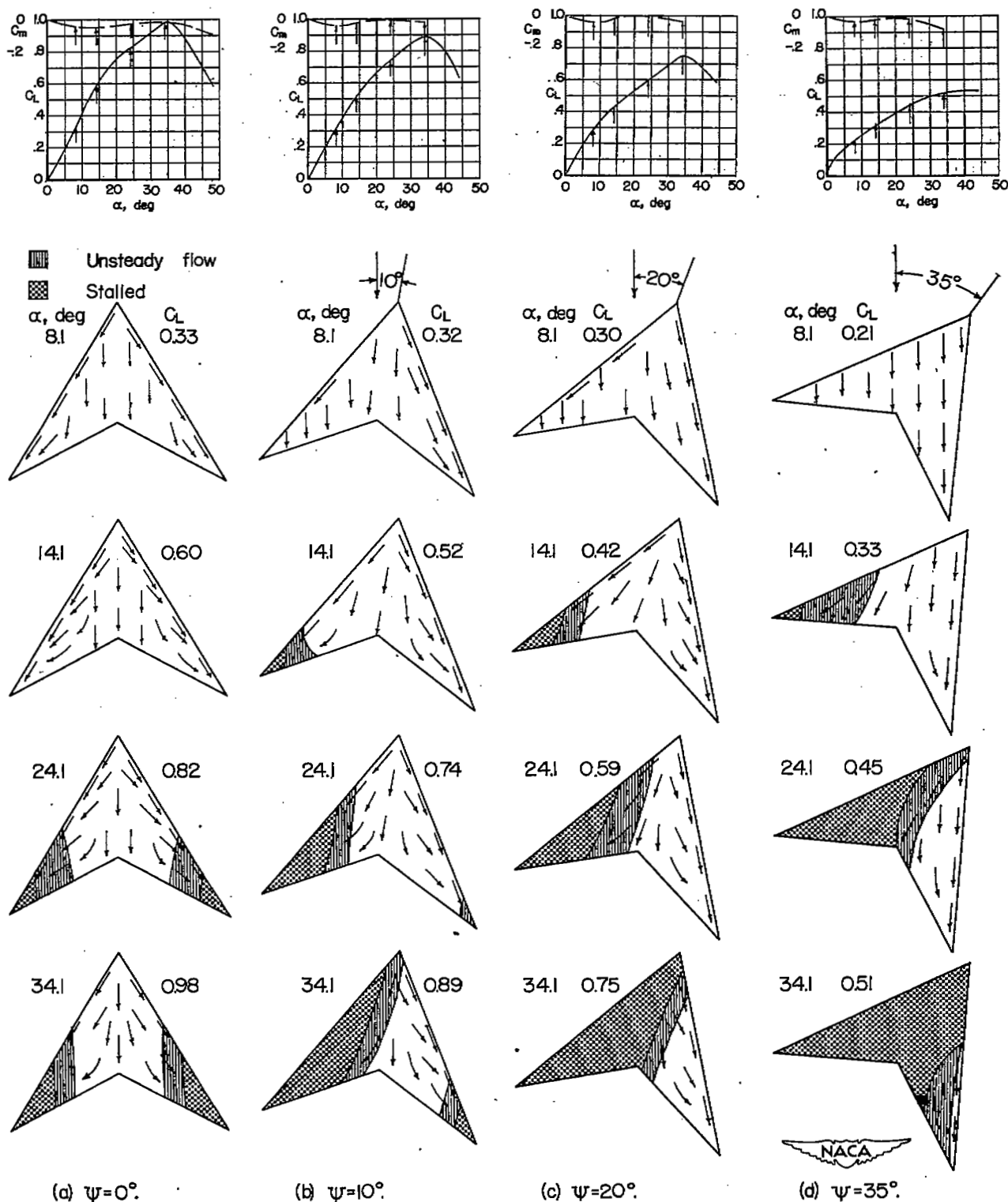


Figure 27.- Flow characteristics over wing 1 as indicated by surface tufts.

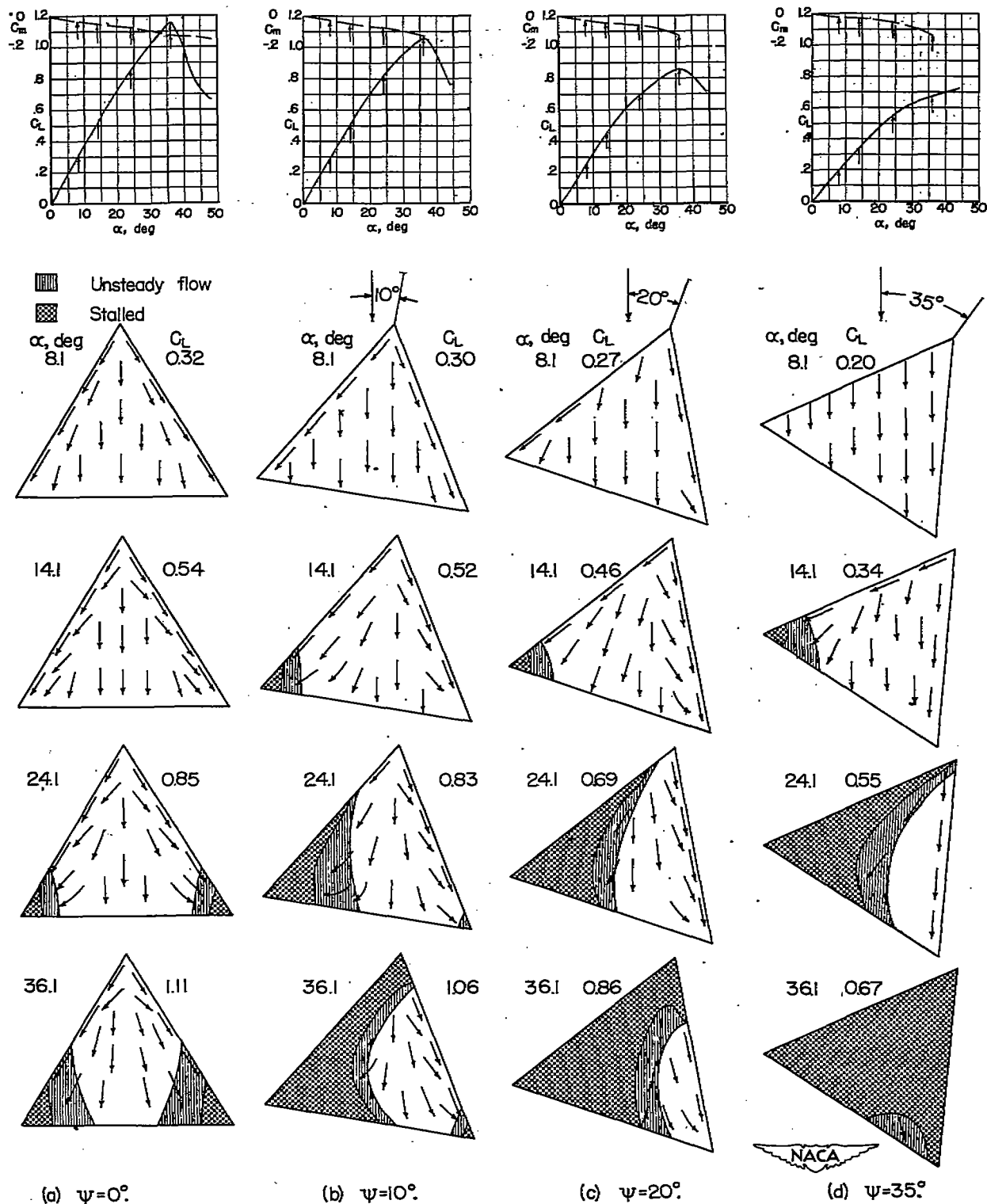


Figure 28.- Flow characteristics over wing 2 as indicated by surface tufts.

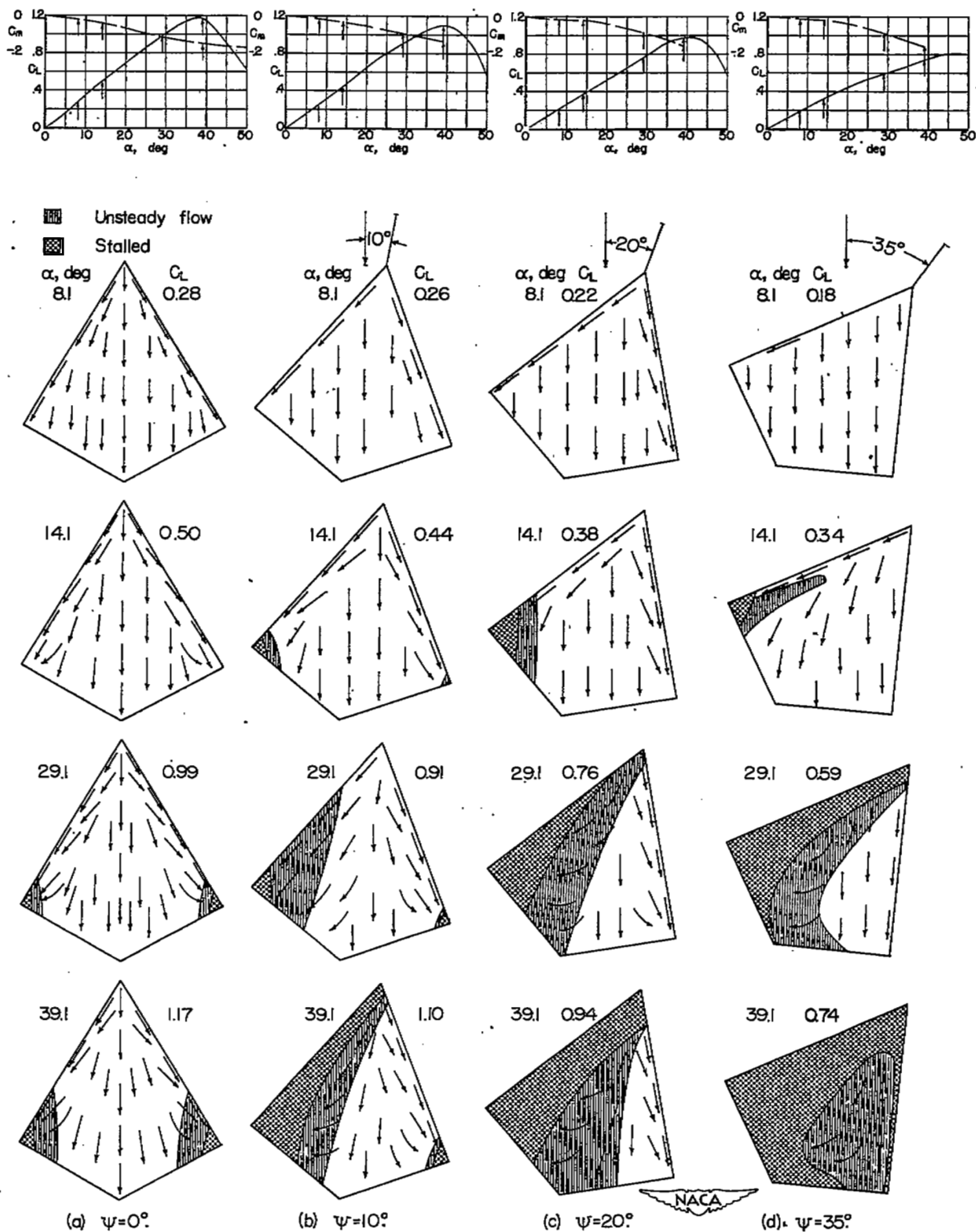
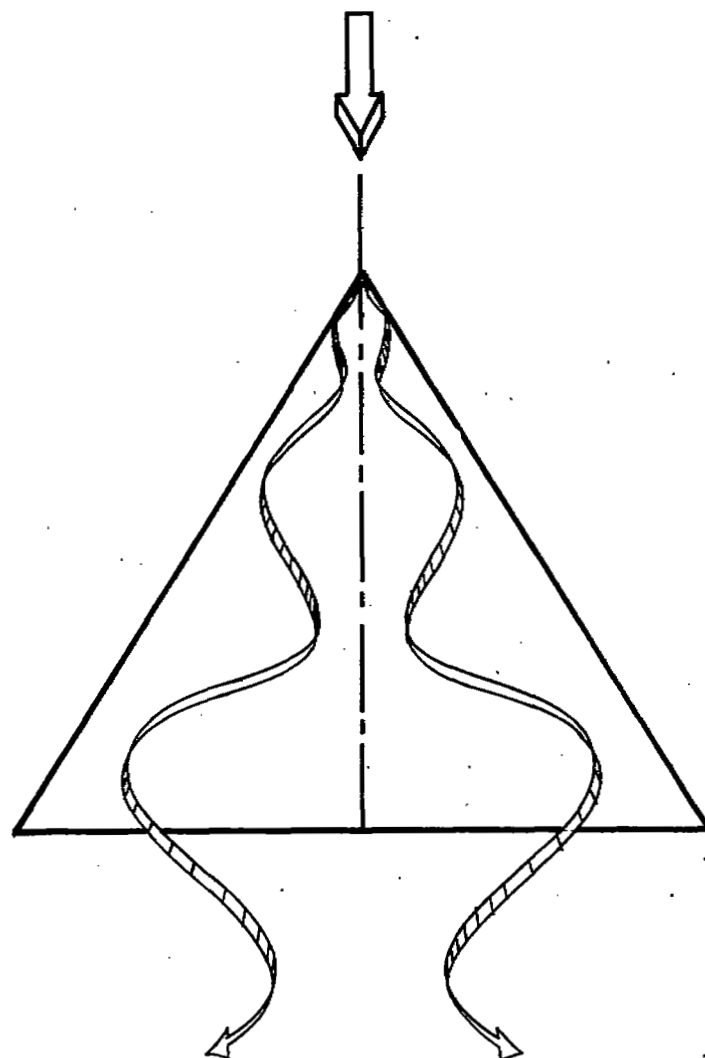
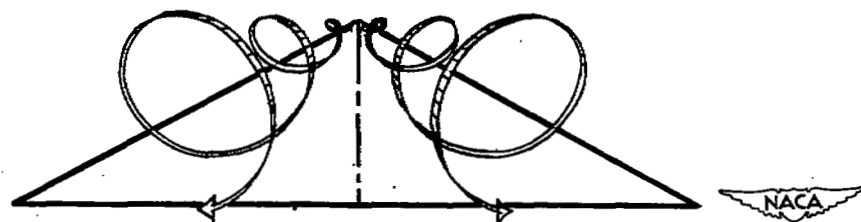


Figure 29.- Flow characteristics over wing 3 as indicated by surface tufts.



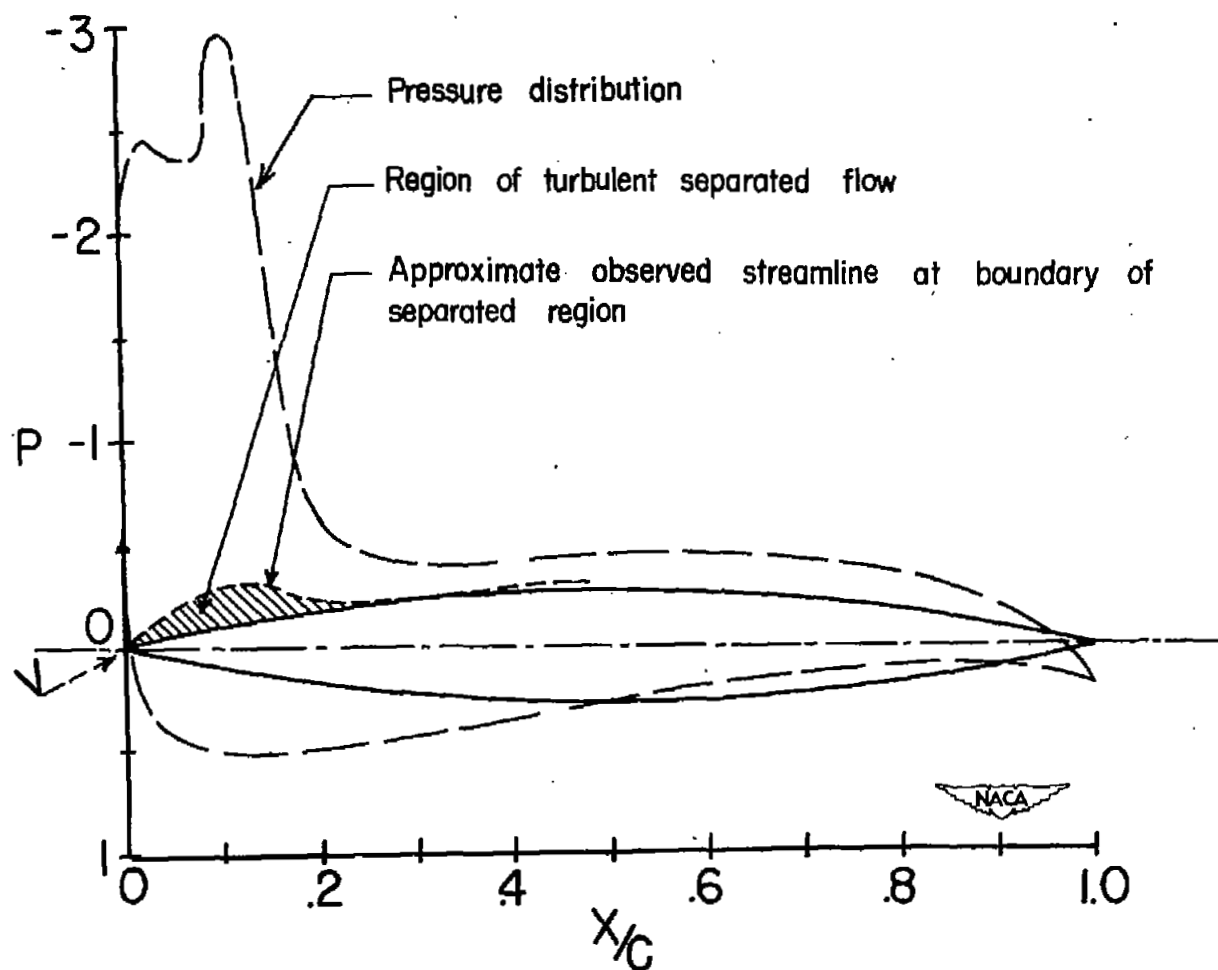


(a) Three-dimensional top view normal to plane of chord lines;  $\alpha=20^\circ$ ;  $\psi=0^\circ$ .



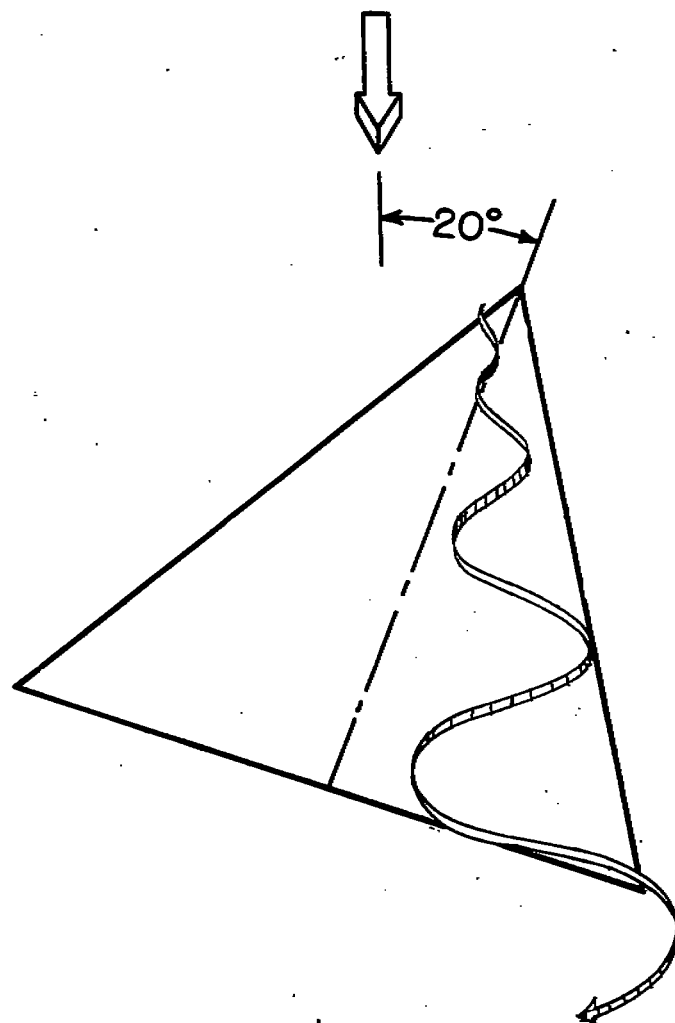
(b) Three-dimensional rear view parallel to air stream;  $\alpha=20^\circ$ ;  $\psi=0^\circ$ .

Figure 30.- Typical vortex flow as observed by smoke-flow and tuft-probing studies over wing 2.

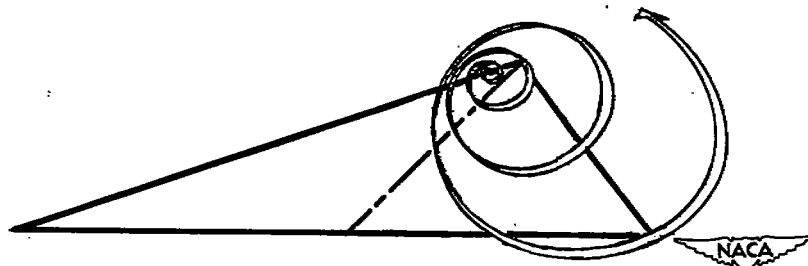


(c) Pressure distribution and cross-sectional view of flow over station 2. of wing 2 at  $\alpha=24.1^\circ$ ;  $\psi=0^\circ$ .

Figure 30.- Continued.



(d) Three-dimensional top view normal to plane of chord lines;  $\alpha=20^\circ$ ;  $\psi=20^\circ$ .



(e) Three-dimensional rear view parallel to air stream;  $\alpha=20^\circ$ ;  $\psi=20^\circ$ .

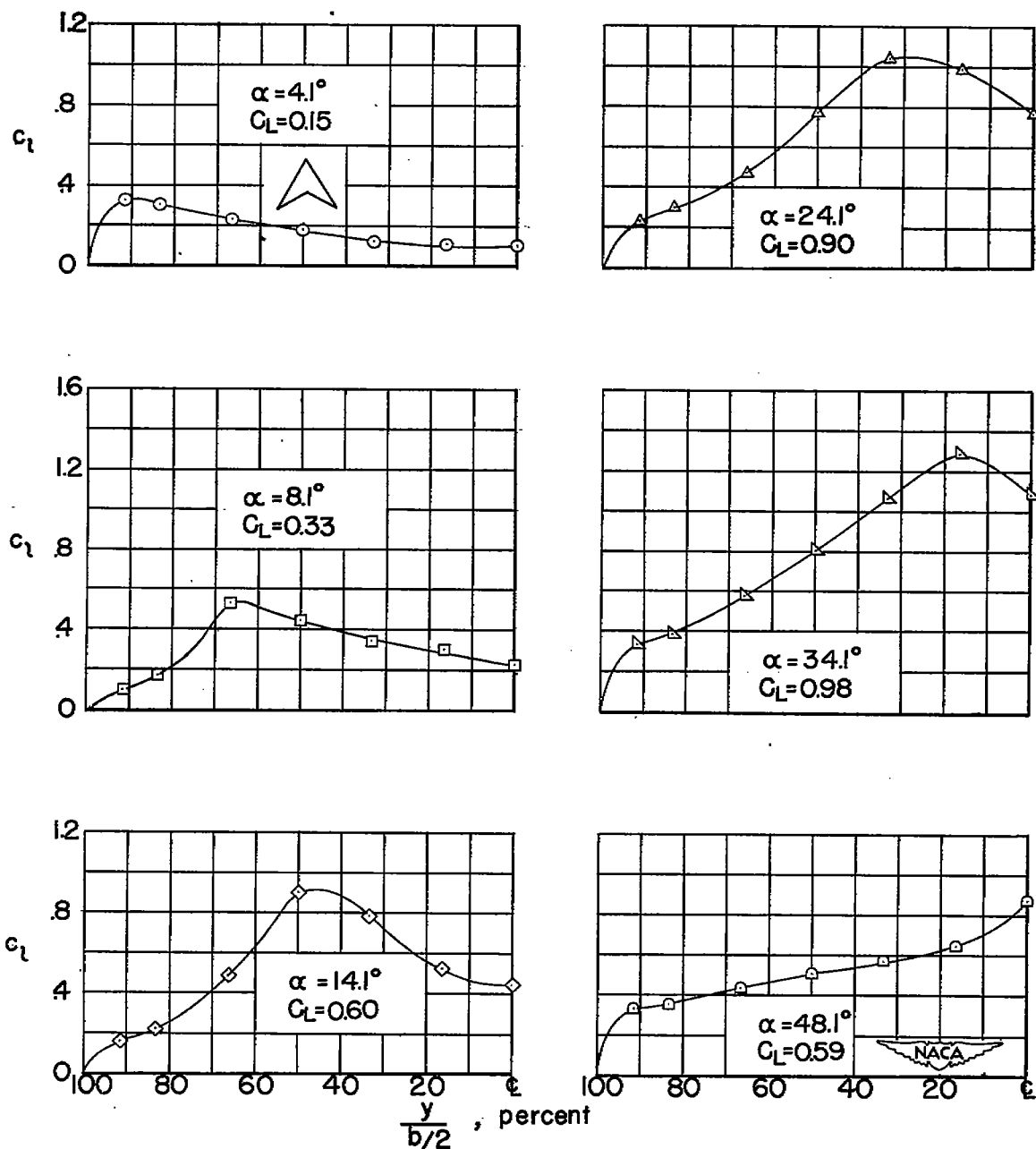


Figure 31.- Effect of  $\alpha$  on the spanwise  $c_l$  variation of wing 1;  
 $\psi = 0^\circ$ .

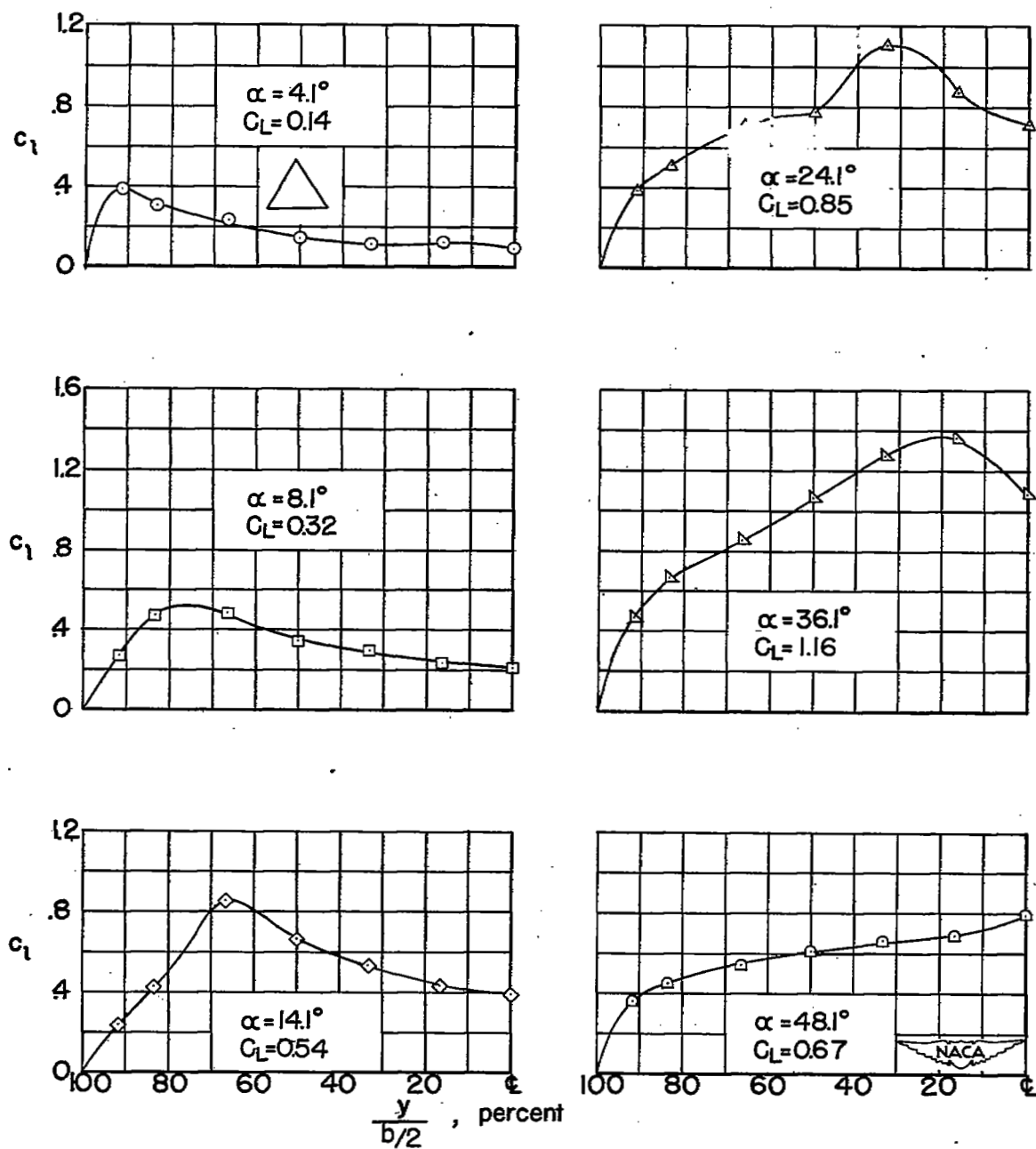


Figure 32.- Effect of  $\alpha$  on the spanwise  $c_l$  variation of wing 2;  
 $\psi = 0^\circ$ .

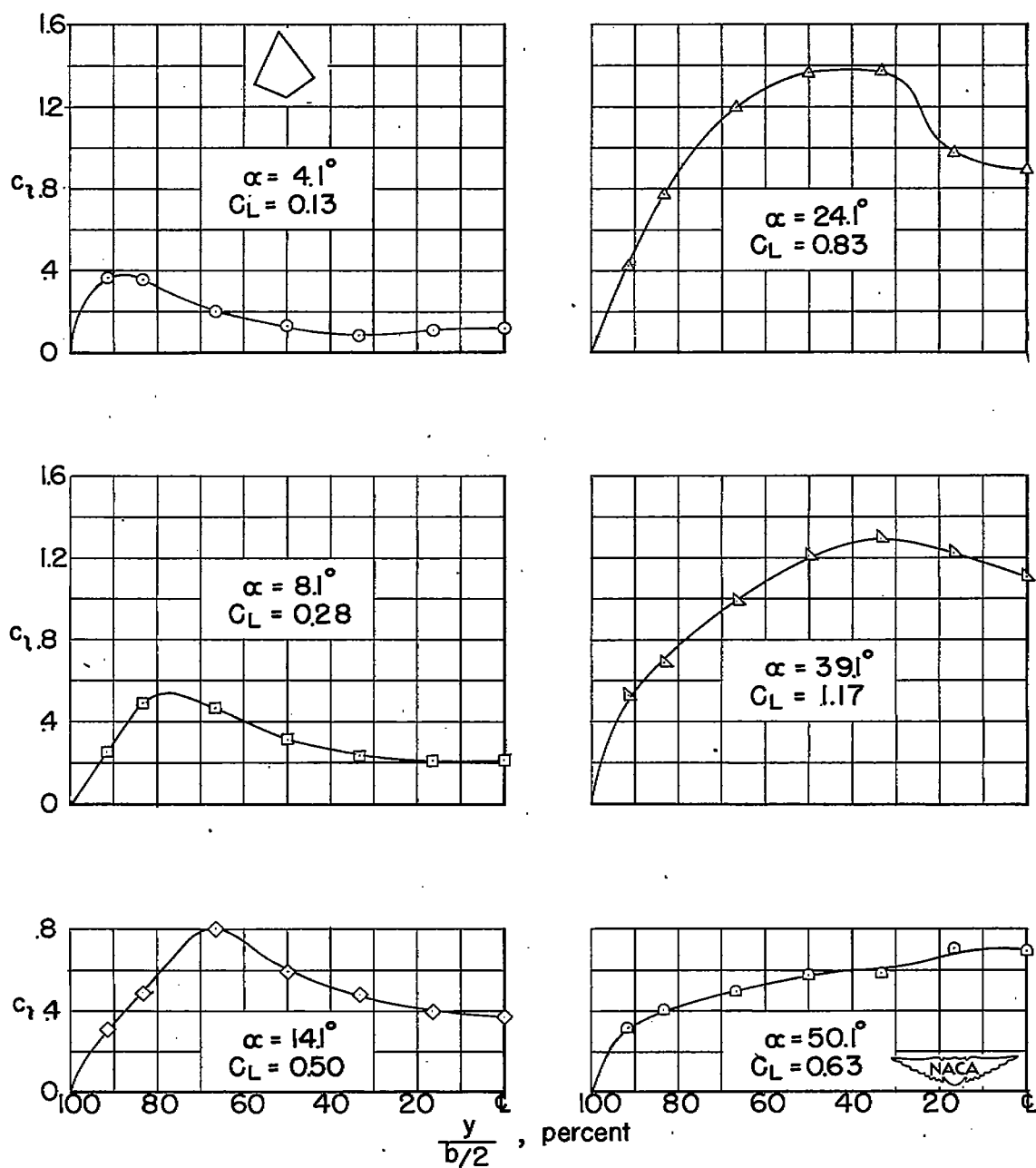


Figure 33.- Effect of  $\alpha$  on the spanwise  $c_l$  variation of wing 3;  
 $\psi = 0^\circ$ .

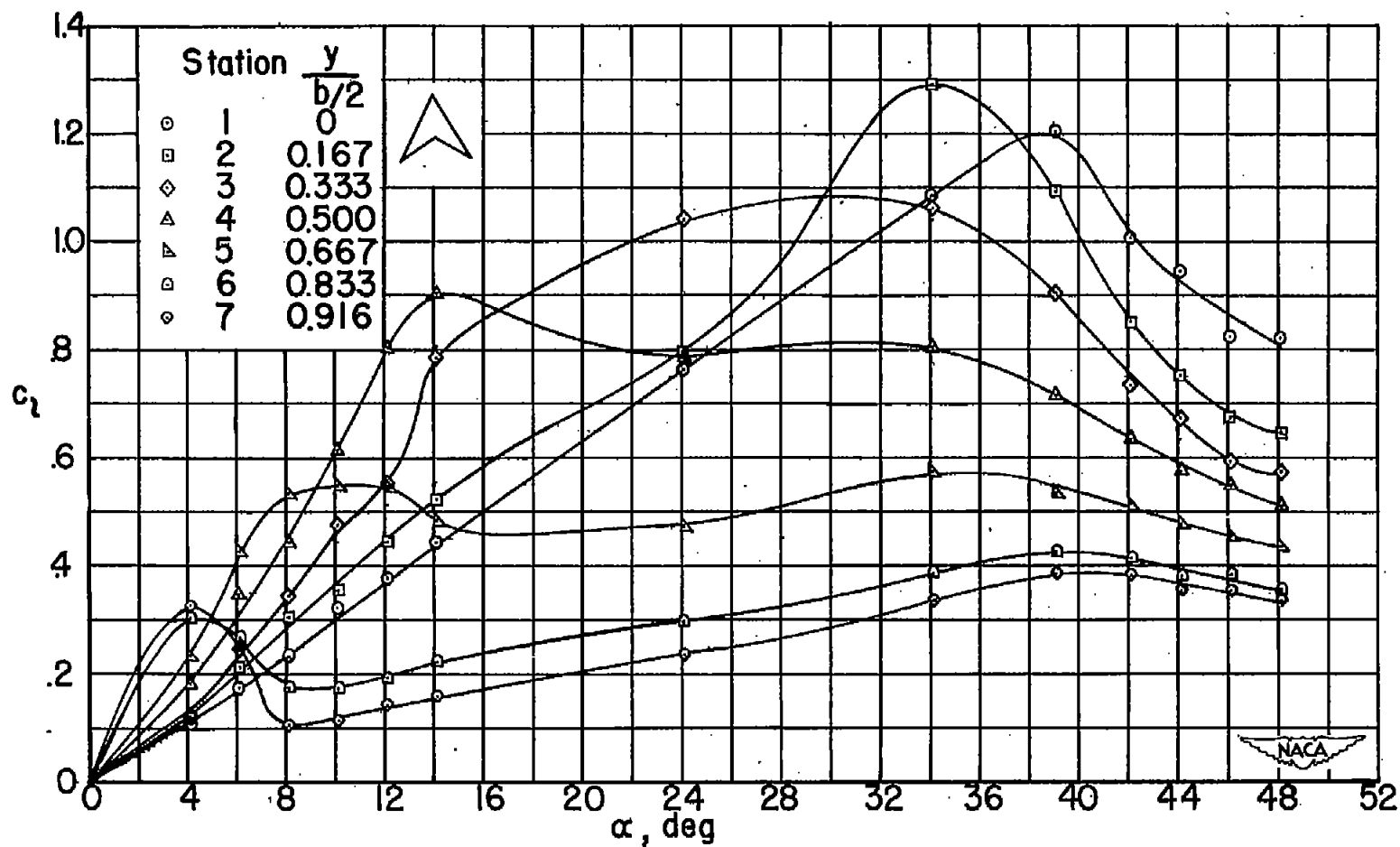


Figure 34.- Variation of  $c_l$  with  $\alpha$  at seven stations along the semispan of wing 1;  $\psi = 0^\circ$ .

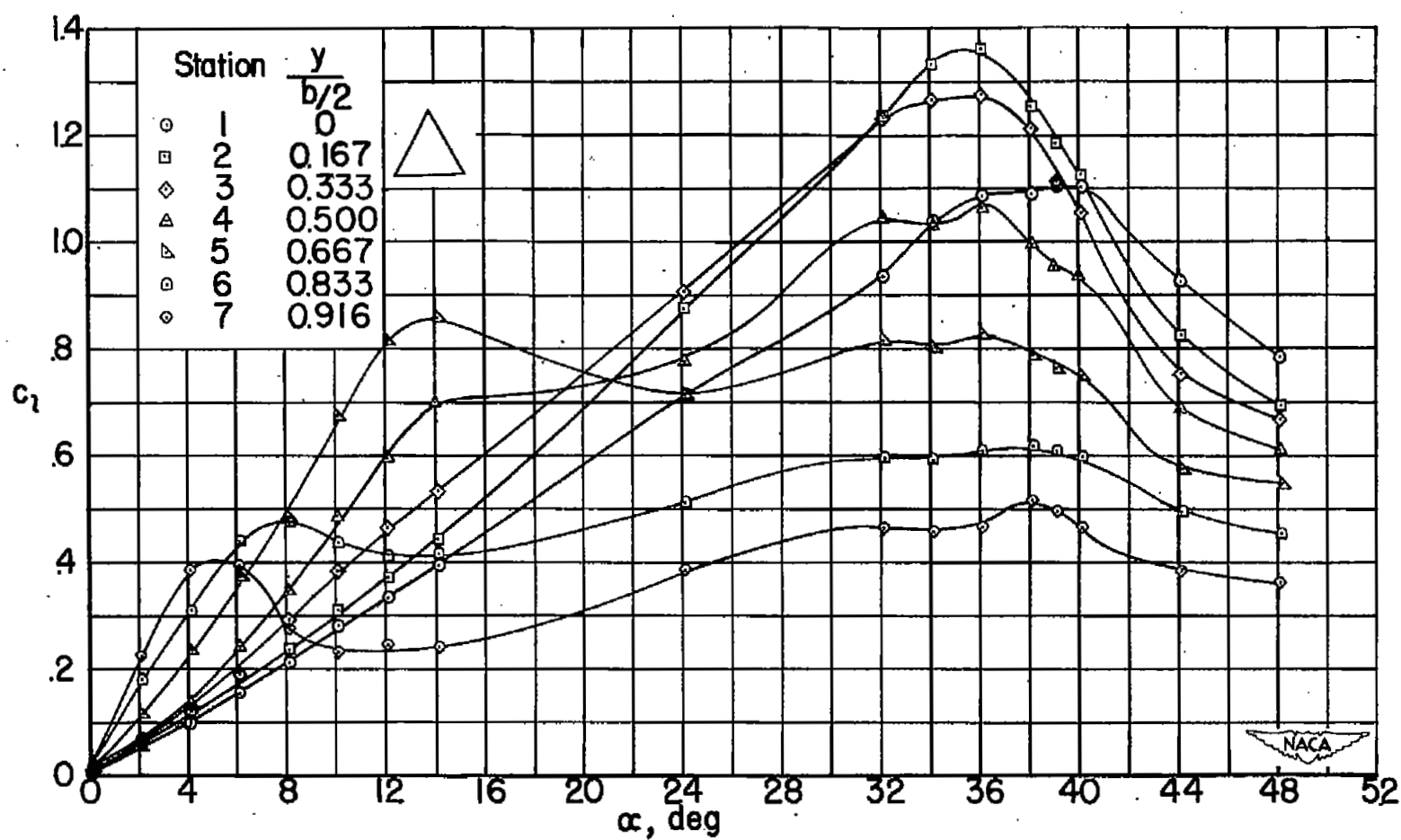


Figure 35.- Variation of  $c_l$  with  $\alpha$  at seven stations along the semispan of wing 2;  $\psi = 0^\circ$ .



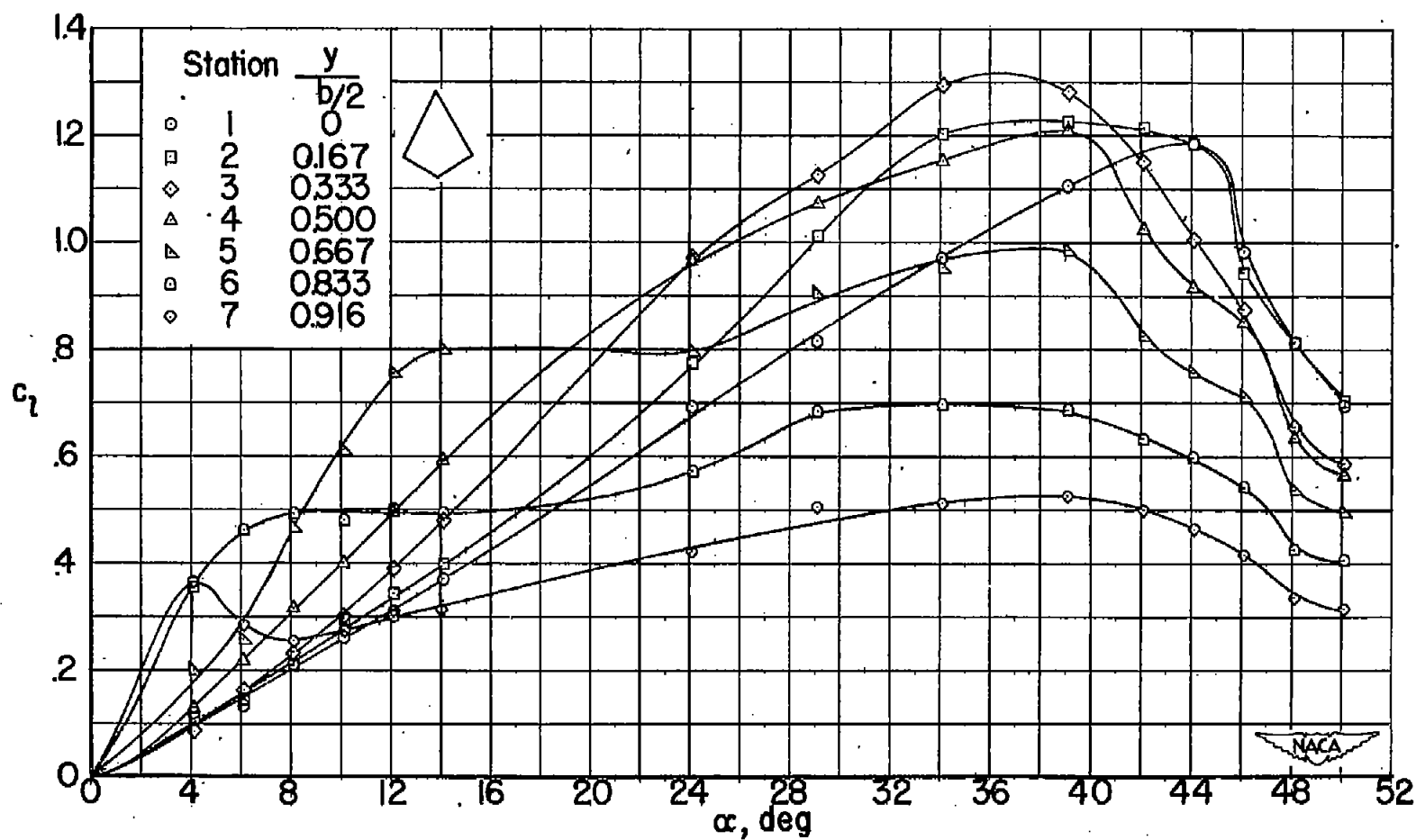


Figure 36.- Variation of  $c_l$  with  $\alpha$  at seven stations along the semispan of wing 3;  $\psi = 0^\circ$ .

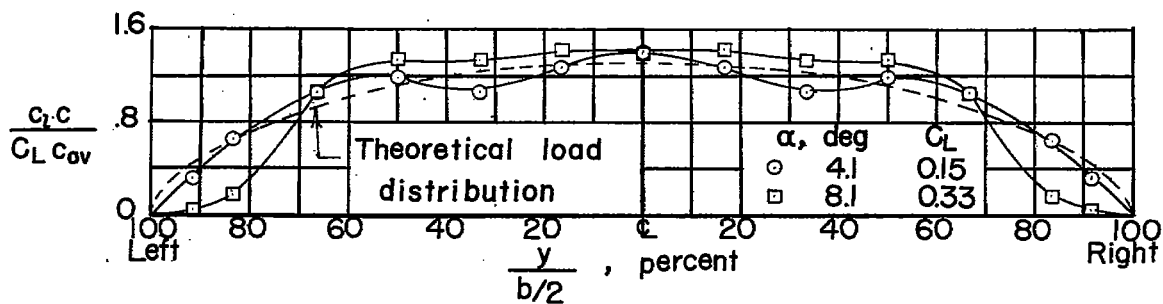
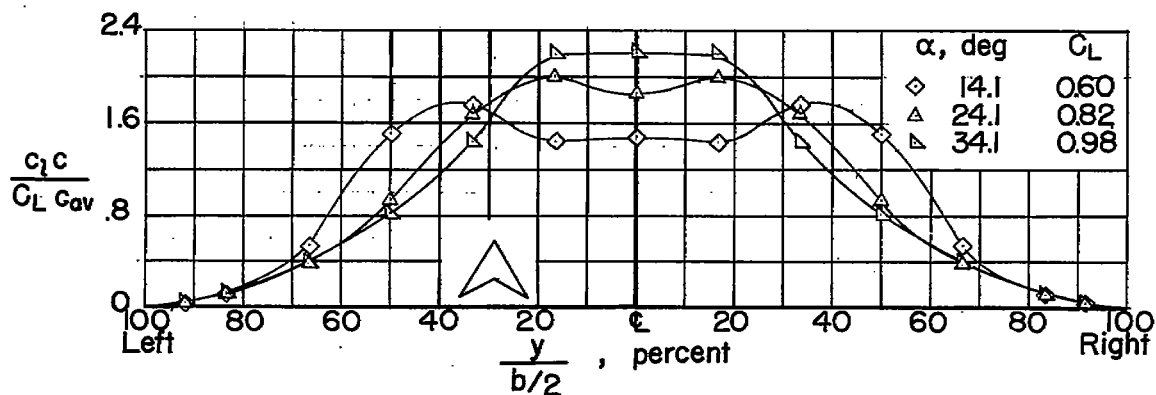
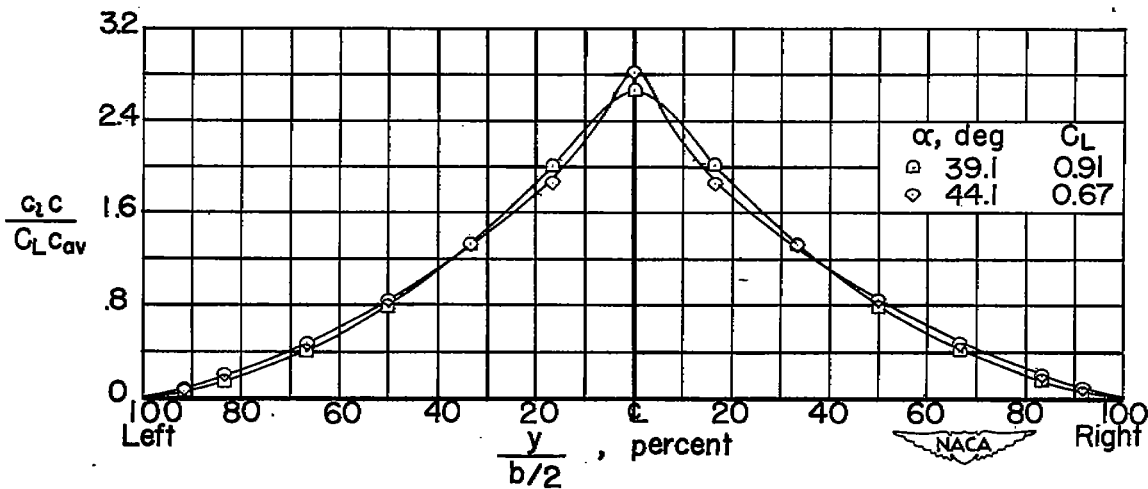
(a) Angles of attack:  $4.1^\circ$ ,  $8.1^\circ$ (b) Angles of attack:  $14.1^\circ$ ,  $24.1^\circ$ ,  $34.1^\circ$ (c) Angles of attack:  $39.1^\circ$ ,  $44.1^\circ$ 

Figure 37.- Span load distribution of wing 1 at various angles of attack;  $\psi = 0^\circ$ . All data are taken over left semispan.

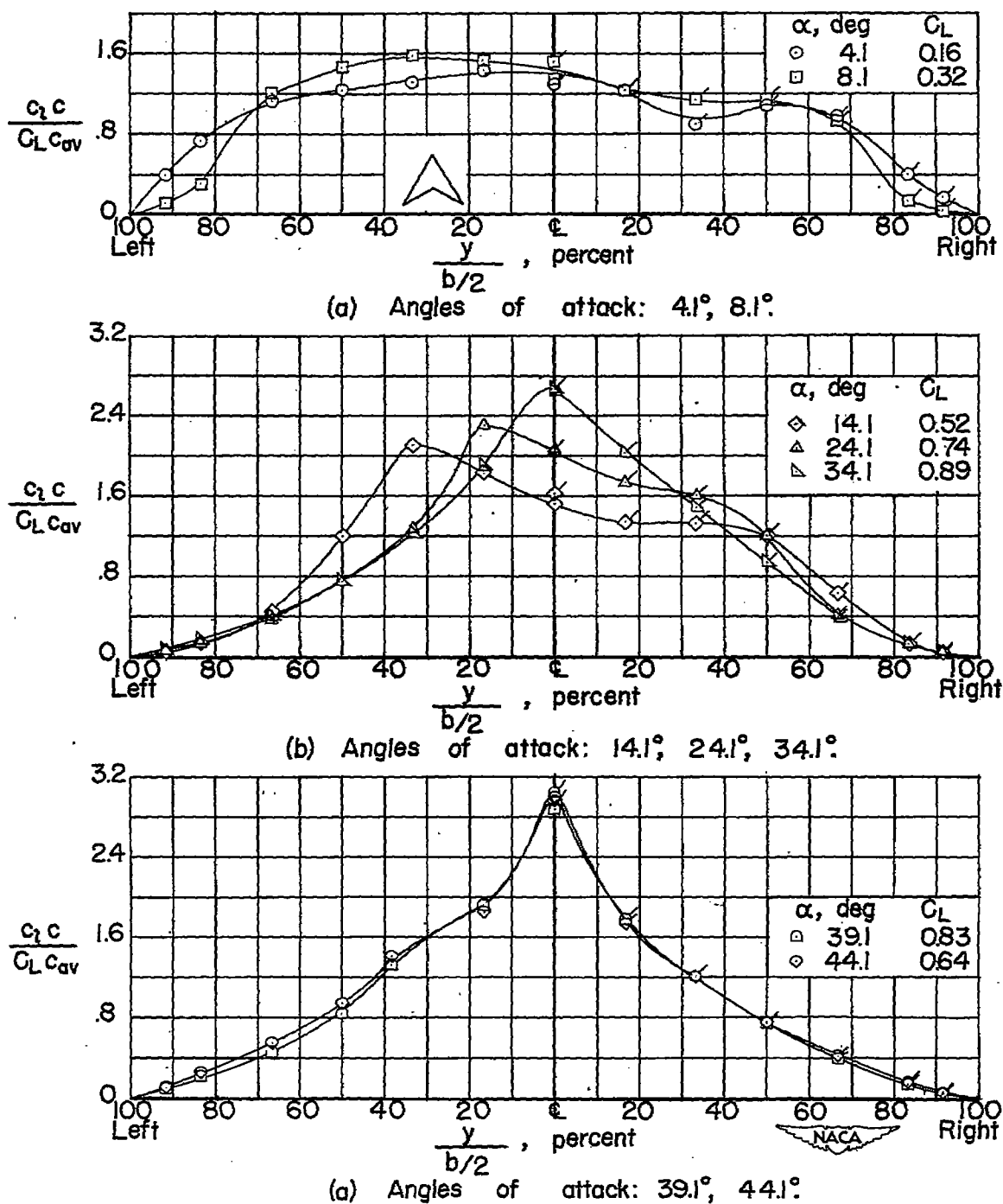


Figure 38.- Span load distribution of wing 1 at various angles of attack;  $\psi = 10^\circ$ . Flagged symbols represent data taken with left semispan at  $\psi = -10^\circ$ .

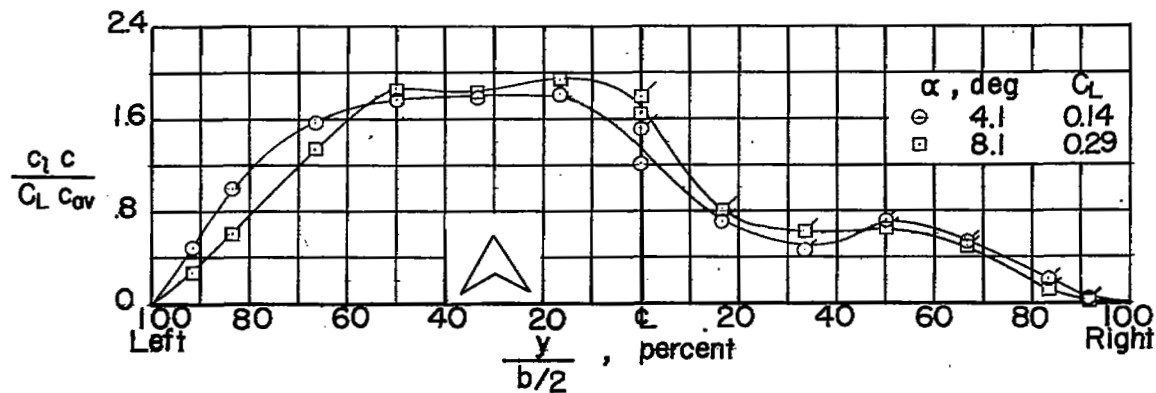
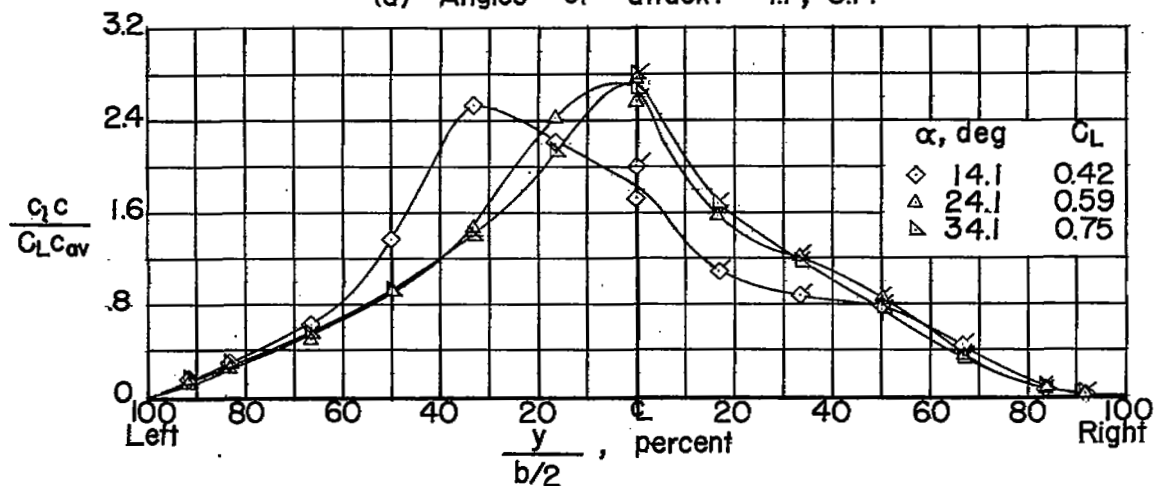
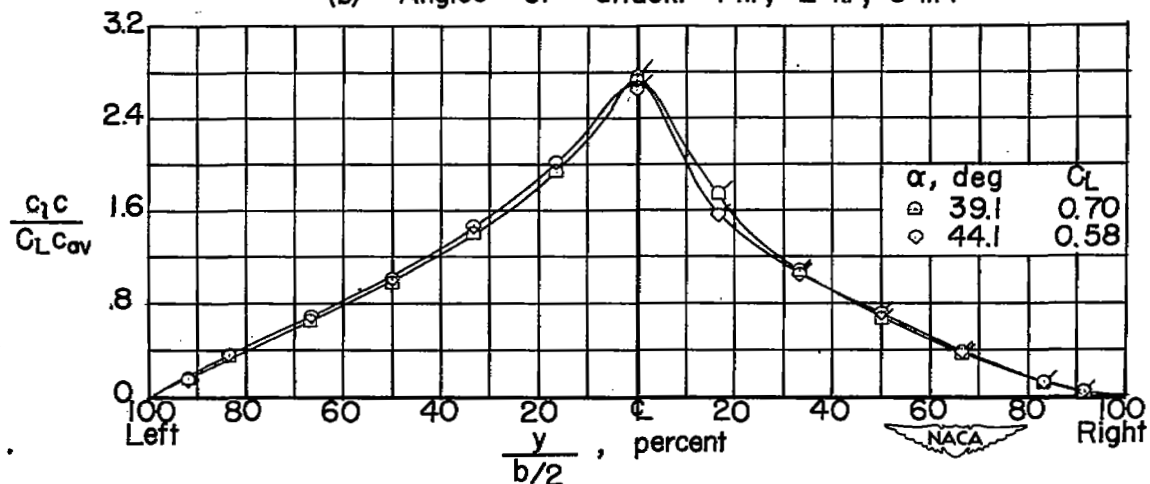
(a) Angles of attack:  $4.1^\circ$ ,  $8.1^\circ$ (b) Angles of attack:  $14.1^\circ$ ,  $24.1^\circ$ ,  $34.1^\circ$ (c) Angles of attack:  $39.1^\circ$ ,  $44.1^\circ$ 

Figure 39.- Span load distribution of wing 1 at various angles of attack;  $\psi = 20^\circ$ . Flagged symbols represent data taken with left semispan at  $\psi = -20^\circ$ .

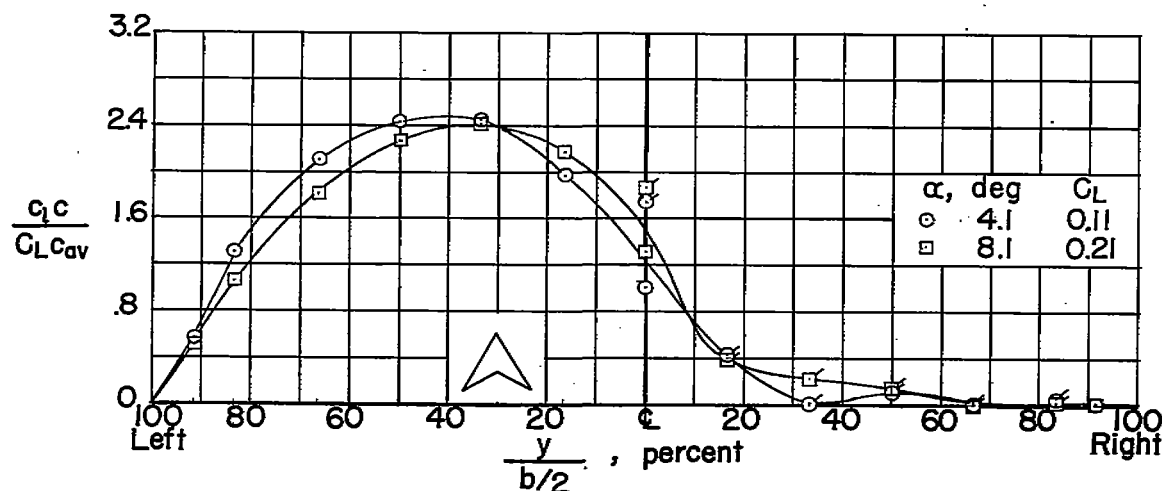
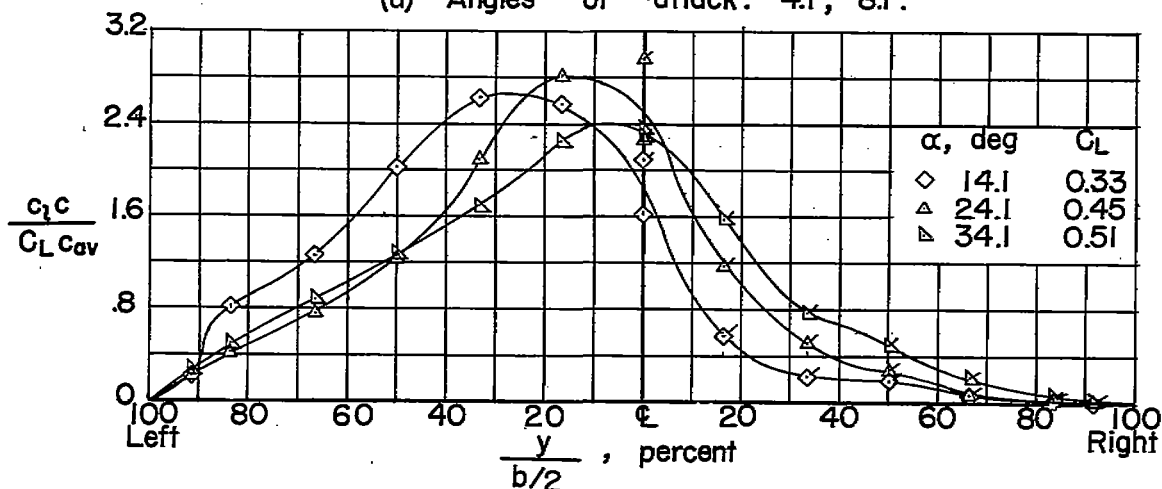
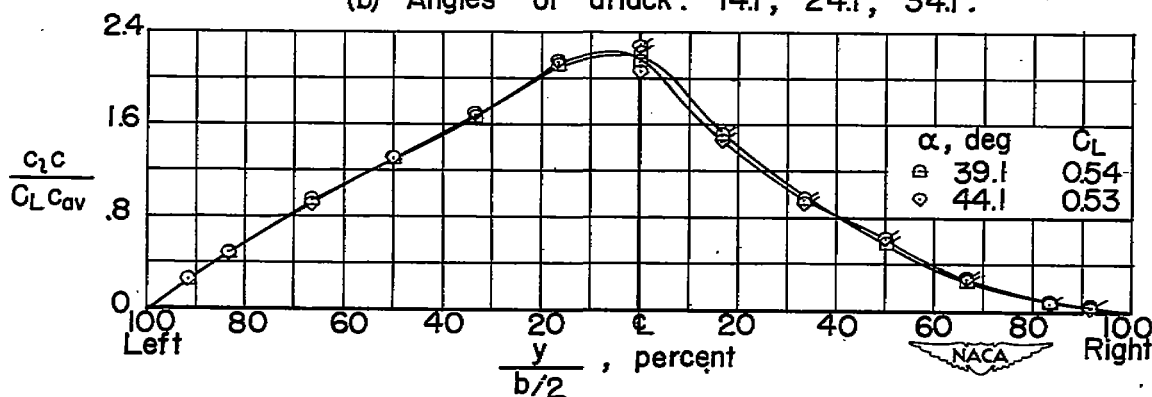
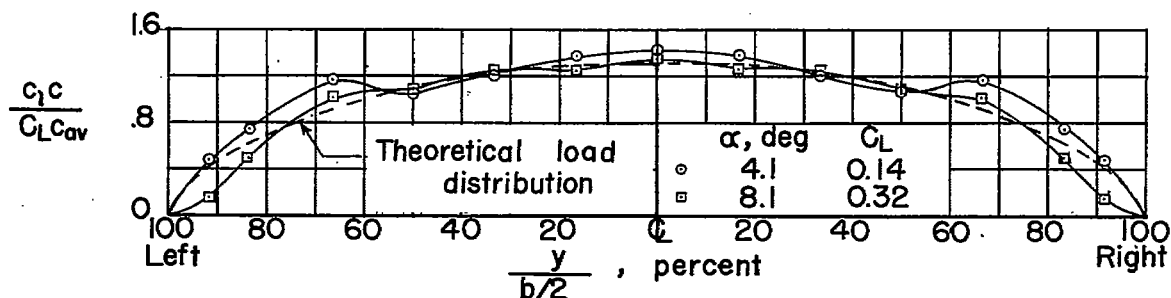
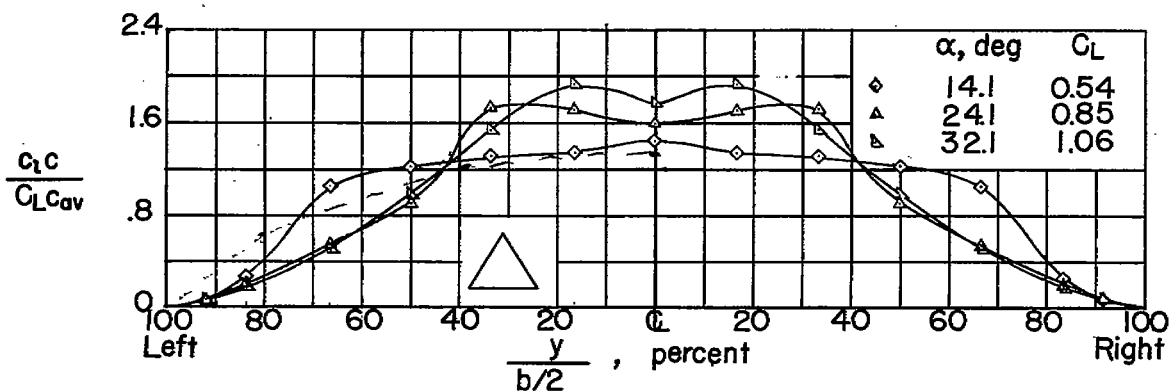
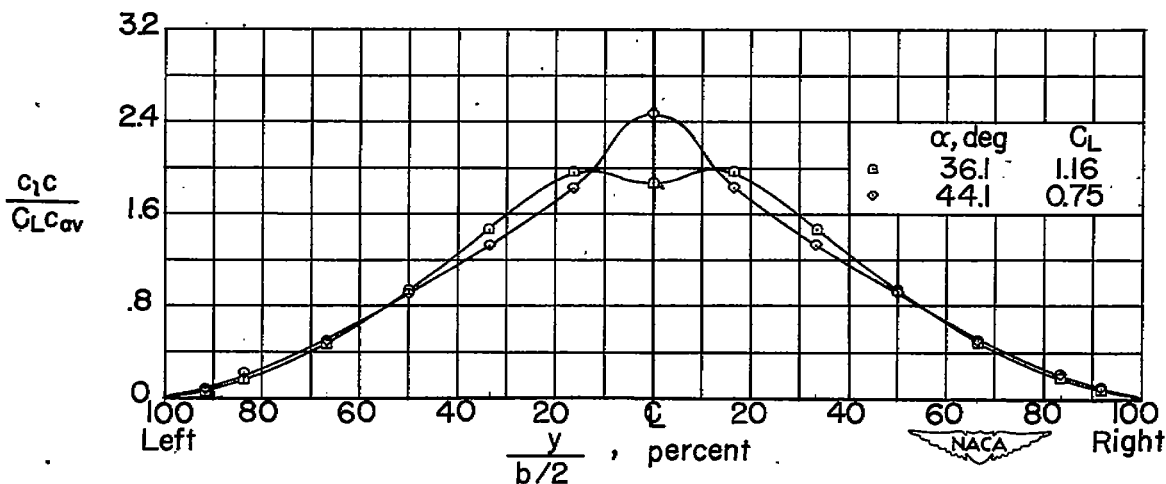
(a) Angles of attack:  $4.1^\circ$ ,  $8.1^\circ$ .(b) Angles of attack:  $14.1^\circ$ ,  $24.1^\circ$ ,  $34.1^\circ$ .(c) Angles of attack:  $39.1^\circ$ ,  $44.1^\circ$ .

Figure 40.- Span load distribution of wing 1 at various angles of attack;  $\psi = 35^\circ$ . Flagged symbols represent data taken with left semispan at  $\psi = -35^\circ$ .

(a) Angles of attack:  $4.1^\circ$ ,  $8.1^\circ$ .(b) Angles of attack:  $14.1^\circ$ ,  $24.1^\circ$ ,  $32.1^\circ$ .(c) Angles of attack:  $36.1^\circ$ ,  $44.1^\circ$ .Figure 41.- Span load distribution of wing 2 at various angles of attack;  $\psi = 0^\circ$ . All data are taken over left semispan.

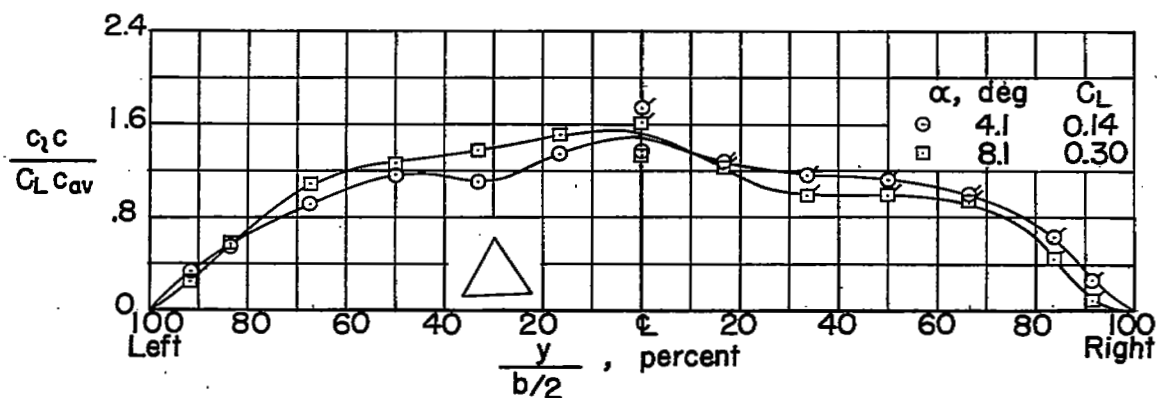
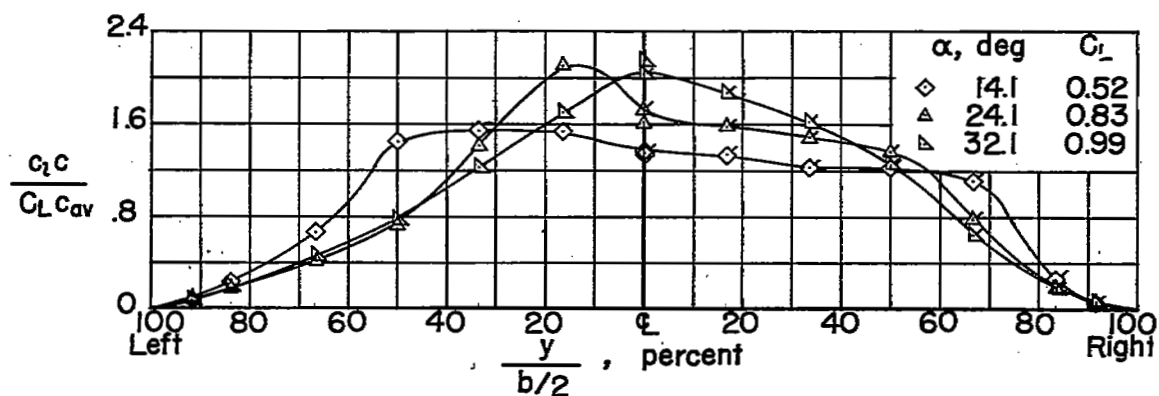
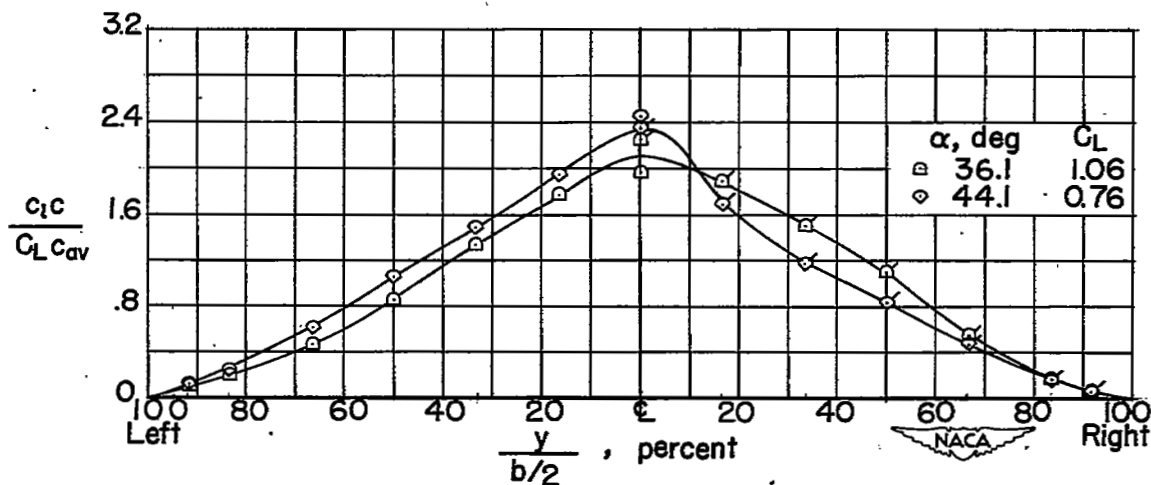
(a) Angles of attack:  $4.1^\circ$ ,  $8.1^\circ$ .(b) Angles of attack:  $14.1^\circ$ ,  $24.1^\circ$ ,  $32.1^\circ$ .(c) Angles of attack:  $36.1^\circ$ ,  $44.1^\circ$ .

Figure 42.- Span load distribution of wing 2 at various angles of attack;  $\psi = 10^\circ$ . Flagged symbols represent data taken with left semispan at  $\psi = -10^\circ$ .

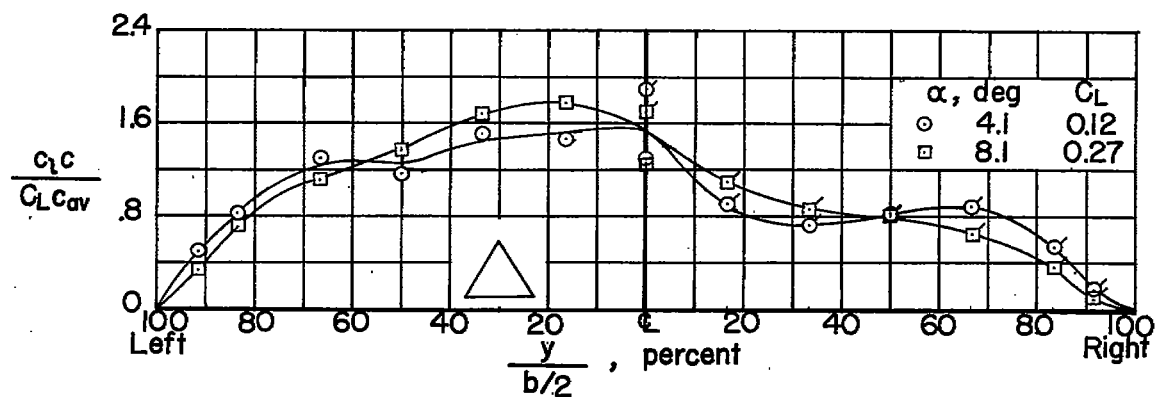
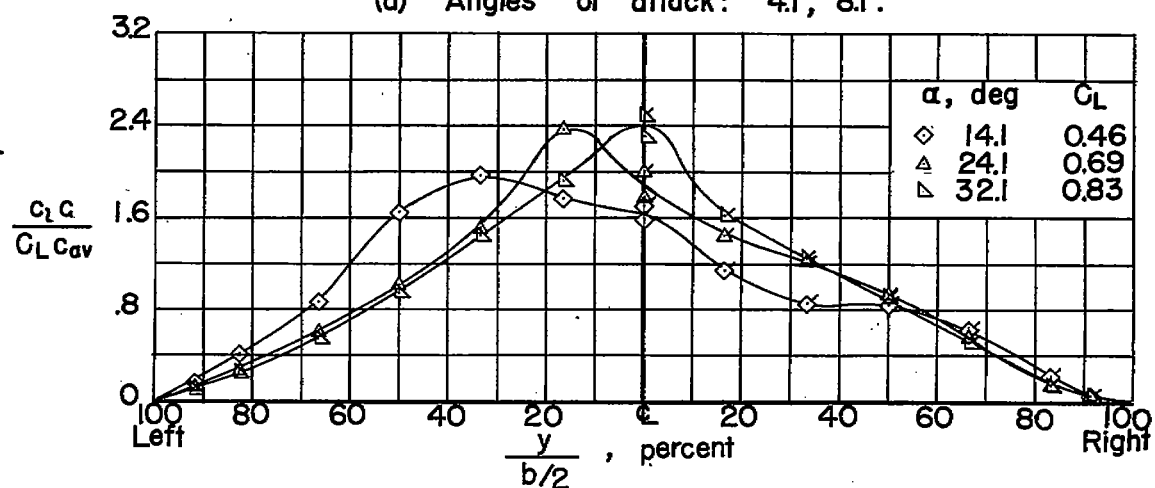
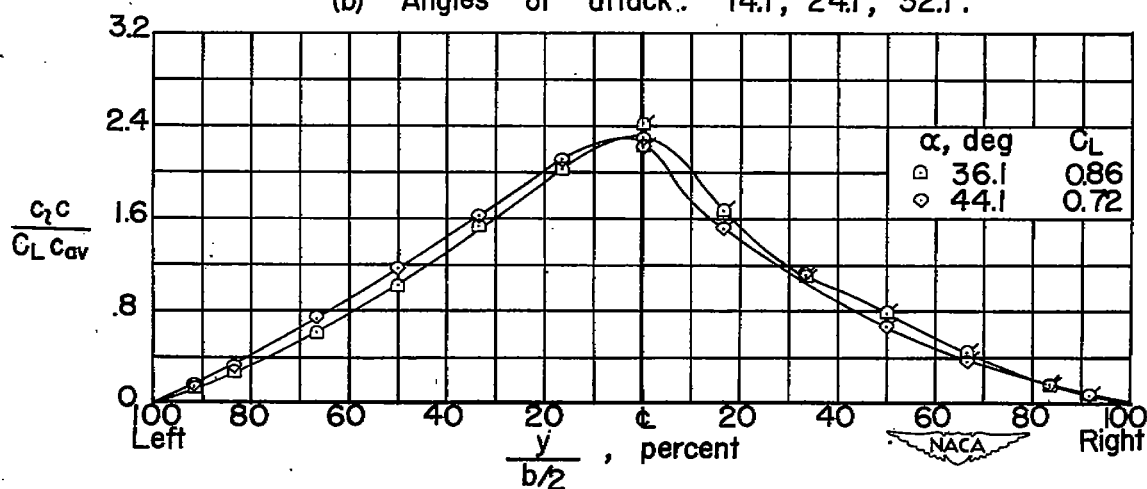
(a) Angles of attack:  $4.1^\circ$ ,  $8.1^\circ$ .(b) Angles of attack:  $14.1^\circ$ ,  $24.1^\circ$ ,  $32.1^\circ$ .(c) Angles of attack:  $36.1^\circ$ ,  $44.1^\circ$ .

Figure 43.- Span load distribution of wing 2 at various angles of attack;  $\psi = 20^\circ$ . Flagged symbols represent data taken with left semispan at  $\psi = -20^\circ$ .



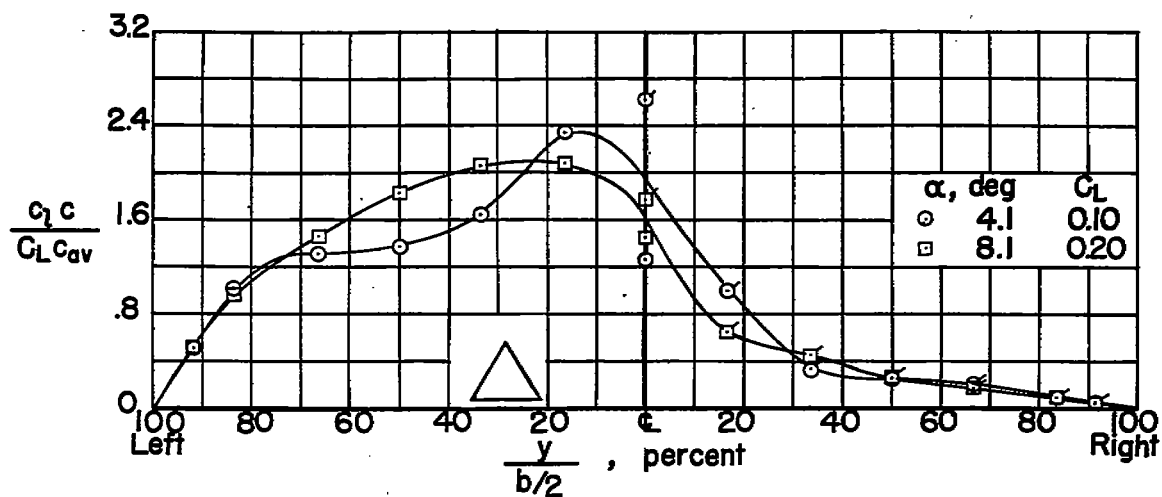
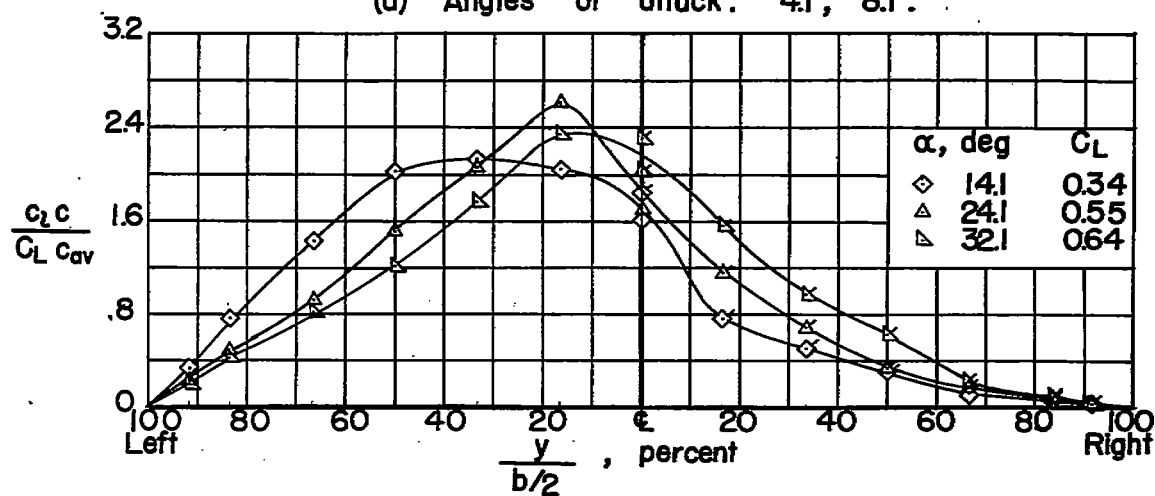
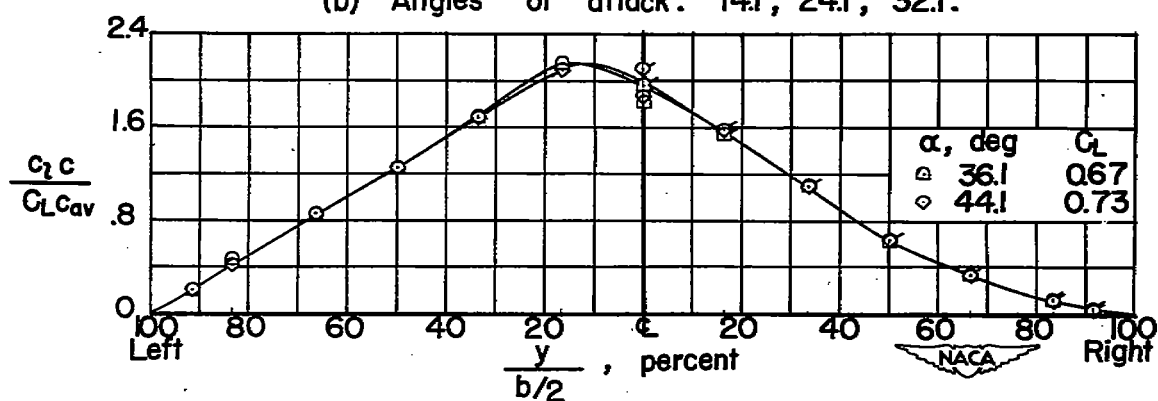
(a) Angles of attack:  $4.1^\circ$ ,  $8.1^\circ$ .(b) Angles of attack:  $14.1^\circ$ ,  $24.1^\circ$ ,  $32.1^\circ$ .(c) Angles of attack:  $36.1^\circ$ ,  $44.1^\circ$ .

Figure 44.- Span load distribution of wing 2 at various angles of attack;  $\psi = 35^\circ$ . Flagged symbols represent data taken with left semispan at  $\psi = -35^\circ$ .

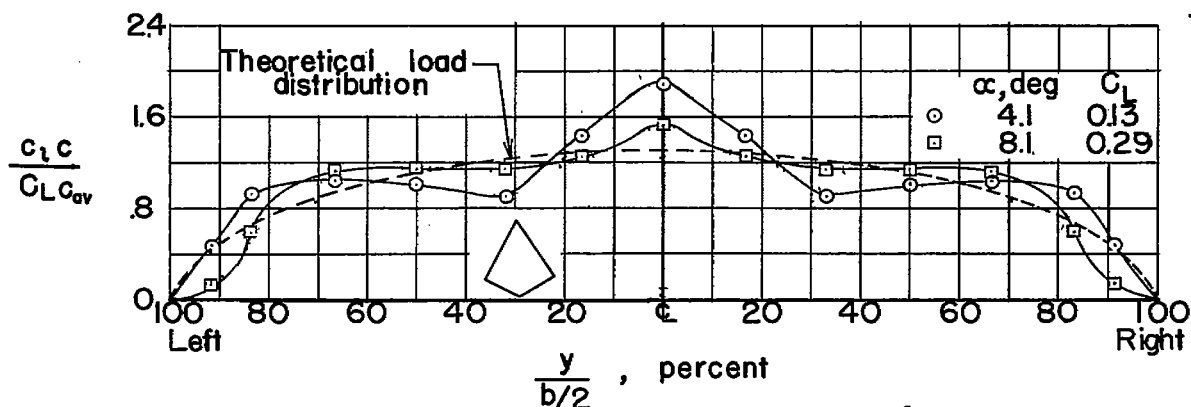
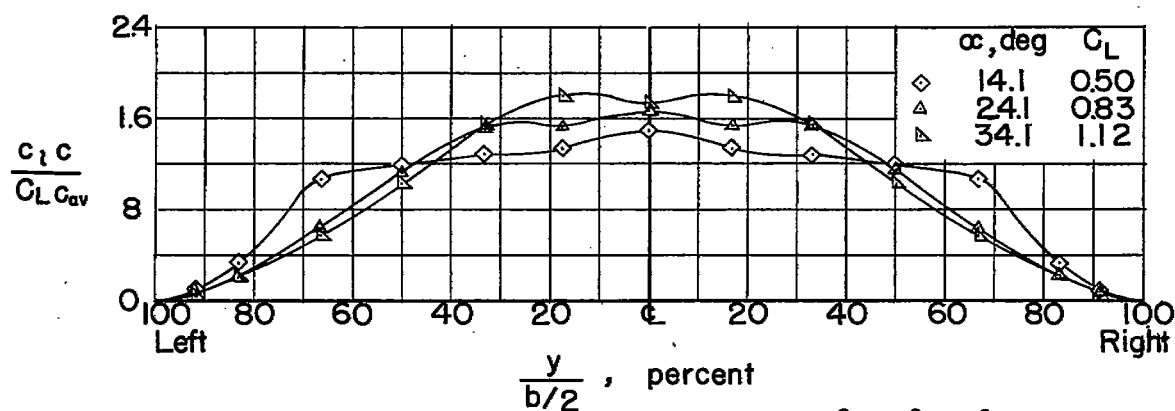
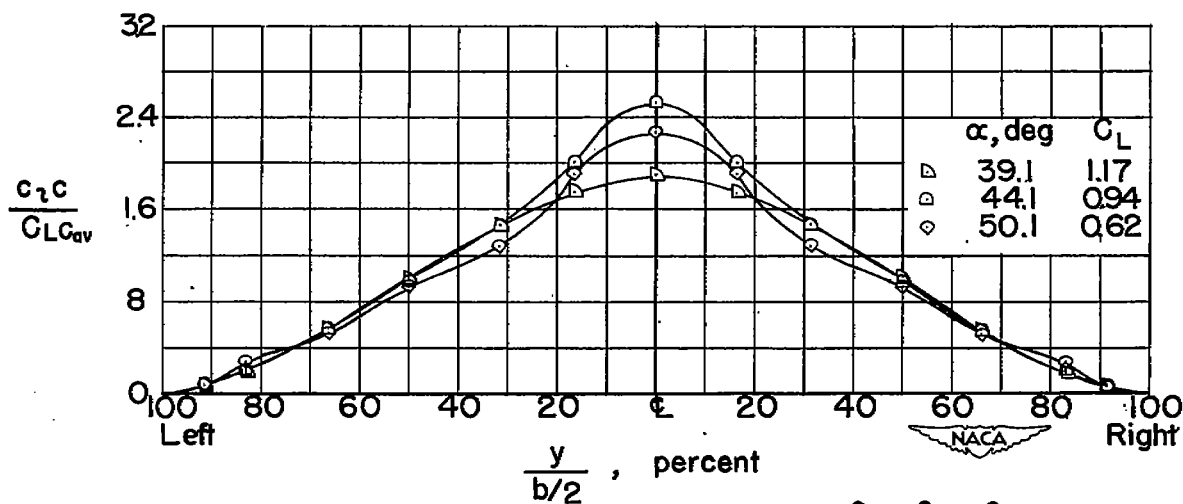
(a) Angles of attack :  $4.1^\circ, 8.1^\circ$ .(b) Angles of attack :  $14.1^\circ, 24.1^\circ, 34.1^\circ$ .(c) Angles of attack :  $39.1^\circ, 44.1^\circ, 50.1^\circ$ .

Figure 45.- Span load distribution of wing 3 at various angles of attack;  $\psi = 0^\circ$ . All data are taken over left semispan.

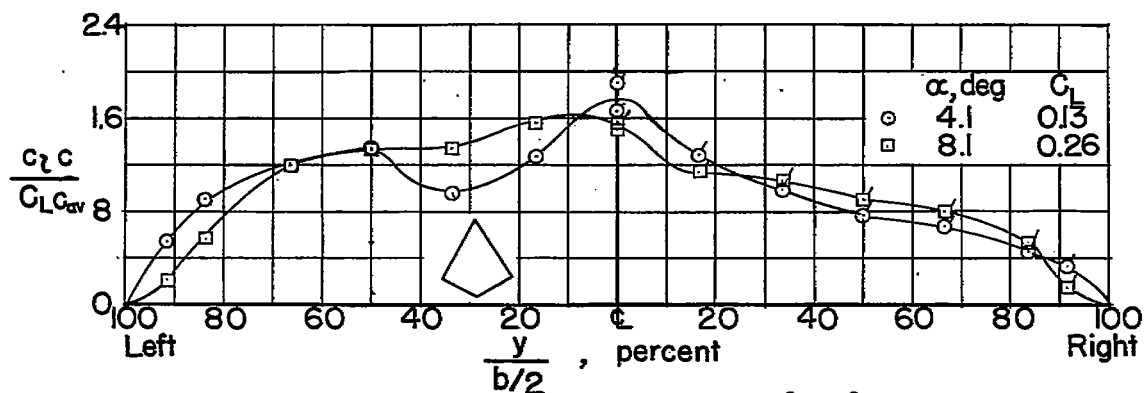
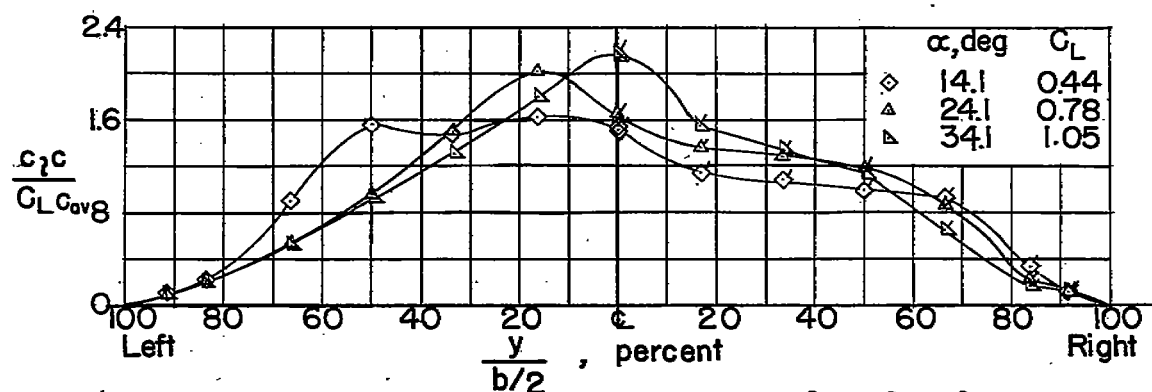
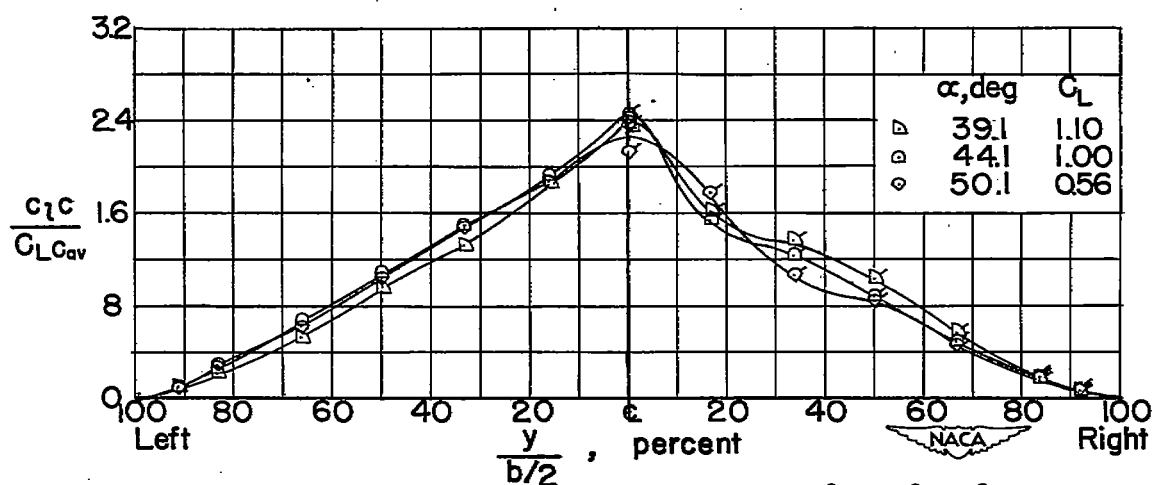
(a) Angles of attack :  $4.1^\circ, 8.1^\circ$ .(b) Angles of attack :  $14.1^\circ, 24.1^\circ, 34.1^\circ$ .(c) Angles of attack :  $39.1^\circ, 44.1^\circ, 50.1^\circ$ 

Figure 46.- Span load distribution of wing 3 at various angles of attack;  $\psi = 10^\circ$ . Flagged symbols represent data taken with left semispan at  $\psi = -10^\circ$ .

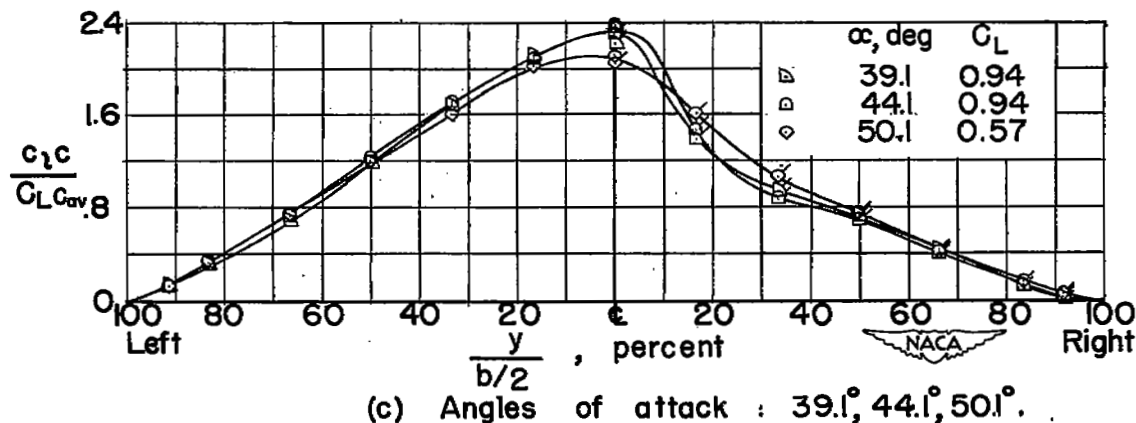
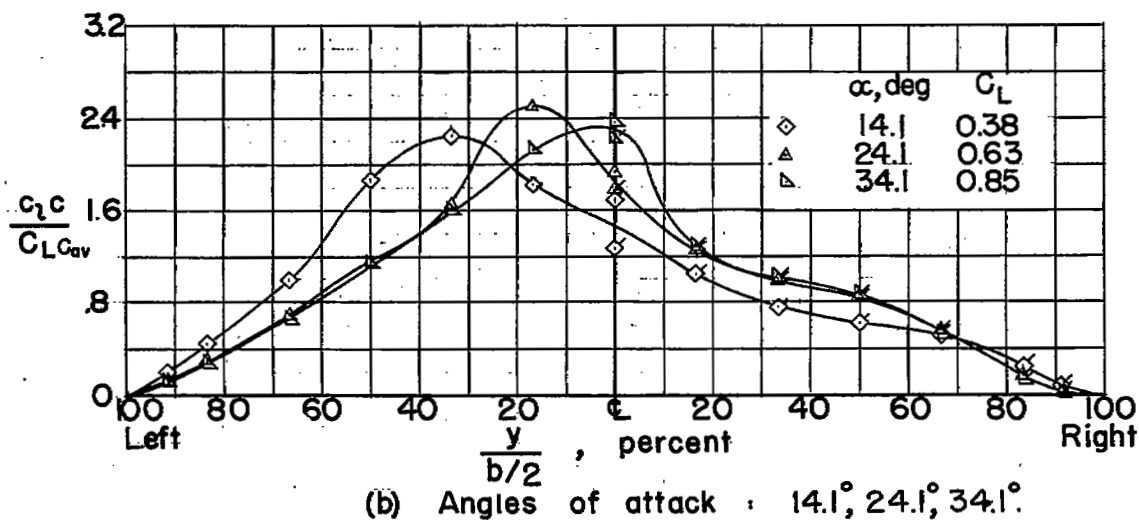
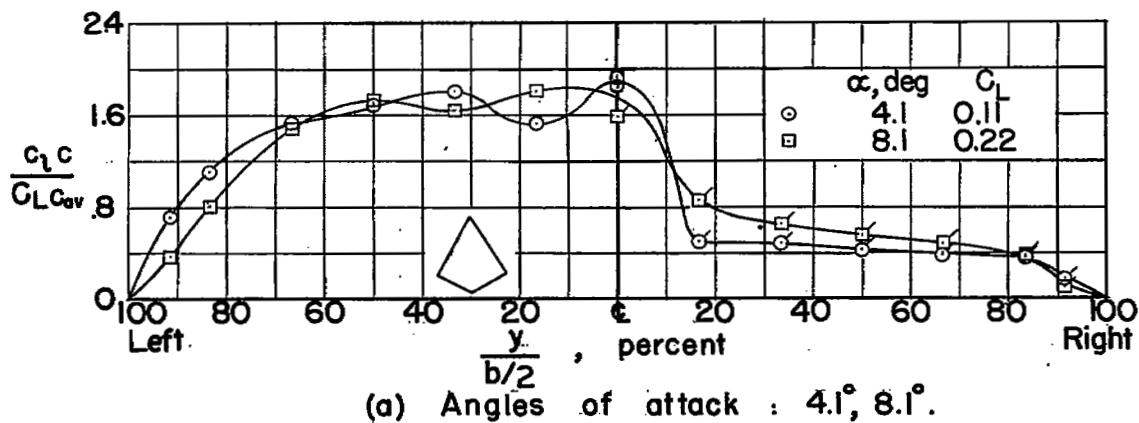
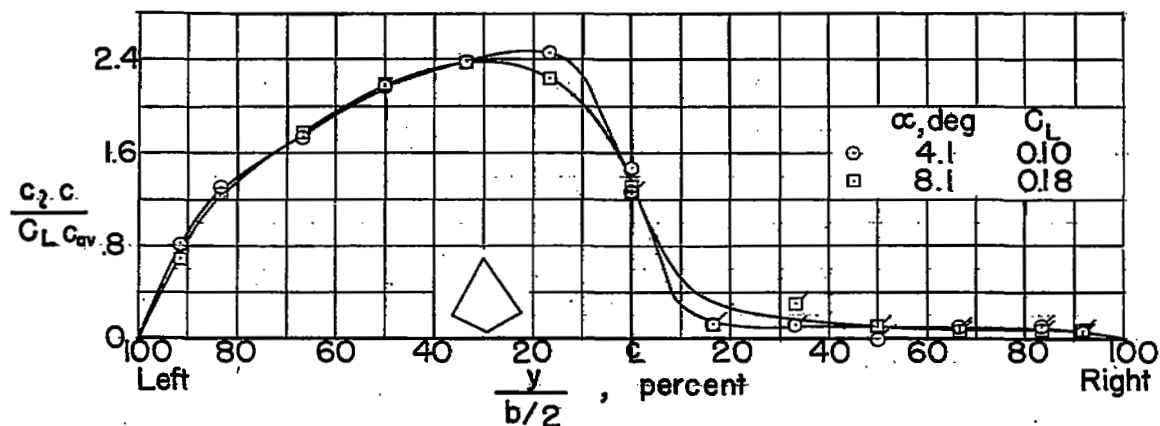
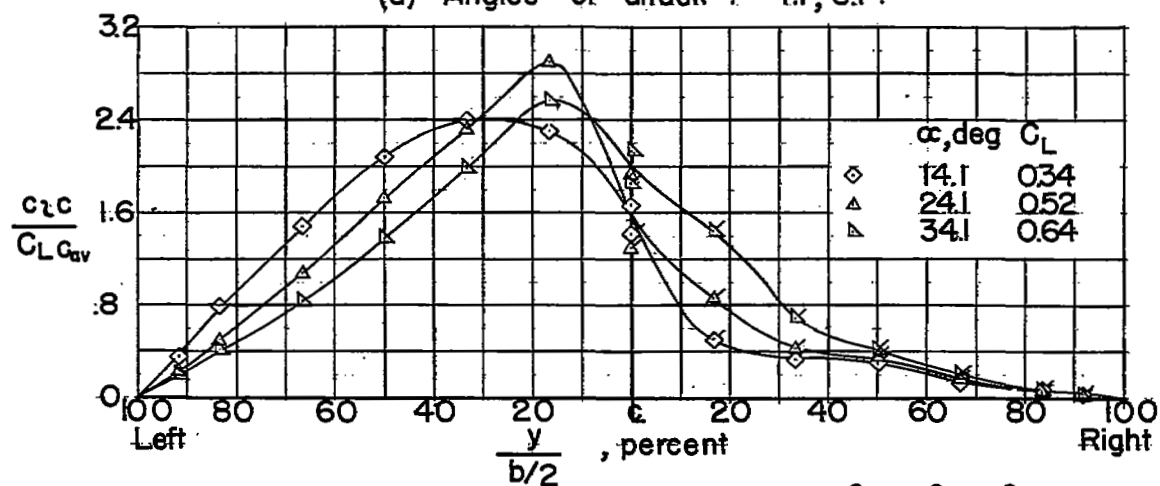


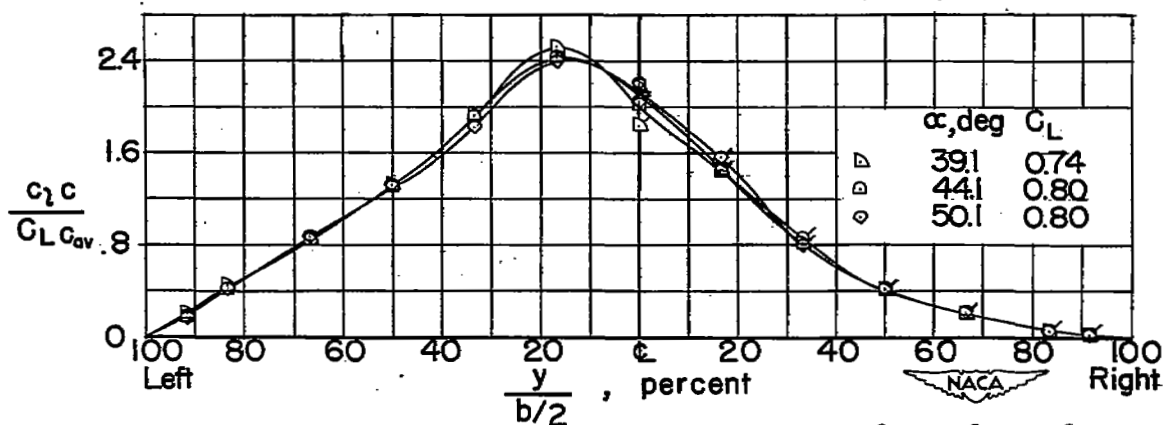
Figure 47.- Span load distribution of wing 3 at various angles of attack;  $\psi = 20^\circ$ . Flagged symbols represent data taken with left semispan at  $\psi = -20^\circ$ .



(a) Angles of attack : 4.1, 8.1.



(b) Angles of attack : 14.1°, 24.1°, 34.1°.



(c) Angles of attack : 39.1°, 44.1°, 50.1°

Figure 48.- Span load distribution of wing 3 at various angles of attack;  $\psi = 35^\circ$ . Flagged symbols represent data taken with left semispan at  $\psi = -35^\circ$ .

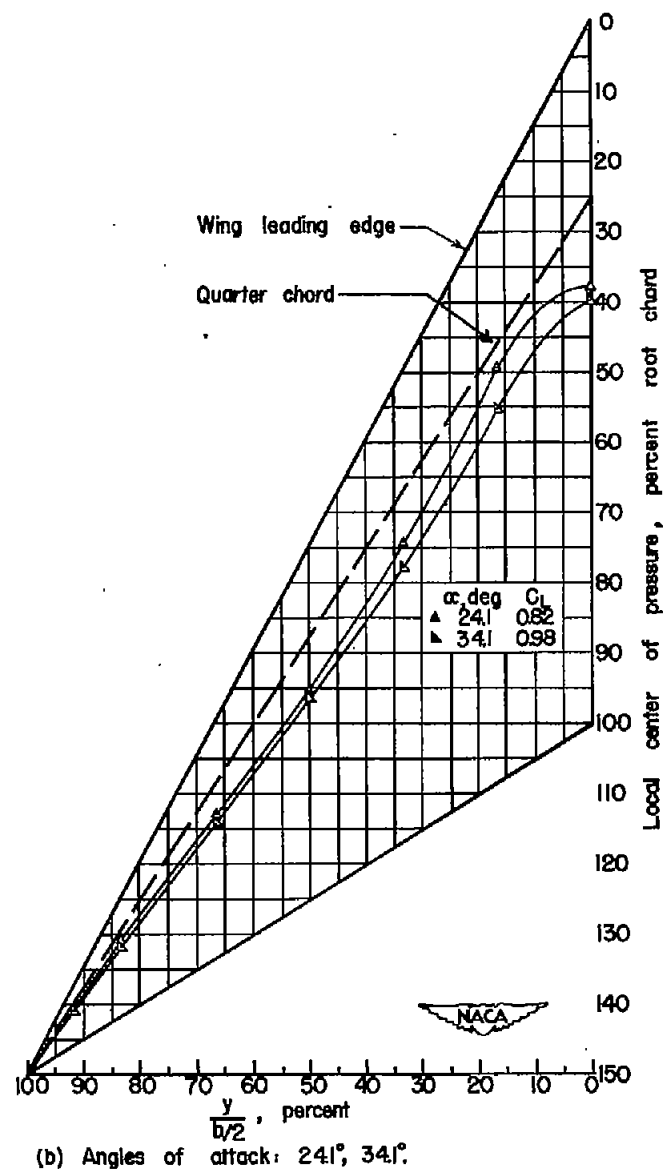
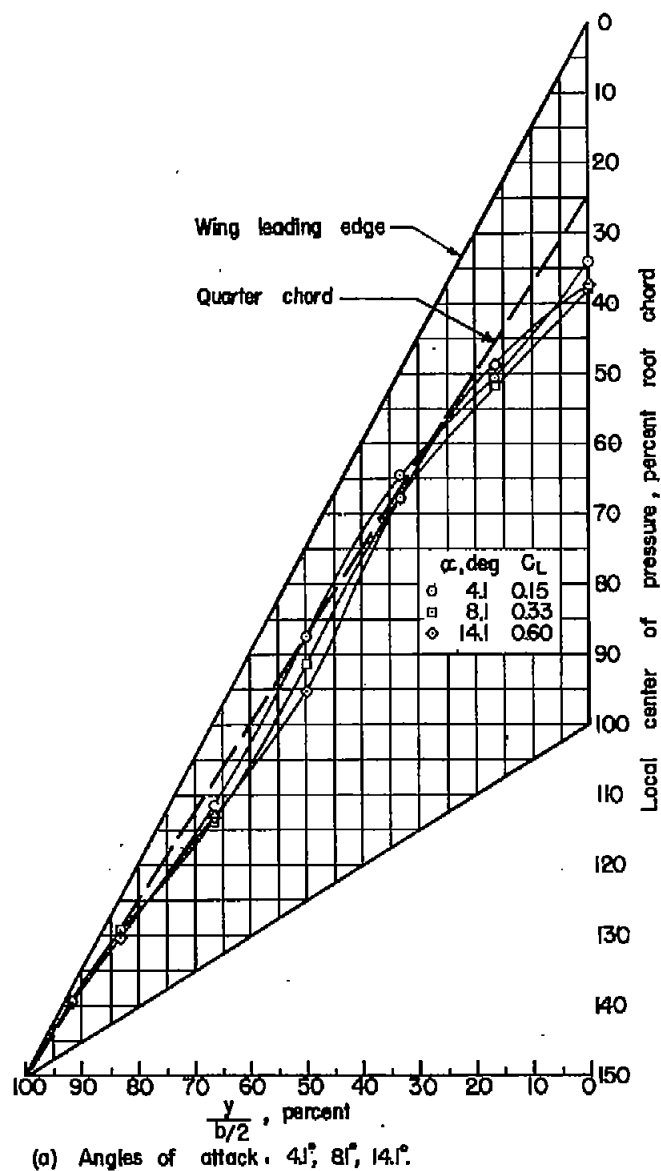
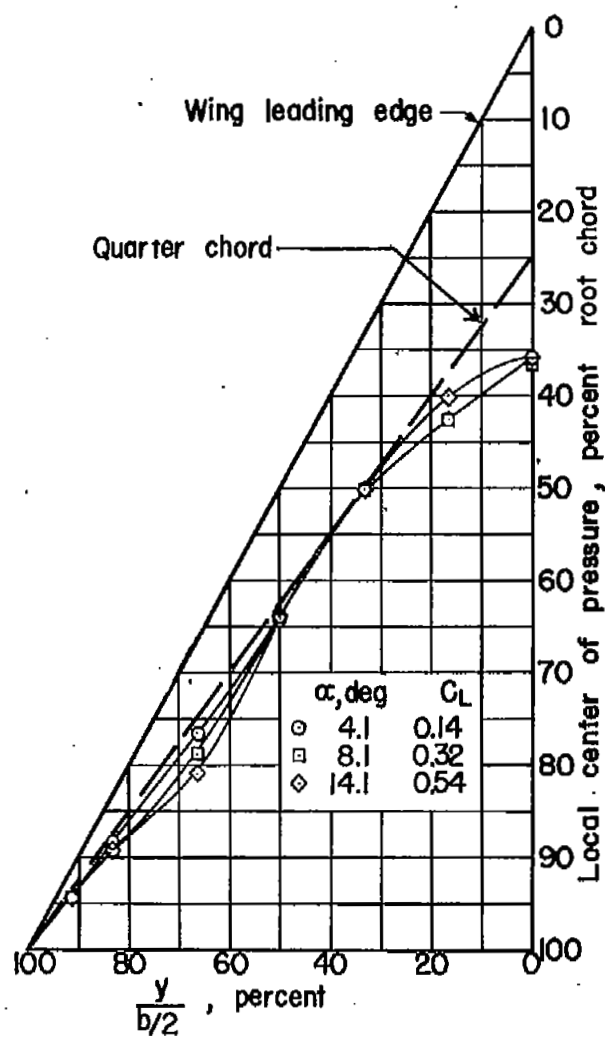
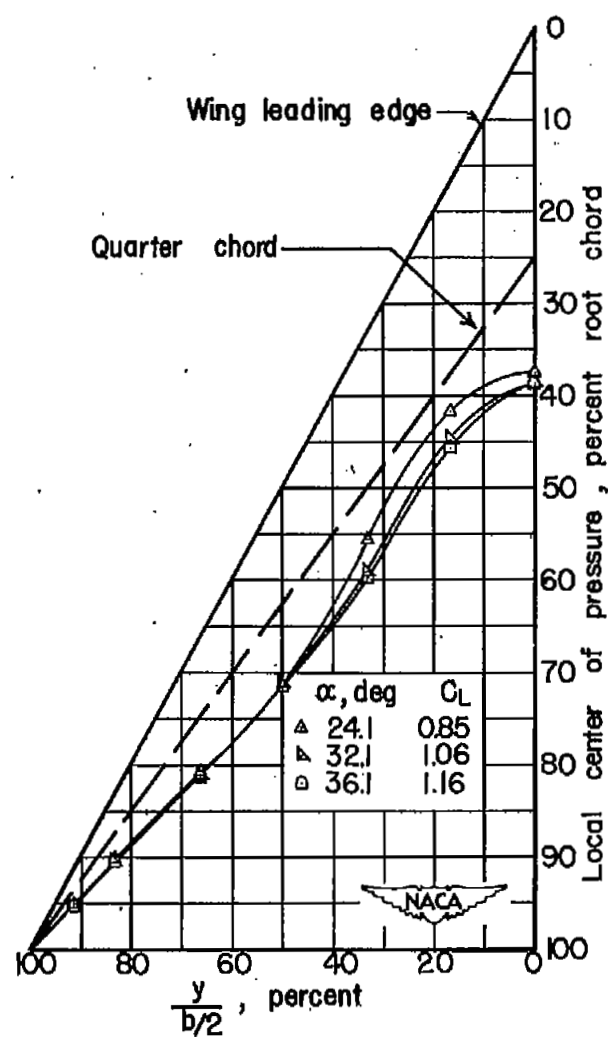


Figure 49.- Effect of angle of attack on the local center-of-pressure location of wing 1;  $\psi = 0^\circ$ .

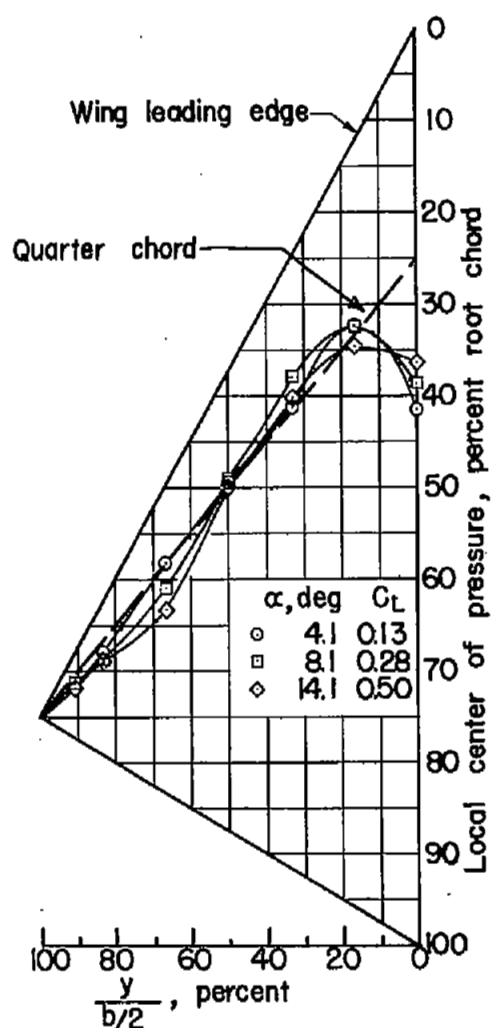


(a) Angles of attack: 4.1°, 8.1°, 14.1°.

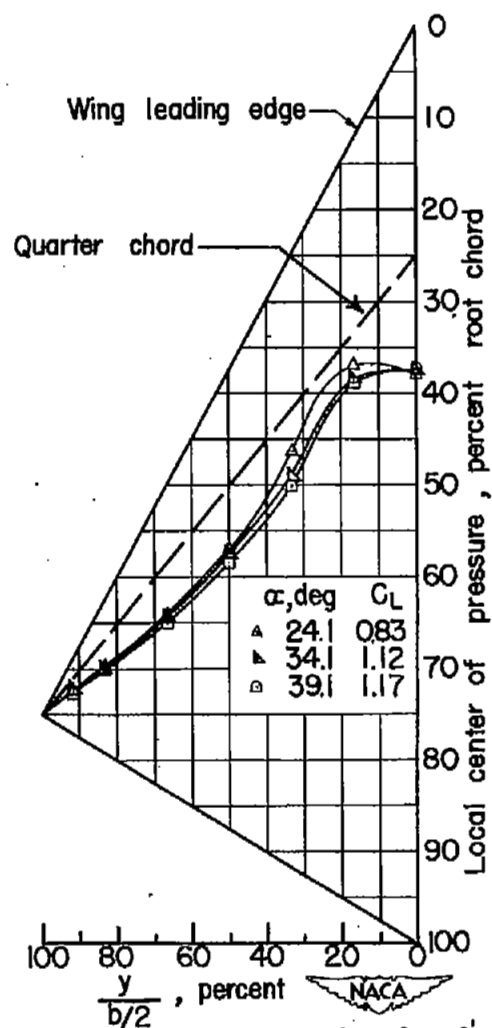


(b) Angles of attack: 24.1°, 32.1°, 36.1°.

Figure 50.- Effect of angle of attack on the local center-of-pressure location of wing 2;  $\psi = 0^\circ$ .



(a) Angles of attack: 4.1°, 8.1°, 14.1°



(b) Angles of attack: 24.1°, 34.1°, 39.1°

Figure 51.- Effect of angle of attack on the local center-of-pressure location of wing 3;  $\psi = 0^\circ$ .



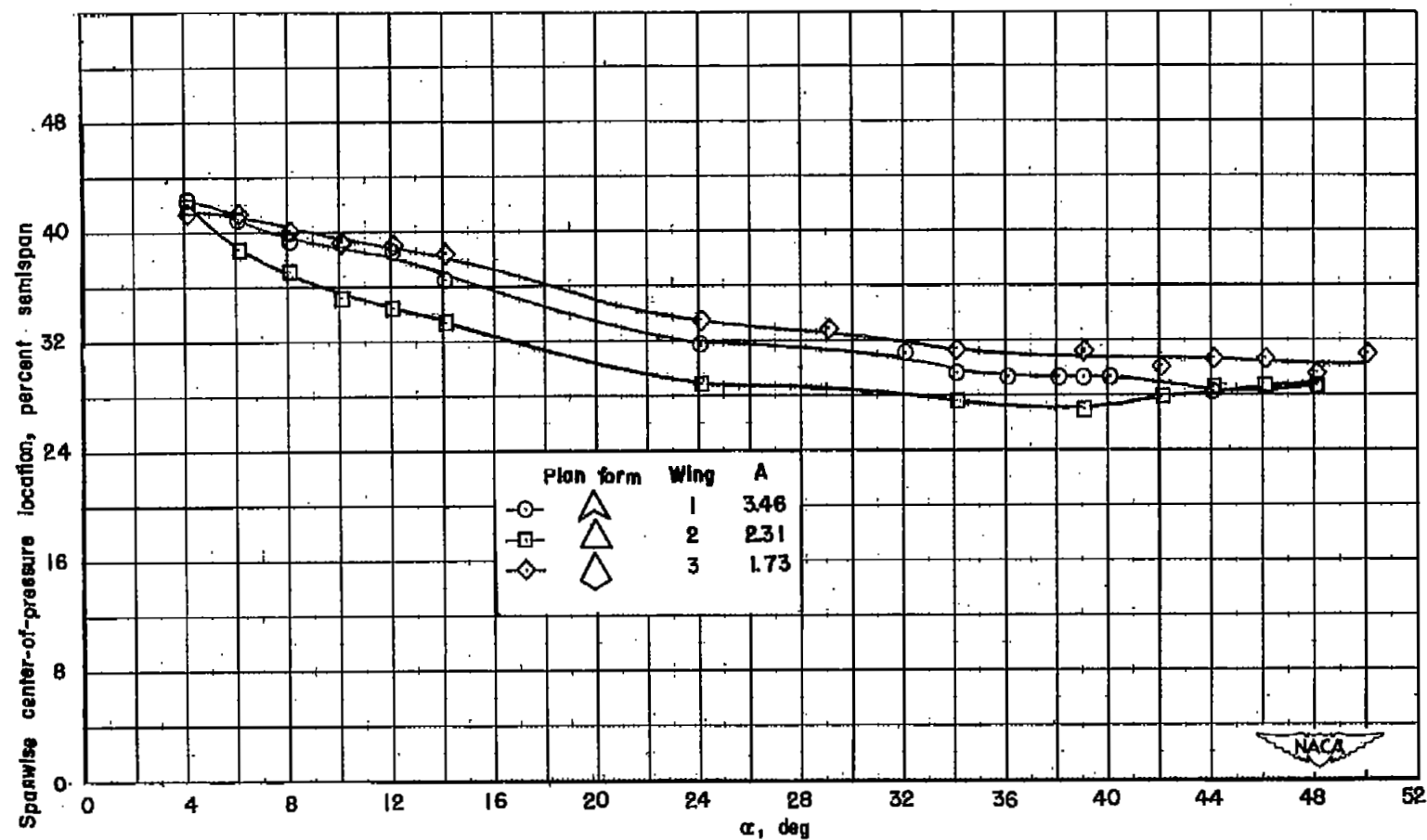


Figure 52.- Variation of wing spanwise center-of-pressure location with angle of attack for the wing investigated;  $\psi = 0^\circ$ .

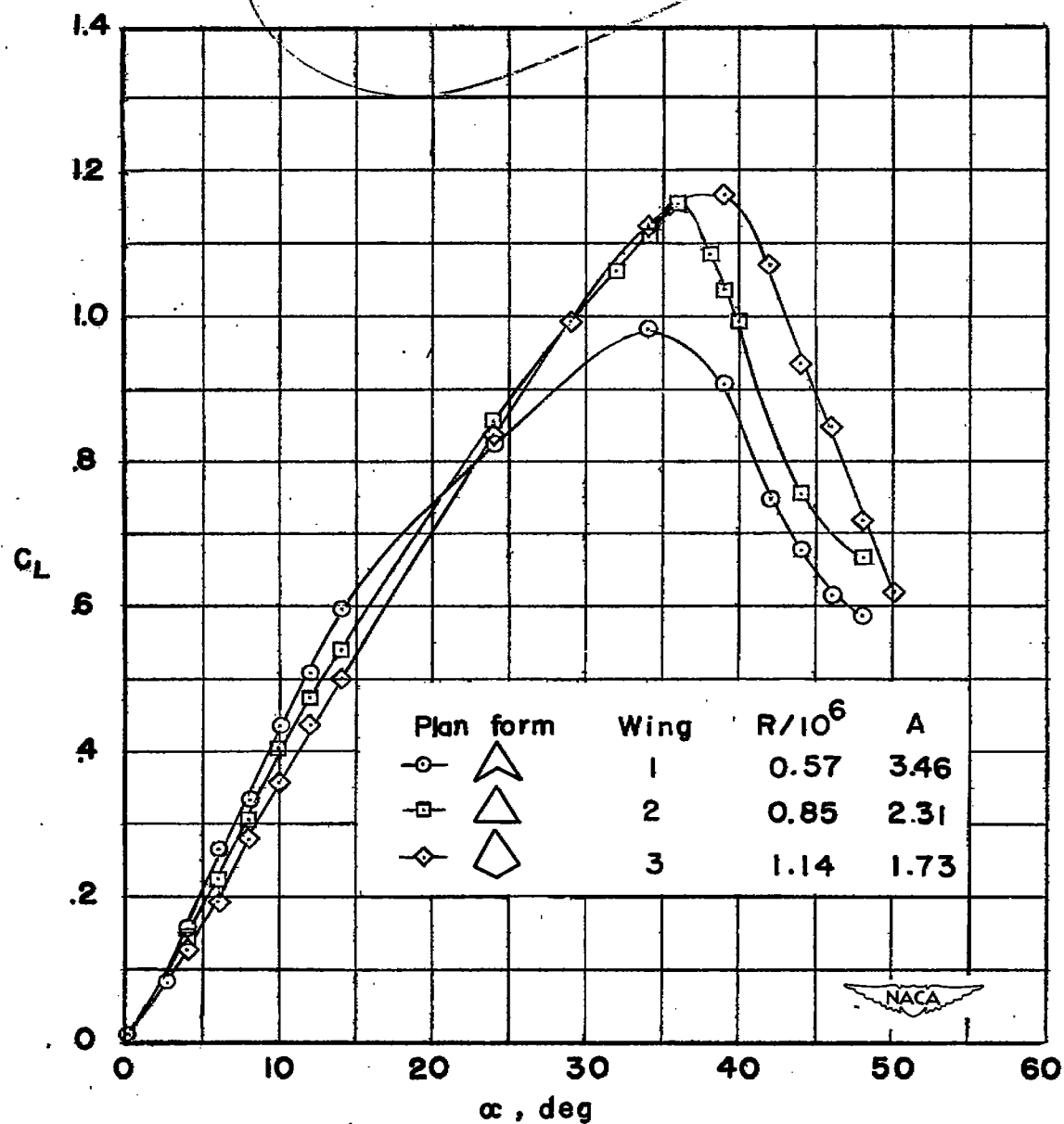


Figure 53.- Variation of  $C_L$  with  $\alpha$  for the three wings investigated.

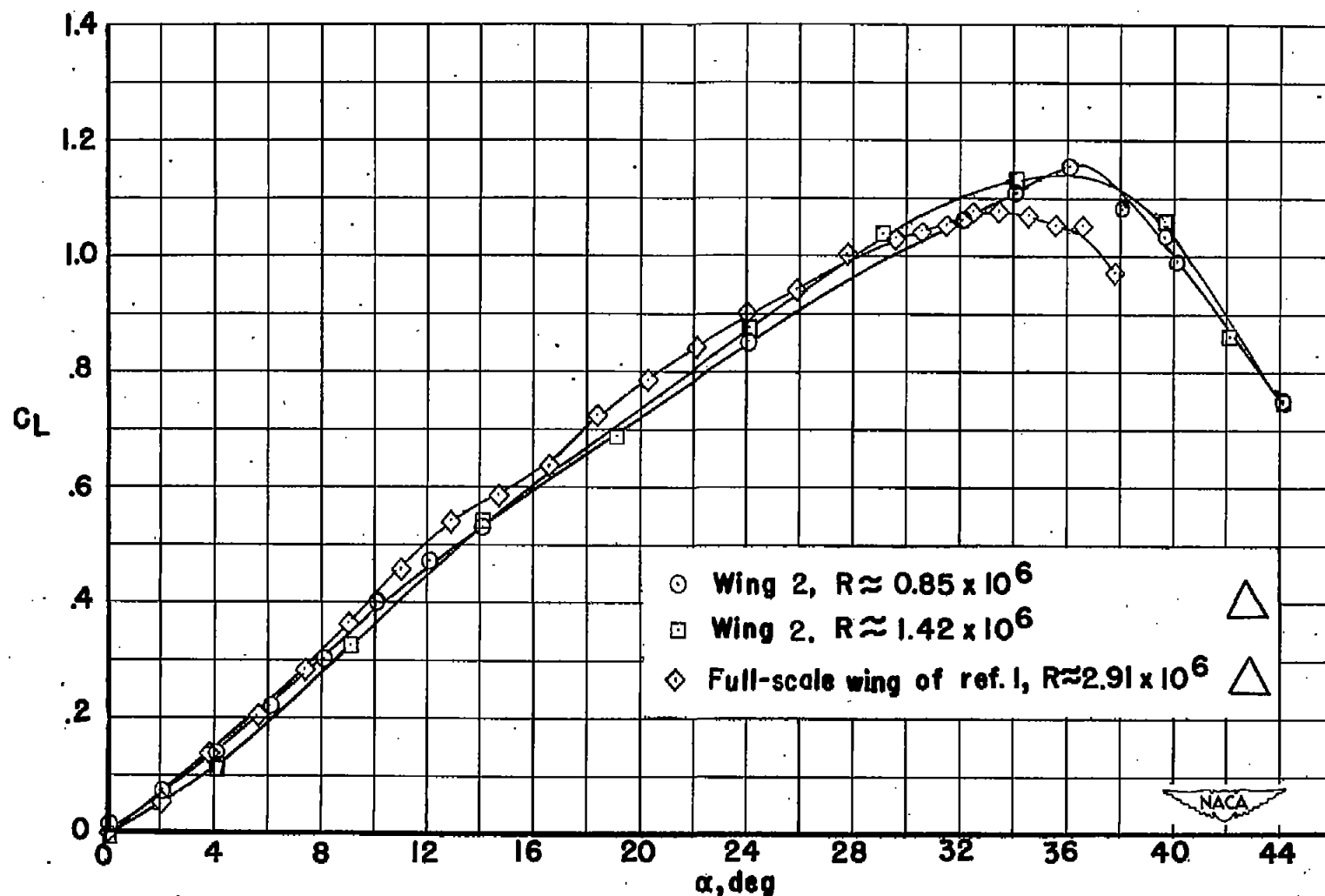


Figure 54.- Effect of Reynolds number on the variation of  $C_L$  with  $\alpha$  for wing and a comparison of the lift data of wing 2 with that of the comparable full-scale wing of reference 1.

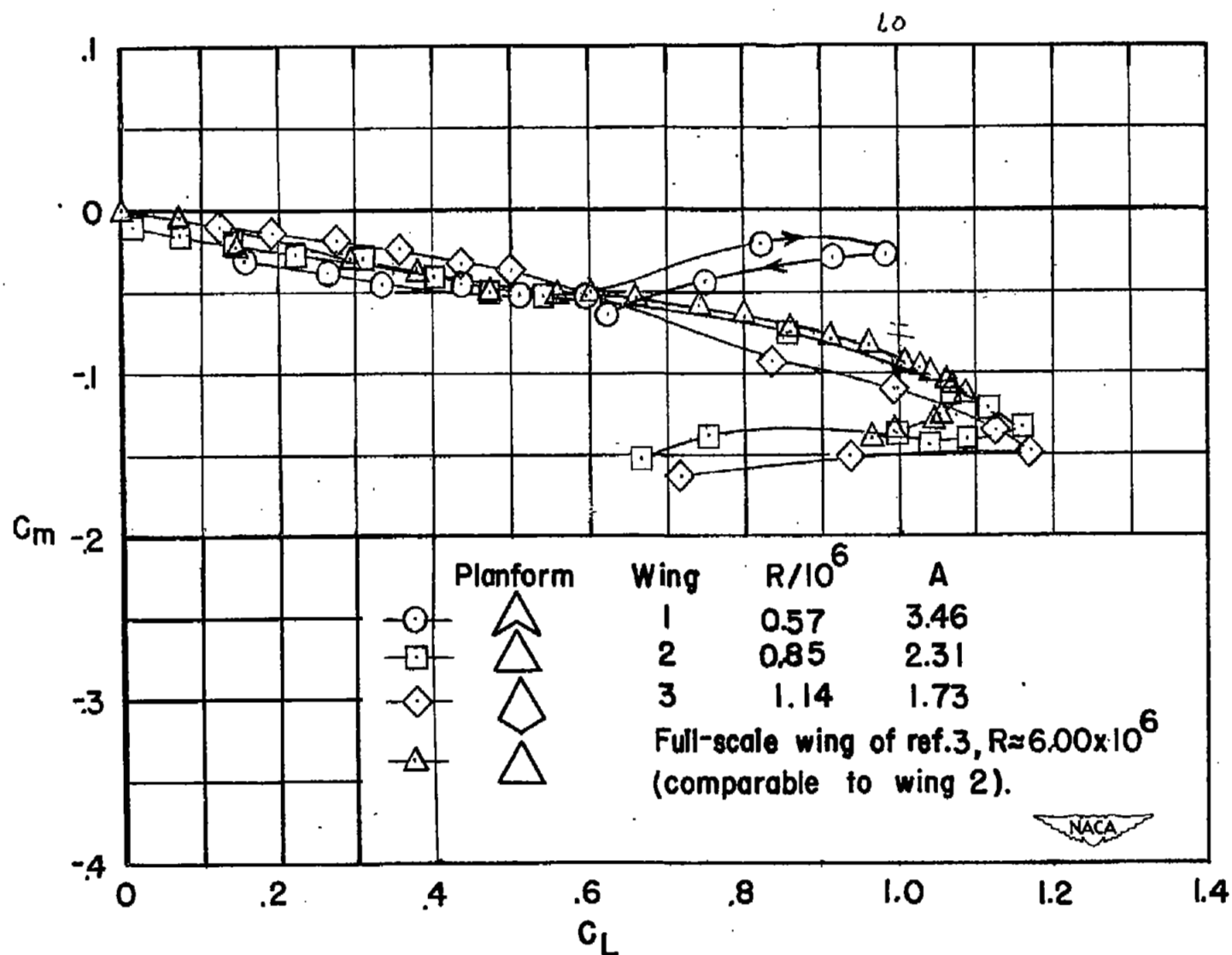


Figure 55.- Variation of  $C_m$  with  $C_L$  for the three wings investigated and a comparison of the variation of  $C_m$  with  $C_L$  of wing 2 with that of the comparable full-scale wing of reference 1.

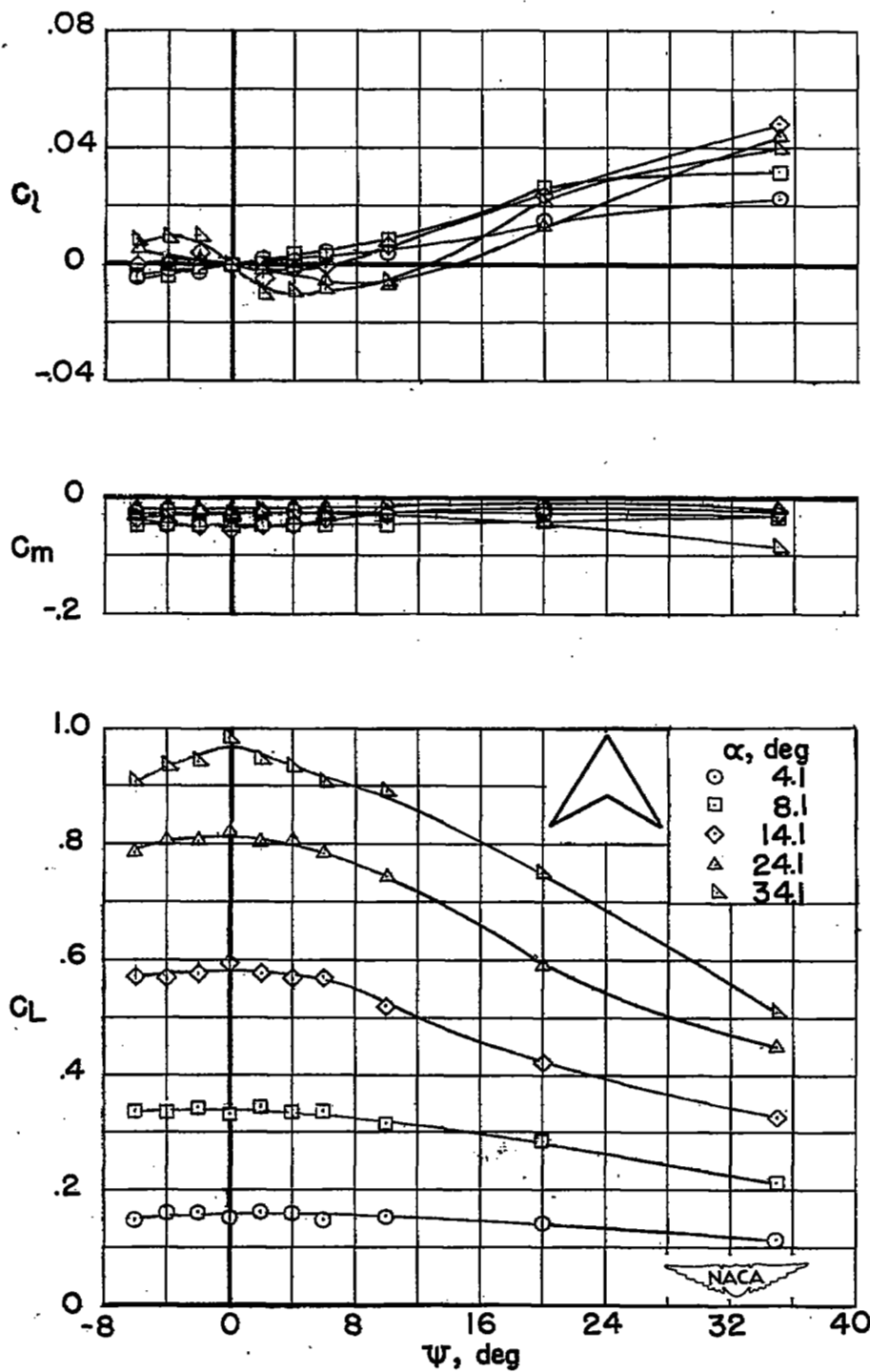


Figure 56.- Variation of  $C_L$ ,  $C_m$ , and  $C_D$  with  $\psi$  for wing 1 at various angles of attack.

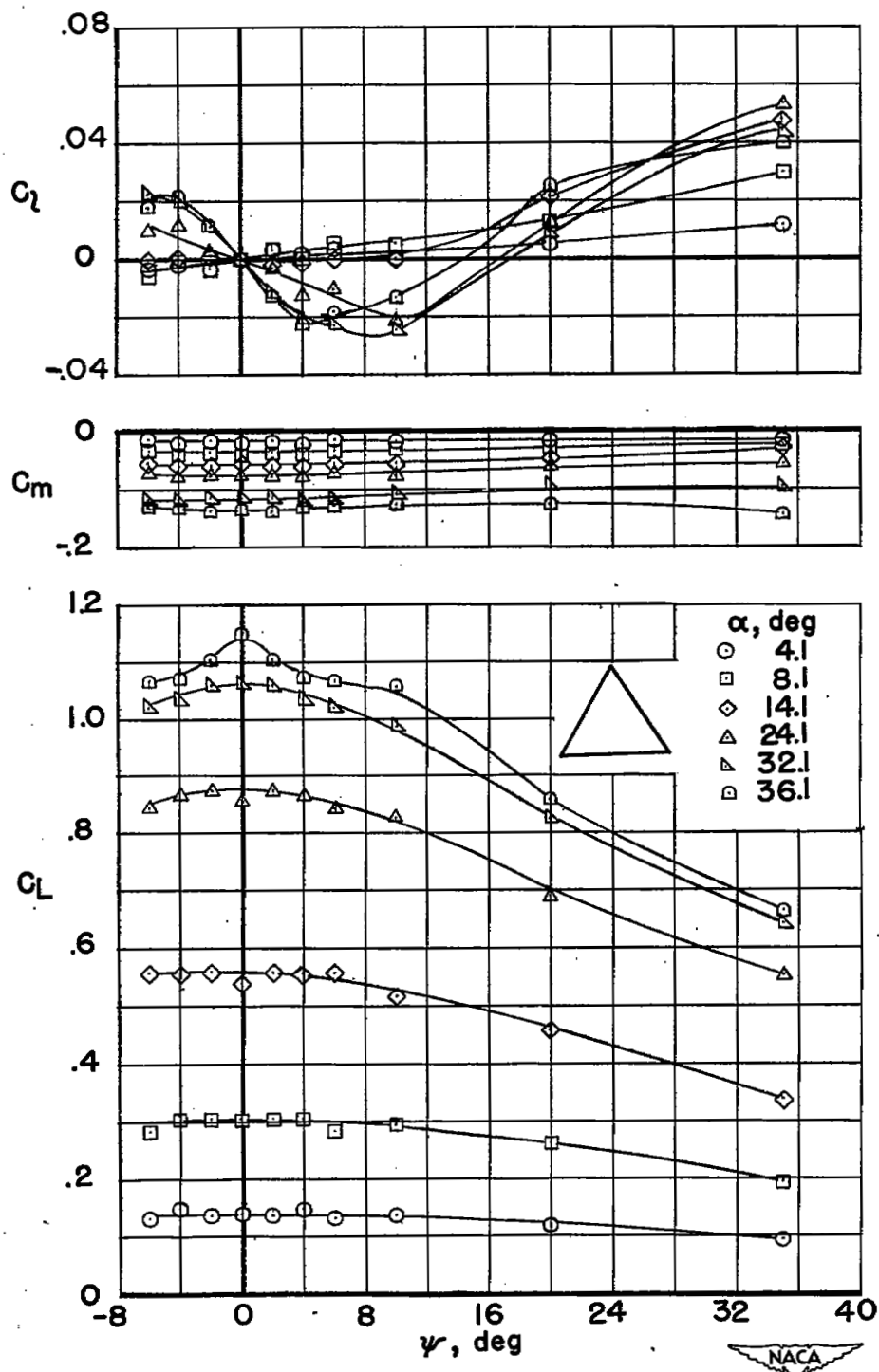


Figure 57.- Variation of  $C_L$ ,  $C_m$ , and  $C_l$  with  $\psi$  for wing 2 at various angles of attack.

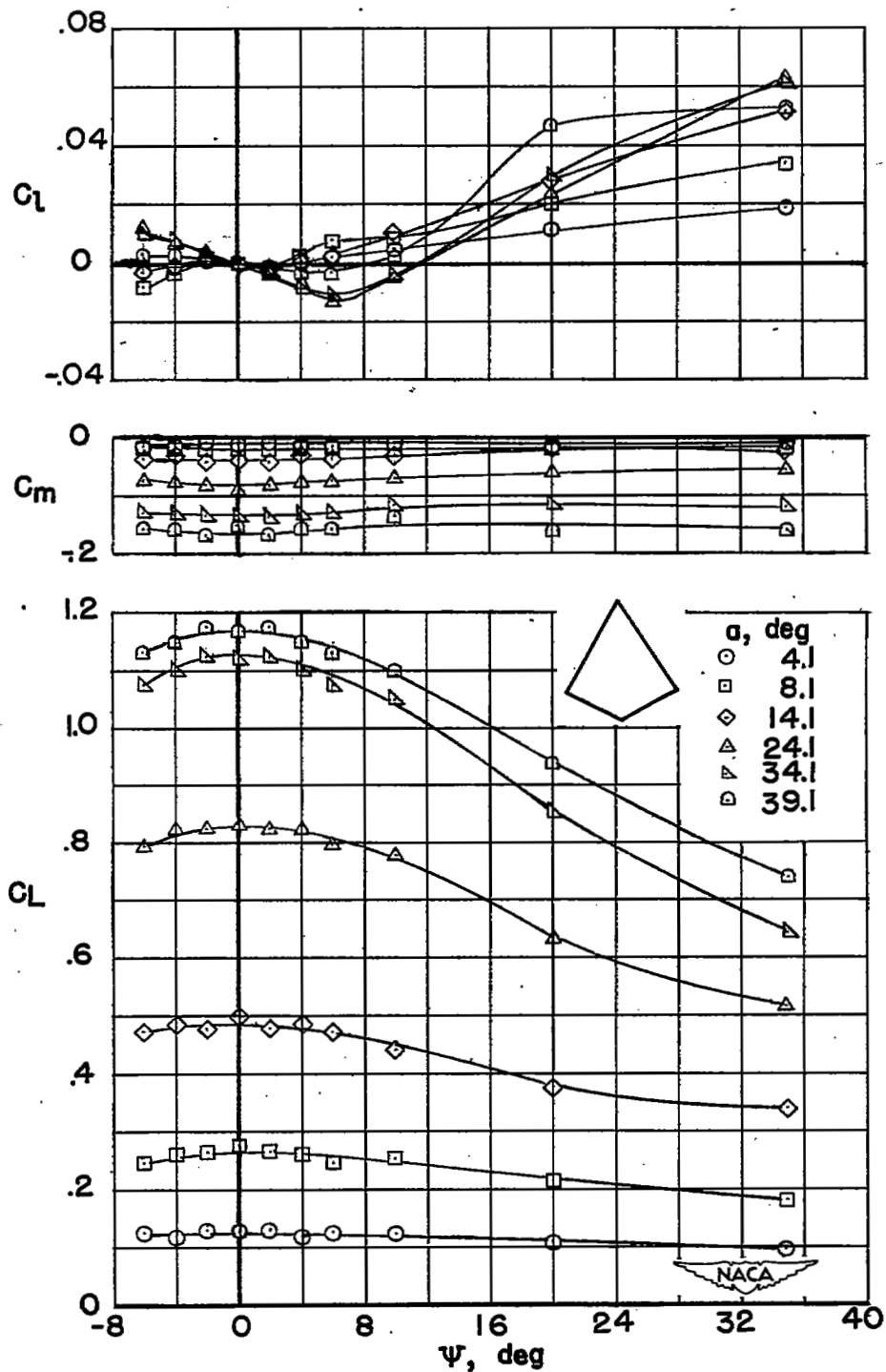


Figure 58.- Variation of  $C_L$ ,  $C_m$ , and  $C_l$  with  $\psi$  for wing 3 at various angles of attack.